Measurement of direct CP violation in $b \to sc\bar{c}$ and $b \to dc\bar{c}$ quark transitions using $B^+ \to J/\psi K^+$ and $B^+ \to J/\psi \pi^+$ decays

Kostyantyn Holubyev

MSc. Physics

November 2008

This thesis is submitted in partial fulfilment of the requirements for the degree of Doctor of Philosophy. No part of this thesis has been previously submitted for the award of a higher degree.

Abstract

This thesis describes the measurement of the direct CP violation in the $b \to sc\bar{c}$ transition using the decay $B^+ \to J/\psi K^+$, and in the $b \to dc\bar{c}$ transition using the decay $B^+ \to J/\psi\pi^+$. The decays of B^+ mesons are reconstructed in approximately 2.8 fb^{-1} of data recorded by DØ detector in 2002-2007 during Run II of Fermilab Tevatron collider. Using the unbinned likelihood fit, a signal of 40,222±242 of $B^+ \to J/\psi K^+$ and 1,578±119 of $B^+ \to J/\psi\pi^+$ events is obtained. The corresponding direct CP violation asymmetries are measured to be

$$A_{CP}(B^+ \to J/\psi(1S)K^+) = +0.0077 \pm 0.0061(\text{stat.}) \pm 0.0027(\text{syst.}),$$

and

$$A_{CP}(B^+ \to J/\psi(1S)\pi^+) = -0.089 \pm 0.081(\text{stat.}) \pm 0.028(\text{syst.}).$$

The result on $A_{CP}(B^+ \to J/\psi(1S)K^+)$ is consistent with the 2007 world average and is the most precise measurement of this asymmetry, with uncertainty approaching the level of the Standard Model prediction. The result on $A_{CP}(B^+ \to J/\psi(1S)\pi^+)$ constitutes the first measurement of this asymmetry at the hadron collider, with uncertainty at the level of the 2007 world average. The measurement presented in this thesis has become possible due to the sophisticated online and offline tracking/vertexing implemented at DØ, and the regular reversal of the polarities of the DØ detector magnets.

Acknowledgements

First of all, and above all, I am deeply thankful to my supervisor, Guennadi Borissov, for his guidance, help, and encouragement. I am thankful to all the research/teching stuff of the Particle Physics Group of Lancaster University, especially to Rob Henderson, Peter Ratoff, Alex Finch, Vato Kartvelishvili, and Tim Brodbeck (now retired), for teaching myself and my fellow PhD students the art of science.

I am deeply thankful to DØ people at Fermi National Accelerator Laboratory (Fermilab), Illinois, USA. I want to thank Dmitri Denisov, for his help in my settling at Fermilab. I want to thank all members of B physics group of DØ, for sharing with me their strong experience in experimental physics in general, and in B physics in particular, and for their active involvement in preparing the results of the measurement reported in this dissertation for publication. I want to thank members of DØ Tracking Group, for helping me better understand the DØ detector and the software environment.

I am extremely thankful to many my fellow colleagues, especially:

to Mark Williams, for generating the Monte Carlo samples used in the presented analysis;

to Alexander Rakitin (former member of DØ , now at BaBar) for being ready to answer every my question, either physics-, or detector-related, and not necessarily wise. I am very thankful to him for teaching me to use Linux, and for showing an immense quantity of most useful C++ and ROOT tips and tricks. I am also thankful to Mr Rakitin for having pleasure to enjoy his company at our leisure;

to Juan Carlos Bueno Sánchez for our most interesting discussions and his introducing me to the field of modern cosmology. The latter was even more valuable by being reasonably far from my favorite experimental particle physics. I am also thankful to Juan for his help in my coping with LaTeX,

and for taking a burden of proofreading my dissertation.

I am thankful to all the mates who I shared an office at Lancaster with, for being a cordial and merry folks.

Also, I am thankful to Peter Ratoff, the former head of Particle Physics Group of Lancaster University (now head of Physics Department), for arranging a financial support for my stay at Lancaster. I am thankful to the administrative officers of Physics Department, especially to Barbara Colman and Robin Lewsey, who safely guide the physicists of Lancaster University through the legislative procedures.

Lastly, I am especially thankful to all those whose help was minor, since these are small bricks which make a big house.

Lancaster, November 2008.

Contents

Abstract 1

Acknowledgements 2

List of Figures 6

List of Tables 10

1 The Theoretical Background 13

1.1 Symmetries in physics 14

1.1.1 C, P, T transformations and CPT-theorem 14

1.1.2 Some history 15

1.1.3 Cabibbo-Kobayashi-Maskawa (CKM) matrix 18

1.2 Particle-antiparticle mixing and CP violation 24

1.3 More CP violation needed! 31

1.4 Observables and motivation 34

1.4.1 Direct CP asymmetry in the $B^+ \to J/\psi K^+$ decay . . 34

Present status 39

1.4.2 Direct CP asymmetry in the $B^+ \to J/\psi \pi^+$ decay . . 41

Present status 41

1.4.3 Perspectives for Tevatron and Analysis strategy . . . 42

2 Experimental Apparatus and Data Acquisition 46

2.1 Accelerator complex 46

2.1.1 Accelerator chain 46

2.1.2 Accelerator performance 49

2.2 DØ detector 50

2.2.1 Central Tracking System 52
SMT 54
Central Fiber Tracker 57
Solenoidal magnet 59
2.2.2 Muon system 60
Toroidal magnet 61
Central muon system 61
Forward muon system 62
2.2.3 Other systems 63
Calorimeter and Preshower 63
Luminosity monitor 63
2.2.4 Trigger system 64
L1 trigger 65
L2 trigger 66
L3 trigger 66
Trigger bits 66
2.3 Event reconstruction 67
2.3.1 DØRECO 67
2.3.2 Tracking at DØ 69
DØ Detector surfaces 70
Track finding by AA 72
Track finding by HTF 73
GTR track refit 76
Vertexing 77
2.3.3 Muon identification 79
2.4 DØ upgrade for RunIIb 82
2.5 Event simulation 83

3 Data analysis **85**
3.1 Tools 85

3.1.1 Triggers for B physics 85
3.1.2 BANA package 87
3.1.3 Inclusive muon skim 88
3.2 Detector-induced asymmetries 89
3.3 Measurement of the kaon charge asymmetry using the decay $D^0 \to \mu^+ K^- \nu_\mu$ 94
3.3.1 Choice of the decay channel 96
3.3.2 Event selection 96
3.3.3 Signal extraction 99
3.3.4 Solving the detector model 104
3.3.5 Sample composition 109
3.3.6 Systematic uncertainties 113
3.3.7 Kaon asymmetry in other event samples 114
3.3.8 Results and Conclusions 118
3.4 Measurement of direct CP violation in $b \to sc\bar{c}$ and $b \to dc\bar{c}$ quark transitions using $B^+ \to J/\psi K^+$ and $B^+ \to J/\psi \pi^+$ decays 119
3.4.1 Event selection 120
3.4.2 Signal extraction 124
3.4.3 Solving the detector model 133
3.4.4 Kaon asymmetry in the $J/\psi K$ sample 135
3.4.5 Systematic uncertainties 137
3.4.6 Consistency check 141
3.4.7 Results and Conclusions 142

Conclusions **143**

Appendix **145**

Decay file 145

Bibliography **147**

List of Figures

1.1 Six unitarity triangles. 21

1.2 The Unitarity Triangle. 22

1.3 CKM fit as of summer 2008. 22

1.4 The celebrated box diagrams giving rise to $\Delta F = 2$ transitions in K ($F \equiv S$), D ($F \equiv C$) and $B_{(s)}$ ($F \equiv B$) systems. . 25

1.5 Three cases of CP violation: direct, in mixing, in interference. 28

1.6 $B^+ \to J/\psi K^+(\pi^+)$: Standard Model diagrams. 35

1.7 $B^+ \to J/\psi K^+$: hypothetical $b \to sZ'$ transition. 39

2.1 Tevatron accelerator complex. 48

2.2 Peak luminosities during the Run II of Tevatron. 49

2.3 Weekly integrated luminosity and its cumulative total during the Run II. 49

2.4 General view of DØ Run II detector. 51

2.5 Track parameters on a z plane. 54

2.6 Central tracking system of DØ Run II detector, view in (x, z) plane. 55

2.7 Principle of silicon microstrip tracker. 56

2.8 The disk-barrel structure of the DØ silicon microstrip tracker. 56

2.9 Cross-section of SMT barrel module. 57

2.10 The design of double-sided 2° ladder. 58

2.11 Exploded view of the muon wire chambers. 61

2.12 Overview of DØ trigger and Data Acquisition System. 65

2.13 Block diagram of L1 and L2 trigger systems. 65

2.14 Steps of DØ Offline Reconstruction Program and BANA package. 69
2.15 DØ tracking procedure as of 2008. 70
2.16 DØ detector surfaces defined for the purposes of track propagation in the Kalman filter. 72
2.17 Track propagation (Kalman filtering) in AA. 74
2.18 Hough transform in HTF. 75
2.19 Parameters describing multiple scattering. 77
2.20 Muon local segments from drift circles. 79
2.21 The L0 design. 83

3.1 Integrated luminosity delivered by Tevatron, and the luminosity recorded by DØ in the current Run II. 87
3.2 Polarity reversal helps reduce systematic effects by exposing different parts of the detector to the same flux of oppositely charged particles. 90
3.3 The range-out changes when the sign of either q, β, or γ changes. 93
3.4 The combined significance of the D^0 with respect to the primary vertex. 98
3.5 The invariant mass distribution of the μK system. 100
3.6 The distribution of the mass difference $\Delta m = m(\mu K\pi) - m(\mu K)$, which allows to clearly see the resonance $D^* \to (\mu K\nu)\pi$. 100
3.7 Δm distributions in the sideband of the D^0 peak. 102
3.8 The distribution of the μK invariant mass for right sign and wrong sign events. 103
3.9 The Δm distribution for right sign and wrong sign events. . 104
3.10 Signal distribution and background distribution for different $m(\mu K)$ bins. 105

3.11 The dependence of the signal significance $S/\sqrt{S+B}$ on the position of the upper signal bound for seven $m(\mu K)$ bins. . . 106
3.12 The distribution of the invariant mass of two pions selected in addition to the $\mu K\pi$ system. 110
3.13 The distribution of the invariant mass of the $K_S\pi$ system in the signal region of the whole $m(\mu K)$ range. 110
3.14 The distribution of the invariant mass of the $K_S\pi$ system in the signal regions of seven $m(\mu K)$ bins. 111
3.15 The θ dependence of the length of the kaon trajectory in the tracking volume. 116
3.16 The cross-sections of inelastic interaction of negative and positive kaons with matter. 117
3.17 The dependence of the kaon asymmetry, A_K, on the kaon momentum, p_K, in eight bins of approximately equal statistics. 118
3.18 The dependence of the kaon asymmetry, A_K, on $1/\sin\theta_K$. . 119
3.19 The invariant mass distribution of the two-muon system. . . 120
3.20 Distribution of the invariant mass of the $m(J/\psi K)$ system after applying the selection cuts. 123
3.21 Normalized distributions of the discriminating variables: minimal transverse momentum of the two muons, kaon transverse momentum, and isolation of the $J/\psi K$ system. 125
3.22 Normalized distributions of the discriminating variables: transverse projection of B^+ decay length divided by its error, χ^2 of the B^+ decay vertex, and combined significance of B^+. . . 126
3.23 Normalized distributions of the discriminating variables: combined significance of kaon. 127
3.24 Distributions of $\log_{10}(y)$, where y is a combined tagging variable. 127
3.25 Significance of the signal computed as $N(signal)/\sqrt{N(tot)}$ as a function of the selection cut on $\log_{10}(y)$. 127

3.26 The distribution of the invariant mass of the $J/\psi K$ system after the final selection using the likelihood ratio method. . . 128
3.27 The $m(J/\psi K)$ distribution obtained using Monte Carlo simulation of $B^+ \to J/\psi K^*(K^+X)$ and $B^+ \to J/\psi K_1(1270)(K^+X)$ events. 130
3.28 Distributions of $B^+ \to J/\psi K^+$ and $B^+ \to J/\psi K^+X$ have similar dependence on p_K. 132
3.29 Result from the unbinned fit of invariant mass distribution of the $J/\psi K$ system. 133
3.30 Momentum distribution in the $B \to J/\psi K$ sample. 138

List of Tables

1.1 Current experimental data for $B \to K\pi$. 37

1.2 Measurements of $C_{b\to sc\bar{c}}$ used by HFAG for end of 2007 averages. 40

1.3 Averaged $A^{dir}_{J/\psi K^+}$ from the direct decays, from PDG 2007. . 40

1.4 Measurements of $C_{b\to dc\bar{c}}$ used by HFAG for end of 2007 averages. 42

1.5 Averaged $A^{dir}_{J/\psi\pi^+}$ from the direct decays, from PDG 2007. . . 43

2.1 Tevatron parameters for Run II(a/b) 48

2.2 Pitches of different silicon detectors comprising DØ Silicon Mictrostrip Tracker. 58

2.3 Helix parameters at different surfaces. 71

2.4 Possible cases of track-muon matching. 80

3.1 Summary of the event selection cuts for the $D^* \to D^0(\mu\nu K)\pi$ decay. 97

3.2 The numbers of D^* events $n_q^{\beta\gamma}$ in eight subsamples for the signal and the background. 106

3.3 The physics and detector asymmetries for the D^* and the background events (MINUIT output). 107

3.4 The numbers of D^* events $n_q^{\beta\gamma}$ in eight subsamples for the signal and the background. Alternative definition of background is used. 108

3.5 The physics and detector asymmetries for the D^* and the background events. Alternative definition of background is used. 108

3.6 D^* sample composition: contributing D^0 decay modes. . . . 109
3.7 The systematic uncertainties on A_K. 114
3.8 The kaon asymmetry, A_K, measured in eight bins of kaon momentum, p_K, of approximately equal statistics. 116
3.9 Summary of the event selection cuts for the $B^+ \to J/\psi(\mu\mu)K^+$ decay. 121
3.10 Parameters of the unbinned fit shown in Fig. 3.29. 134
3.11 Result from the unbinned fit shown in Fig. 3.29: number of events in each channel. 134
3.12 Number of events in the $J/\psi K$, $J/\psi\pi$, and $J/\psi KX$ channels, and in the combinatorial background, in different $\beta\gamma q$ subsamples. 136
3.13 Physics asymmetry A and detector asymmetries for different channels. 136
3.14 The systematic uncertainties on $A^{dir}_{J/\psi K^+}$ ($A^{dir}_{J/\psi\pi^+}$). 138
3.15 $A(J/\psi K)$: the systematic effect from the mass parameterization. 139
3.16 $A(J/\psi\pi)$: the systematic effect from the mass parameterization. 139
3.17 $A^{dir}_{J/\psi K^+}$ separately for $p_K < 4.2$ GeV/c and $p_K > 4.2$ GeV/c. 142

Chapter 1

The Theoretical Background

In his Nobel Prize lecture (1964) Wigner points out that "the surprising discovery of Newton's age is just the clear separation between the laws of nature on one hand and initial conditions on the other" [1]. Wigner then contrasts the symmetries of the laws of nature and the random character of the initial conditions, and summarizes: "A law of nature can be accepted as valid only if the correlations which it postulates are consistent with the accepted invariance principles". The increasing role of the invariance principles in physics is investigated by Wigner in a collection of articles, now available under one cover [2].

To the extent symmetries are important, so are their violations. The discovery of violation of parity (P) and charge conjugation (C) in weak interactions, and then the discovery of violation of the combined CP symmetry considerably enriched our understanding of nature. Ever since, the measurements of violation of the combined CP symmetry in various weak systems constitutes an important field of experimental particle physics. This work aims to make a modest contribution to this field.

This chapter is organized as follows. In Section 1.1 we list some milestones that paved the way for the discovery and incorporation of CP violation into the Standard Model (SM). In Section 1.2 we concentrate on the quantum-mechanical formalism of the particle-antiparticle mixing and in-

troduce the relevant CP violation observables. In Section 1.3 we give the modern motivations to pursue CP violation studies. In Section 1.4 we motivate our interest in direct CP violation asymmetry in $b \to sc\bar{c}$ and $b \to dc\bar{c}$ transitions.

1.1 Symmetries in physics

1.1.1 C, P, T transformations and CPT-theorem

Let us first remind the symmetry operations we deal with:

- Space reflection P: $x \to -x$. For instance, for momentum $\mathbf{p}$ and angular momentum $\mathbf{l}$ we have:

$$\mathbf{p} \xrightarrow{\mathrm{P}} -\mathbf{p}, \quad \mathbf{l} \equiv \mathbf{x} \times \mathbf{p} \xrightarrow{\mathrm{P}} \mathbf{l}. \tag{1.1}$$

  The space reflection, called *parity operation* in quantum mechanics, provides a general classification of vectors and scalars. Polar vectors change sign under the parity transformation ($\mathbf{V} \xrightarrow{\mathrm{P}} -\mathbf{V}$), and axial vectors do not ($\mathbf{A} \xrightarrow{\mathrm{P}} \mathbf{A}$). Among scalars, there are proper scalars ($S \xrightarrow{\mathrm{P}} S$), and pseudoscalars ($P \xrightarrow{\mathrm{P}} -P$).

- Time reversal T: $t \to -t$:

$$\mathbf{p} \xrightarrow{\mathrm{T}} -\mathbf{p}, \quad \mathbf{l} \xrightarrow{\mathrm{T}} -\mathbf{l}. \tag{1.2}$$

- Charge conjugation C: particle $\to$ antiparticle. The concept of antiparticles and charge conjugation naturally arises in the context of relativistic quantum mechanics.

It has been verified in a long list of experiments that the electromagnetic and strong interactions are invariant under C, P, and T transformations [3]. Weak interactions, however, are not invariant under any of these transformations, but they are believed to obey the combined CPT symmetry. CPT

constitutes a fundamental symmetry which has a significance over and above the three component symmetries. The corresponding *CPT theorem* states [4] that the CPT invariance must hold on the basis of

- Lorentz invariance;
- The existence of a unique vacuum state;
- Locality: fields either commute or anti-commute for spacelike separations.

The spin-statistics connection − integral spin for bosons and half integral spin for fermions − follows automatically. An important consequence of the CPT theorem is that particles and antiparticles should have equal masses and lifetimes. This is a non-trivial result: it implies that weaker CPT invariance is enough for masses and lifetimes of particles and antiparticles to be equal, irrespective of C or CP conservation.

1.1.2 Some history

The evolution of the Standard Model has been noticeably experiment-driven. To illustrate this, we briefly sketch the path to the discovery of CP violation, and its accommodation into the SM formalism. All the details can be found in the references given.

- Quark hypothesis.

  In 1964, Gell-Mann and Zweig remarked [5] that one can imagine the then known baryons and mesons to be made up of three quarks, u, d, and s, and three corresponding antiquarks. Then, the mesons could be taken to be bound $q\overline{q}$ states, with ^1S states corresponding to pseudoscalar particles, and ^3S states corresponding to the vector particles. Baryons had to be qqq states.

- Glashow-Illiopoulos-Maiani (GIM) mechanism.

By 1960s, the u, d, and s quark flavors have already shown a specific pattern in their weak interactions [6]:

1. $\Delta S = 1$ transitions ($u \leftrightarrow s$) are suppressed relative to $\Delta S = 0$ transitions ($u \leftrightarrow d$): e.g. the transition rates

$$\frac{K^- \to \pi^0 e \overline{\nu}_e}{n \to p e \overline{\nu}_e} \sim \frac{1}{25}; \tag{1.3}$$

2. The strangeness-changing neutral currents are absent, at least at the tree level: $\langle d|s\rangle = 0$, as inferred from

$$\mathrm{Br}(K_S^0 \to \mu\mu) \sim 10^{-9}. \tag{1.4}$$

The first finding was incorporated by Cabibbo, who suggested that u couples to the mixed state of d and s, $d' = d\cos\theta_C + s\sin\theta_C$. The second finding forced Glashow, Iliopoulos, and Maiani (GIM) to hypothesize the fourth flavor, the charm c, with $\langle s|c\rangle$ and $\langle d|c\rangle$ to exactly cancel out $\langle u|s\rangle$ and $\langle u|d\rangle$. The u and c quarks were thought to couple to the down-type quark states rotated in the flavor space through the Cabibbo angle θ_C:

$$\begin{pmatrix} d' \\ s' \end{pmatrix} = \begin{pmatrix} \cos\theta_C & \sin\theta_C \\ -\sin\theta_C & \cos\theta_C \end{pmatrix} \begin{pmatrix} d \\ s \end{pmatrix}. \tag{1.5}$$

All the experimental results were found consistent with a single value of $\sin\theta_C \approx 0.22$. The unitarity of the rotation matrix ensured both the universality of the weak coupling and the absence of the strangeness changing neutral currents.

- P (C) violation.

P, and correspondingly C violation, were discovered in nuclear β decay of ^{60}Co by Wu et al [7]. Subsequent experiments with nuclear and particle decays showed that the Lorentz-invariant weak transition amplitude $\mathcal{A}$ should 1) contain vector (V) and axial vector (A) parts

to accommodate Fermi and Gamow-Teller weak transitions; 2) contain both scalar and pseudoscalar parts to accommodate P and C violation:

$$\begin{aligned} \mathcal{A} &= G \sum_{i=V,A} (\overline{U}\mathbf{V}_C \mathrm{O}_i D) \left(\bar{l}(c_i + c_i'\gamma^5 \mathrm{O}_i)\nu\right) \\ &\sim V \cdot V + V \cdot A + A \cdot V + A \cdot A, \end{aligned} \tag{1.6}$$

where G is Fermi coupling constant, $\overline{U} = (\overline{u}, \overline{c})$, $D = (d, s)^T$, $\bar{l} = (\overline{e}, \overline{\mu})$, $\nu = (\nu_e, \nu_\mu)^T$, $\mathbf{V}_C$ is the Cabibbo rotation matrix from (1.5), $\mathrm{O}_V = \gamma^\mu$ and $\mathrm{O}_A = i\gamma^\mu\gamma^5$ are vector and axial vector operators respectively, and c_i are appropriate coefficients, which accommodate the maximum parity violation by neutrinos in $c_i = c_i'$. Note that $V \cdot V$ and $A \cdot A$ are scalars, while $V \cdot A$ and $A \cdot V$ are pseudoscalars. Having found a mechanism to successfully incorporate the P and C violation in the theory, theorists were comforted by the thought that the combined operation of CP is still held as a fundamental symmetry of nature, and there is no need to fall back all the way to CPT [5].

- CP violation.

  CP violation was discovered in 1964 by Cronin, Fitch, Christenson, and Turlay in the neutral K meson system. Scientists were motivated by the excess of K_S regeneration seen in one of the experiments [8]. Having seen the P and C invariance fallen, they decided to test CP invariance explicitly by looking for a CP violating decay $K_L \to \pi\pi$. Their initial purpose was to set the limit [9]. Instead, they discovered CP violation [10], observing the small rate

$$\frac{\Gamma(K_L \to \pi^+\pi^-)}{\Gamma(K_S \to \pi^+\pi^-)} = [(2.0 \pm 0.4) \times 10^{-3}]^2. \tag{1.7}$$

  CP violation can be incorporated in the weak transition amplitude by adding a complex phase to the elements of the quark mixing matrix $\mathbf{V}_C$ (the detailed theoretical reasoning can be found in [11], Chapter

4). However, any complex phase in 2×2 unitary matrix can be redefined away. To contain an observable complex phase, the quark mixing matrix should be at least 3×3. Kobayashi and Maskawa first noted this in 1973 [12], and pointed out that three quark generations provide a natural accommodation of the CP violation discovered in K decays. At the time of their remark, there was not yet any experimental confirmation of even the c quark! However, during the next 22 years, all the "needed" flavors, which we now call c, b, and t, and the corresponding leptons were discovered. The weak amplitude then solidified to:

$$\mathcal{A} = G \sum_{i=V,A} (\overline{U}\mathbf{V}\mathrm{O}_i D) \left(\bar{l}(1+\gamma^5 \mathrm{O}_i)\nu\right) \tag{1.8}$$

where $\overline{U} = (\overline{u}, \overline{c}, \overline{t})$, $D = (d, s, b)^T$, $\bar{l} = (\overline{e}, \overline{\mu}, \overline{\tau})$, $\nu = (\nu_e, \nu_\mu, \nu_\tau)^T$, and the Cabibbo-Kobayashi-Maskawa (CKM) quark mixing matrix is

$$\mathbf{V} = \begin{pmatrix} \mathbf{V}_{ud} & \mathbf{V}_{us} & \mathbf{V}_{ub} \\ \mathbf{V}_{cd} & \mathbf{V}_{cs} & \mathbf{V}_{cb} \\ \mathbf{V}_{td} & \mathbf{V}_{ts} & \mathbf{V}_{tb} \end{pmatrix}. \tag{1.9}$$

Particle Data Group (PDG) [13] uses the following parameterization of the CKM matrix:

$$\mathbf{V} = \begin{pmatrix} c_{12}c_{13} & s_{12}c_{13} & s_{13}e^{-i\delta_{13}} \\ -s_{12}c_{23} - c_{12}s_{23}s_{13}e^{i\delta_{13}} & c_{12}c_{23} - s_{12}s_{23}s_{13}e^{i\delta_{13}} & s_{23}c_{13} \\ s_{12}s_{23} - c_{12}c_{23}s_{13}e^{i\delta^{13}} & -c_{12}s_{23} - s_{12}c_{23}s_{13}e^{i\delta_{13}} & c_{23}c_{13} \end{pmatrix}. \tag{1.10}$$

Here $c_{ij} = \cos\theta_{ij}$ and $s_{ij} = \sin\theta_{ij}$, the angles θ_{12}, θ_{13}, and θ_{23} represent the rotation in the three-dimensional flavor space, with 1,2,3 being the family indices. The complex phase $\delta_{13} \neq 0$ incorporates CP violation.

1.1.3 Cabibbo-Kobayashi-Maskawa (CKM) matrix

The condition of unitarity in the case of 3×3 complex mixing matrix $\mathbf{V}$ should be written as:

$$\sum_{i=1}^{3} \mathbf{V}_{ji}\mathbf{V}^*_{ki} = 0 = \sum_{i=1}^{3} \mathbf{V}_{ij}\mathbf{V}^*_{ik}; \quad j,k = 1,...,3, \quad j \neq k, \tag{1.11}$$

$$\sum_{i=1}^{3} |\mathbf{V}_{ij}|^2 = 1; \quad j = 1,...,3. \tag{1.12}$$

The hierarchy between the elements of $\mathbf{V}$ was found early: e.g. the fact that the b quark prefers to decay to the c quark, rather than to the u quark, and the c quark to the s quark, rather than to the d quark. Thus, from the experiment we learn:

$$|\mathbf{V}_{ub}|^2 \ll |\mathbf{V}_{cb}|^2 \ll |\mathbf{V}_{tb}|^2 \ll 1, \tag{1.13}$$

which implies

$$s_{13} \ll s_{23} \ll s_{12} \ll 1. \tag{1.14}$$

Taking into account the unitarity constraint (1.11), Wolfenstein [14] pointed out that the CKM matrix can be expanded in the powers of $\sin\theta_C = \lambda$; up to λ^4 we have:

$$\mathbf{V} = \begin{pmatrix} 1-\frac{1}{2}\lambda^2 & \lambda & A\lambda^3(\rho - i\eta) \\ -\lambda & 1-\frac{1}{2}\lambda^2 & A\lambda^2 \\ A\lambda^3(1-\rho-i\eta) & -A\lambda^2 & 1 \end{pmatrix}. \tag{1.15}$$

The three angles and the complex phase of the PDG representation are replaced by four real quantities λ, A, ρ, and η. To be self-consistent, A, ρ, and η are required to be of order unity. Note that only the $\mathbf{V}_{td}$ and $\mathbf{V}_{ub}$ elements of (1.15) contain sizable complex phase, so the 2×2 submatrices corresponding to the transitions between the adjacent generations are approximately real, as expected.

Eq. (1.11) contains the sum of three complex numbers and can be visualized on a complex plane in the form of triangles, as the three numbers add

up to zero:

$$\begin{array}{cccc} \mathbf{V}^*_{ud}\mathbf{V}_{us}+ & \mathbf{V}^*_{cd}\mathbf{V}_{cs}+ & \mathbf{V}^*_{td}\mathbf{V}_{ts} = & 0 \\ \mathcal{O}(\lambda) & \mathcal{O}(\lambda) & \mathcal{O}(\lambda^5) & \end{array} \tag{1.16}$$

$$\begin{array}{cccc} \mathbf{V}^*_{ud}\mathbf{V}_{cd}+ & \mathbf{V}^*_{us}\mathbf{V}_{cs}+ & \mathbf{V}^*_{ub}\mathbf{V}_{cb} = & 0 \\ \mathcal{O}(\lambda) & \mathcal{O}(\lambda) & \mathcal{O}(\lambda^5) & \end{array} \tag{1.17}$$

$$\begin{array}{cccc} \mathbf{V}^*_{ud}\mathbf{V}_{ub}+ & \mathbf{V}^*_{cs}\mathbf{V}_{cb}+ & \mathbf{V}^*_{ts}\mathbf{V}_{tb} = & 0 \\ \mathcal{O}(\lambda^4) & \mathcal{O}(\lambda^2) & \mathcal{O}(\lambda^2) & \end{array} \tag{1.18}$$

$$\begin{array}{cccc} \mathbf{V}^*_{td}\mathbf{V}_{cd}+ & \mathbf{V}^*_{ts}\mathbf{V}_{cs}+ & \mathbf{V}^*_{tb}\mathbf{V}_{cb} = & 0 \\ \mathcal{O}(\lambda^4) & \mathcal{O}(\lambda^2) & \mathcal{O}(\lambda^2) & \end{array} \tag{1.19}$$

$$\begin{array}{cccc} \mathbf{V}^*_{td}\mathbf{V}_{ud}+ & \mathbf{V}^*_{ts}\mathbf{V}_{us}+ & \mathbf{V}^*_{tb}\mathbf{V}_{ub} = & 0 \\ \mathcal{O}(\lambda^3) & \mathcal{O}(\lambda^3) & \mathcal{O}(\lambda^3) & \end{array} \tag{1.20}$$

$$\begin{array}{cccc} \mathbf{V}^*_{ud}\mathbf{V}_{ub}+ & \mathbf{V}^*_{cd}\mathbf{V}_{cb}+ & \mathbf{V}^*_{td}\mathbf{V}_{tb} = & 0 \\ \mathcal{O}(\lambda^3) & \mathcal{O}(\lambda^3) & \mathcal{O}(\lambda^3) & \end{array} . \tag{1.21}$$

Below each product of matrix elements we note their magnitude in powers of λ. We observe the following (see Fig. 1.1):

- The first two triangles are extremely squashed: two sides are of order λ, the third is of order λ^5, and the ratio of them of order $\lambda^4 \sim 2 \cdot 10^{-3}$. The elements $\mathbf{V}^*_{td}\mathbf{V}_{ts}$ and $\mathbf{V}^*_{us}\mathbf{V}_{cs}$ control the K^0 and D^0 mixing. The effective weak phases there are expected to be tiny in the Standard Model.

- The third and fourth triangles – (1.18) and (1.19) – are still squashed, but less so: two sides are of order λ^2, and the third is of order λ^4. The element $\mathbf{V}^*_{ts}\mathbf{V}_{tb}$ controls the B^0_s mixing.

- The last two triangles – (1.20) and (1.21) – have sides that are all of the same order λ^3. All their angles are therefore naturally large, several $\times$ 10 degrees. The triangle corresponding to (1.21) (no. 6 in the Fig. 1.1) is precisely the one called "the Unitarity Triangle". Note, that its side $\mathbf{V}^*_{td}\mathbf{V}_{tb}$ controls the B^0_d mixing. By convention, both sides

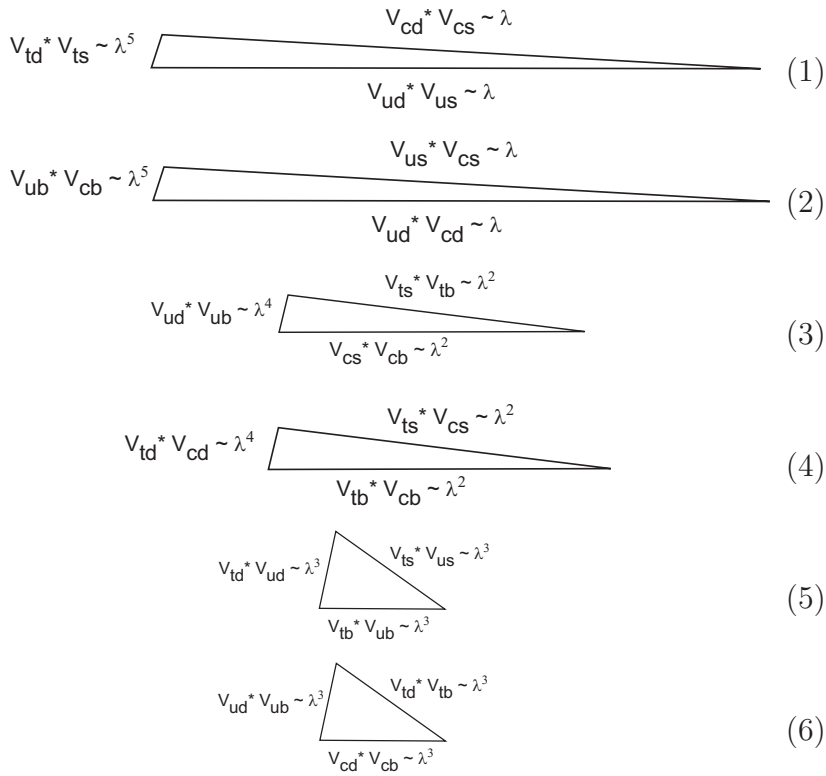

Figure 1.1: Six unitarity triangles corresponding to (1.16)-(1.21).

of (1.21) are divided by $\mathbf{V}_{cd}^* \mathbf{V}_{cb}$ (see Fig. 1.2). Various measurements effectively constrain the position of the triangle's apex, $\{\rho,\eta\}$, in the complex plane.

The Unitarity Triangle has been subject to numerous experimental tests. The current status is presented in Fig. 1.3, which shows the result of combining the constraints on $\{\rho,\eta\}$ from various measurements, as reported by the CKMfitter group in summer 2008 [15]. The detailed explanation of the fitting technique and the fit inputs can be found ibid. The observables which are connected by the CKM framework represent different dynamical regimes that proceed on very different time-scales. Yet, the results of all measurements seem to be consistent with a single position of the apex, i.e. with a single CKM phase. Thus, the CP violation observed in the interactions of elementary particles seems to exactly fit the space left for it in the Standard Model.

The six triangles represented by (1.11) have all very different angles, but

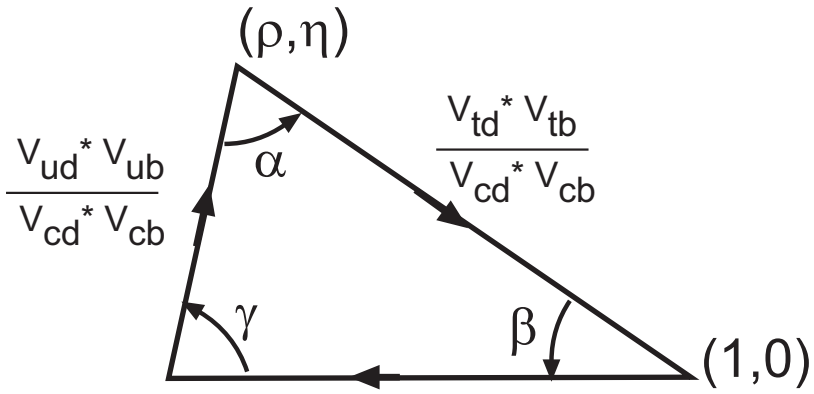

$$
\begin{aligned}
\alpha &= \arg\left(\frac{\mathbf{V}_{td}^*\mathbf{V}_{tb}}{-\mathbf{V}_{ud}^*\mathbf{V}_{ub}}\right) = \arg\left(\frac{\mathbf{V}_{ud}^*\mathbf{V}_{ub}}{\mathbf{V}_{td}^*\mathbf{V}_{tb}}\right) \\
\beta &= \pi - \arg\left(\frac{-\mathbf{V}_{td}^*\mathbf{V}_{tb}}{-\mathbf{V}_{cd}^*\mathbf{V}_{cb}}\right) = \arg\left(-\frac{\mathbf{V}_{cd}^*\mathbf{V}_{cb}}{\mathbf{V}_{td}^*\mathbf{V}_{tb}}\right) \\
\gamma &= \arg\left(\frac{\mathbf{V}_{ud}^*\mathbf{V}_{ub}}{-\mathbf{V}_{cd}^*\mathbf{V}_{cb}}\right)
\end{aligned}
$$

Figure 1.2: The Unitarity Triangle: the angles are related to the phases of the CKM matrix. Anticlockwise direction is positive.

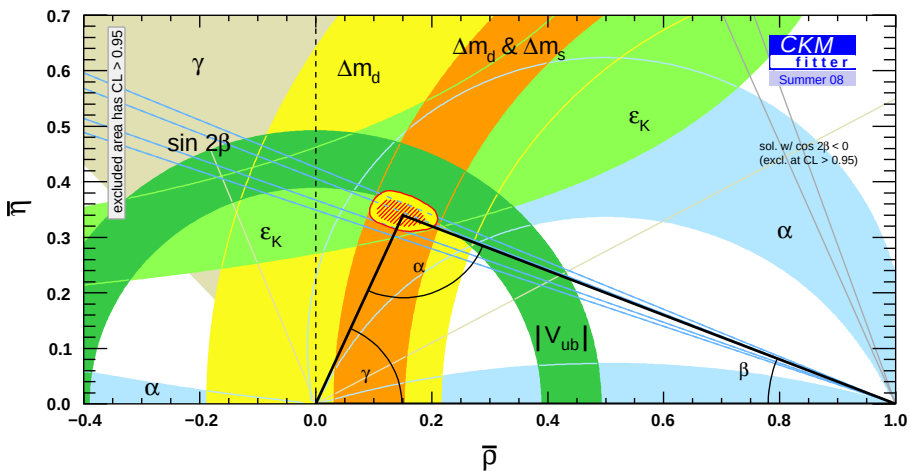

Figure 1.3: CKM fit as of summer 2008.

they all have the same area

$$\frac{1}{2}J = \frac{1}{2}|\mathrm{Im}\,\mathbf{V}^*_{mk}\mathbf{V}_{ml}\mathbf{V}_{nk}\mathbf{V}^*_{nl}| = \frac{1}{2}c^2_{13}s_{13}c_{12}s_{12}c_{23}s_{23}\sin\delta_{13}. \tag{1.22}$$

irrespective of the family indices k, l, m, n. The phase-invariant quantity J, appropriately normalized, provides a measure of the CP violation effects expected from the Standard Model [16]. To observe CP violation, one needs:

$$\theta_{12}, \theta_{13}, \theta_{23} \neq 0, \frac{\pi}{2}, \quad \text{and} \quad \delta_{13} \neq 0, \frac{\pi}{2}. \tag{1.23}$$

It is also important to note that the CP violating phase in the CKM matrix can be "rotated away" if the masses of any two up-type (down-type) quarks are degenerate. So, to realize CP violation one needs:

$$m_u \neq m_c \neq m_t \neq m_u, \quad \text{and} \quad m_d \neq m_s \neq m_b \neq m_d. \tag{1.24}$$

Conditions (1.23) and (1.24) can be summarized in a compact manner by requiring

$$\begin{aligned} d_{CP} &= 2J(m_t^2 - m_c^2)(m_c^2 - m_u^2)(m_u^2 - m_t^2) \\ &\times (m_b^2 - m_s^2)(m_s^2 - m_d^2)(m_d^2 - m_b^2) \neq 0. \end{aligned} \tag{1.25}$$

Justification for this requirement can be found in [16] and [11].

Taking into account the observed hierarchy between the CKM elements (1.14), the value of invariant J in the Standard Model is $J \approx 2 \cdot 10^{-3} \sin\delta_{13}$ [17]. Assuming rotation angles θ_{ij} and the CKM phase δ_{13} to be free parameters, maximal CP violating effects in the Standard Model were observed if we had

$$\theta_{12} \approx \theta_{13} \approx \theta_{23} \approx \frac{\pi}{4}, \text{ and } \sin\delta_{13} = 1. \tag{1.26}$$

It is easy to see from (1.22) that in this case we would have $J = J_{max} \approx 5 \cdot 10^{-2}$. So, maximal CP violation does not seem to be realized in nature, with invariant J being roughly order of magnitude away from its maximal possible value.

1.2 Particle-antiparticle mixing and CP violation

In this section we review the general phenomenological implications of the imaginary couplings in (1.9), following [11] and [18]. The particle-antiparticle mixing provides a good environment for CP violation to manifest itself, since such a mixing naturally brings into interference different amplitudes with different complex phases. Thus, the types of CP violation and the corresponding CP violation observables are conveniently defined in terms of the mixing parameters.

We will discuss mixing in neutral $P^0 - \overline{P}^0$ system in general. Specializations to particular systems, K^0, D^0, or B^0, can be found in literature [13, 18, 19]. Mixing is characterized by the change of the flavour quantum number F by two units, $\Delta F = 2$, which can occur due to:

- two-step transition via common intermediate state f, $P^0 \overset{\Delta F=1}{\longleftrightarrow} f \overset{\Delta F=1}{\longleftrightarrow} \overline{P}^0$. f can be either on-shell (e.g. $\pi\pi$ state for kaons), or virtual off-shell state;

- one-step transition $P^0 \overset{\Delta F=2}{\longleftrightarrow} \overline{P}^0$, as e.g. shown in Fig. 1.4 for neutral K ($F \equiv S$), D ($F \equiv C$) and B ($F \equiv B$) systems.

The time evolution of the correlated $P^0 - \overline{P}^0$ state $\Psi(t)$ obeys the Schrödinger equation

$$i\hbar \frac{\partial}{\partial t} \Psi(t) = \mathrm{H}\Psi(t), \tag{1.27}$$

where H is the Hamiltonian of the system. The full dependence of $\Psi(t)$ cannot be obtained exactly, as this requires to get the strong dynamics under control. Therefore, we restrict $\Psi(t)$ to the subspace of P^0 and $\overline{P}^0$:

$$|\Psi(t)\rangle = a(t)|P^0\rangle + b(t)|\overline{P}^0\rangle, \tag{1.28}$$

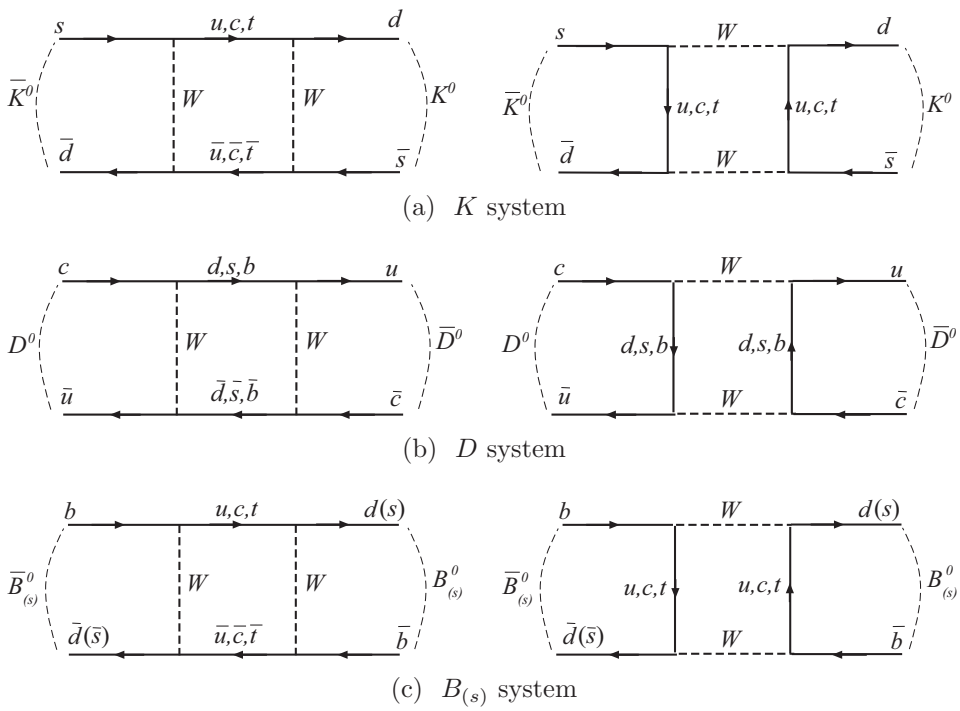

Figure 1.4: The celebrated box diagrams giving rise to $\Delta F = 2$ transitions in K ($F \equiv S$), D ($F \equiv C$) and $B_{(s)}$ ($F \equiv B$) systems.

or, in matrix notation:

$$\Psi(t) = \begin{pmatrix} a(t) \\ b(t) \end{pmatrix}.$$

Then, the corresponding matrix for H is given by:

$$\mathrm{H} = \mathbf{M} - \frac{i}{2}\mathbf{\Gamma} = \begin{pmatrix} M_{11} - \frac{i}{2}\Gamma_{11} & M_{12} - \frac{i}{2}\Gamma_{12} \\ M_{21} - \frac{i}{2}\Gamma_{21} & M_{22} - \frac{i}{2}\Gamma_{22} \end{pmatrix}, \tag{1.29}$$

and accounts for propagation (M) and decay (Γ) of the system. CPT invariance (see Section 1.1.1) implies the following relations among the elements of the mass matrix [20]:

$$\begin{aligned} \text{CPT invariance} \quad \leftrightarrow \quad & M_{11} = M_{22}, \quad \Gamma_{11} = \Gamma_{22}, \\ & M_{21} = M_{12}^*, \quad \Gamma_{21} = \Gamma_{12}^*. \end{aligned} \tag{1.30}$$

The mixing is described in (1.29) by the non-zero off-diagonal elements: $M_{12} - i/2\,\Gamma_{12} \neq 0$. Due to mixing, the CP eigenstates of a correlated pair

do not correspond to the strong eigenstates:

$$|P_1\rangle = p|P^0\rangle + q|\overline{P}^0\rangle, \tag{1.31}$$

$$|P_2\rangle = p|P^0\rangle - q|\overline{P}^0\rangle. \tag{1.32}$$

Here

$$\left(\frac{q}{p}\right)^2 = \frac{M_{12}^* - \frac{i}{2}\Gamma_{12}^*}{M_{12} - \frac{i}{2}\Gamma_{12}}, \tag{1.33}$$

or

$$\frac{q}{p} = \sqrt{\frac{M_{12}^* - \frac{i}{2}\Gamma_{12}^*}{M_{12} - \frac{i}{2}\Gamma_{12}}}, \tag{1.34}$$

where the positive sign is conventionally chosen. CP invariance requires that nature treats P^0 and $\overline{P}^0$ "on equal footing", e.g. $q = p$ ($q/p = 1$), and $|P_1\rangle$ and $|P_2\rangle$ are orthogonal: $\langle P_1|P_2\rangle = 0$.

The discovery of CP violation by Cronin and Fitch (1.7) can be summarized by saying that the quantum mechanical state K_L contains a small admixture $\epsilon_1 = \epsilon$ of a CP even component, K_1, in addition to its dominant CP odd part, K_2:

$$\langle K_L| = \frac{1}{\sqrt{1+|\epsilon|^2}}(\langle K_2| + \epsilon\langle K_1|). \tag{1.35}$$

CPT invariance then requires that the K_S state should, in turn, contain the admixture of K_2 of the same amount $\epsilon_2 = \epsilon$:

$$\langle K_S| = \frac{1}{\sqrt{1+|\epsilon|^2}}(\langle K_1| + \epsilon\langle K_2|). \tag{1.36}$$

Hence, in terms of (1.31) and (1.32), CP violation is described by $\langle K_L|K_S\rangle \neq 0$ or $(q/p)_K \neq 1$, which implies that the amplitudes M_{12}^K and/or Γ_{12}^K *acquire complex phases*, as expected from Section 1.1.2.

Let us define for future convenience $\Delta M \equiv M_2 - M_1$, $\Delta\Gamma \equiv \Gamma_1 - \Gamma_2$ (so that both ΔM and $\Delta\Gamma$ are positive in kaon system), $\Gamma \equiv (\Gamma_1 + \Gamma_2)/2$, $x \equiv \Delta M/\Gamma$, $y \equiv \Delta\Gamma/(2\Gamma)$. Then it is known from experiment that in the B_d meson system $x_d \approx 0.77$, and conservatively $y_d < 0.1$ [21]. Therefore $\Delta\Gamma_d \ll \Delta M_d$, which model-independently implies $|\Gamma_{12}^d| \ll |M_{12}^d|$. For the B_s

system, $\Delta\Gamma_s \ll \Gamma_s \ll \Delta M_s$, so the approximation $|\Gamma_{12}^s| \ll |M_{12}^s|$ holds even better. So, for both B_d and B_s systems we can expand the eigenvalues and q/p in powers of a small parameter

$$a = \left|\frac{\Gamma_{12}}{M_{12}}\right| \sin\phi. \tag{1.37}$$

Keeping only the terms of order a we obtain [22]:

$$\begin{aligned} &\Delta M = 2|M_{12}|, \quad \Delta\Gamma = 2|\Gamma_{12}|\cos\phi, \\ &\text{and} \quad \frac{q}{p} \approx -e^{-i\phi_M}\left[1 - \frac{a}{2}\right], \end{aligned} \tag{1.38}$$

In (1.37) and (1.38) ϕ is the relative phase between Γ_{12} and M_{12}:

$$\frac{M_{12}}{\Gamma_{12}} = -\left|\frac{M_{12}}{\Gamma_{12}}\right| e^{i\phi}, \tag{1.39}$$

and ϕ_M is the relative phase between q and p ("mixing phase"):

$$\phi_M = \arg\left(\frac{q}{p}\right). \tag{1.40}$$

For both B_q systems ($q = d, s$) the Standard Model predicts to a good approximation:

$$\phi^q \approx 0, \quad \text{and} \quad \phi_M^q \approx \arg\left(\sqrt{\frac{M_{12}^q}{M_{12}^{q*}}}\right) = \arg\left(M_{12}^q\right). \tag{1.41}$$

The only source of complex phase in the Standard Model is the CKM elements. As the Standard Model prediction for M_{12}^q is dominated by the heavy quark in the box diagrams of Fig. 1.4 [19], we write:

$$M_{12}^q \sim (\mathbf{V}_{tq}\mathbf{V}_{tb}^*)^2. \tag{1.42}$$

Using (1.15), with precision up to λ^4 we can write for the B_d system:

$$\phi_M^d = \arg\left((\mathbf{V}_{td}\mathbf{V}_{tb}^*)^2\right) \approx 2\arg\left(\mathbf{V}_{td}\right), \tag{1.43}$$

and for the B_s system:

$$\phi_M^s = \arg\left(\mathbf{V}_{ts}\mathbf{V}_{tb}^*\right) \approx 0. \tag{1.44}$$

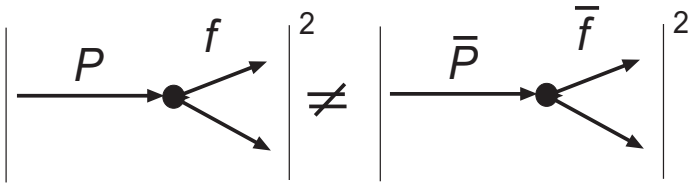

(a) Direct CP violation.

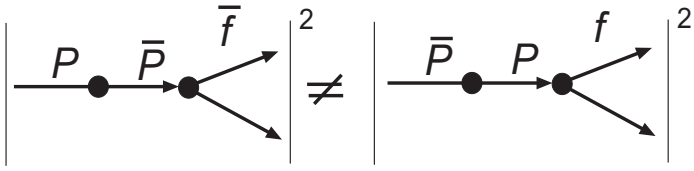

(b) CP violation in mixing.

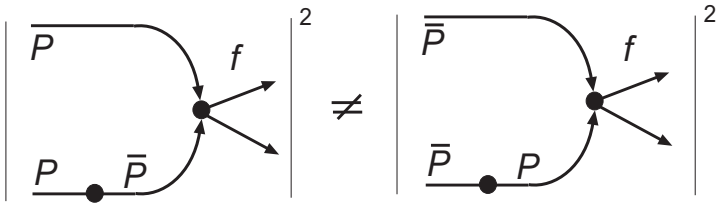

(c) CP violation in interference.

Figure 1.5: Three cases of CP violation: direct, in mixing, in interference.

The time evolution of states starting out as pure P^0 or $\overline{P}^0$ is obtained by noting the time evolution of the mass eigenstates:

$$|P_1(t)\rangle = e^{-i(M_1 - \frac{i}{2}\Gamma_1)t}|P_1(0)\rangle, \tag{1.45}$$

$$|P_2(t)\rangle = e^{-i(M_2 - \frac{i}{2}\Gamma_2)t}|P_2(0)\rangle, \tag{1.46}$$

and solving the system of (1.31) and (1.32) for $|P^0(t)\rangle$ and $|\overline{P}^0(t)\rangle$. We obtain:

$$|P^0(t)\rangle = f_+(t)|P^0\rangle + \frac{q}{p}f_-(t)|\overline{P}^0\rangle, \tag{1.47}$$

$$|P^0(t)\rangle = f_+(t)|P^0\rangle + \frac{q}{p}f_-(t)|\overline{P}^0\rangle, \tag{1.48}$$

where

$$f_\pm(t) = \frac{1}{2}e^{-iM_1 t}e^{-\frac{1}{2}\Gamma_1 t}\left[1 \pm e^{-i\Delta M t}e^{\frac{1}{2}\Delta\Gamma t}\right]. \tag{1.49}$$

The decay rate evolution is in general rather complex. We will consider three simple, complementary cases:

a) No oscillations occur, i.e. $\Delta M = \Delta\Gamma = 0$. The time evolution is purely exponential in t. Let us denote by $\mathcal{A}(f)$ the transition rate of the decay $P \to f$, and by $\overline{\mathcal{A}}(\overline{f})$ the transition rate of the charge-conjugate decay $\overline{P} \to \overline{f}$. CP violation can still arise if $|\mathcal{A}(f)| \neq |\overline{\mathcal{A}}(\overline{f})|$ (see Fig. 1.5(a)). This is called *direct* CP violation, and can be observed as a decay rate asymmetry:

$$A_f^{dir} = \frac{\Gamma(P \to f) - \Gamma(\overline{P} \to \overline{f})}{\Gamma(P \to f) + \Gamma(\overline{P} \to \overline{f})} = \frac{|\mathcal{A}_f|^2 - |\overline{\mathcal{A}}_{\overline{f}}|^2}{|\mathcal{A}_f|^2 + |\overline{\mathcal{A}}_{\overline{f}}|^2}. \tag{1.50}$$

b) Flavour-specific decays are those coming from either P^0 or $\overline{P}^0$ but not from both:

$$P^0 \to f \nleftarrow \overline{P}^0 \text{ or } P^0 \nrightarrow \overline{f} \leftarrow \overline{P}^0, \tag{1.51}$$

i.e. those for which

$$|\mathcal{A}_{\overline{f}}| = |\overline{\mathcal{A}}_f| = 0, \qquad |\mathcal{A}_f| = |\overline{\mathcal{A}}_{\overline{f}}| \equiv \mathcal{A}, \tag{1.52}$$

see Fig. 1.5(b). The last equality in (1.52) is enforced by CPT invariance. Prominent flavour-specific channels for neutral mesons like K, D, B are provided by the semileptonic decays, with $f = l^+X$, $\overline{f} = l^-X$.

It can be shown [11] that the flavor-specific decay rates evolve with time as follows:

$$\Gamma(P^0(t) \to l^+ + X) \sim e^{-\Gamma_1 t} K_+(t) |\mathcal{A}|^2, \tag{1.53}$$

$$\Gamma(P^0(t) \to l^- + X) \sim e^{-\Gamma_1 t} K_-(t) \left|\frac{q}{p}\right| |\mathcal{A}|^2, \tag{1.54}$$

$$\Gamma(\overline{P}^0(t) \to l^- + X) \sim e^{-\Gamma_1 t} K_+(t) |\mathcal{A}|^2, \tag{1.55}$$

$$\Gamma(\overline{P}^0(t) \to l^+ + X) \sim e^{-\Gamma_1 t} K_-(t) \left|\frac{p}{q}\right| |\mathcal{A}|^2, \tag{1.56}$$

with

$$K_\pm(t) = 1 + e^{\Delta\Gamma t} \pm 2\, e^{\frac{1}{2}\Delta\Gamma t} \cos \Delta M t. \tag{1.57}$$

From (1.53)-(1.56) it is clear that CP violation due to $|q/p| \neq 1$ should manifest itself as a decay rate asymmetry between the mixed $P^0 \to \overline{P}^0 \to l^- X$ and $\overline{P}^0 \to P^0 \to l^+ X$, i.e. as a *wrong-sign semileptonic asymmetry*:

$$\begin{aligned} a_{SL} &= \frac{\Gamma(P^0(t) \to l^- X) - \Gamma(\overline{P}^0(t) \to l^+ X)}{\Gamma(P^0(t) \to l^- X) + \Gamma(\overline{P}^0(t) \to l^+ X)} \\ &= \frac{|p/q|^2 - |q/p|^2}{|p/q|^2 + |q/p|^2} = \frac{1 - |q/p|^4}{1 + |q/p|^4}. \end{aligned} \tag{1.58}$$

Note that a_{SL} is independent of time. Taking into account (1.38) and (1.37), we find:

$$a_{SL} = a + \mathcal{O}(a^2) = \left| \frac{\Gamma_{12}}{M_{12}} \right| \sin\phi = \frac{\Delta\Gamma}{\Delta M} \tan\phi. \tag{1.59}$$

So, the measurement of the wrong-sign semileptonic asymmetry allows to access the phase ϕ, if $\Delta\Gamma$ and ΔM are constrained by other experiments.

c) Flavour-nonspecific decays are those fed by both P^0 and $\overline{P}^0$:

$$P^0 \to f \leftarrow \overline{P}^0. \tag{1.60}$$

Here the phase $\phi_M = \arg(q/p)$ becomes observable through the *interference between the decay and mixing* (see Fig. 1.5(c)). By solving Schrödinger equation using (1.38), one can find [22]:

$$\begin{aligned} \Gamma(B_s(t) \to f) &= N_f |\mathcal{A}_f|^2 \frac{1 + |\lambda_f|^2}{2} e^{-\Gamma t} \\ &\times \left[\cosh\frac{\Delta\Gamma t}{2} + C_f \cos(\Delta M t) + A_{\Delta\Gamma} \sinh\frac{\Delta\Gamma t}{2} + S_f \sin(\Delta M t) \right], \end{aligned} \tag{1.61}$$

$$\begin{aligned} \Gamma(\overline{B}_s(t) \to f) &= N_f |\mathcal{A}_f|^2 \frac{1 + |\lambda_f|^2}{2} (1 + a) e^{-\Gamma t} \\ &\times \left[\cosh\frac{\Delta\Gamma t}{2} - C_f \cos(\Delta M t) + A_{\Delta\Gamma} \sinh\frac{\Delta\Gamma t}{2} - S_f \sin(\Delta M t) \right], \end{aligned} \tag{1.62}$$

where

$$\lambda_f \equiv \frac{q}{p}\frac{\overline{\mathcal{A}}_f}{\mathcal{A}_f}, \tag{1.63}$$

$$C_f \equiv \frac{1-|\lambda_f|^2}{1+|\lambda_f|^2} = \frac{|\mathcal{A}_f|^2 - |\overline{\mathcal{A}}_f|^2}{|\mathcal{A}_f|^2 + |\overline{\mathcal{A}}_f|^2}, \tag{1.64}$$

$$A_{\Delta\Gamma} \equiv -\frac{\mathrm{Re}\,\lambda_f}{1+|\lambda_f|^2}, \tag{1.65}$$

$$S_f \equiv -\frac{2\mathrm{Im}\,\lambda_f}{1+|\lambda_f|^2}, \tag{1.66}$$

and N_f is the time-independent normalization factor. The quantity $A_{\Delta\Gamma}$ plays a role only if $\Delta\Gamma$ is sizable, and is not interesting for the present discussion. The time-dependent asymmetry constructed from these rates reads

$$\begin{aligned} a_f(t) &= \frac{\Gamma(B_s(t)\to f) - \Gamma(\overline{B}_s(t)\to f)}{\Gamma(B_s(t)\to f) + \Gamma(\overline{B}_s(t)\to f)} \\ &\sim C_f \cos\Delta M t + S_f \sin\Delta M t. \end{aligned} \tag{1.67}$$

Several cases are possible. Assuming $\phi = 0$ in the Standard Model, direct CP violation $|\mathcal{A}_f| \neq |\overline{\mathcal{A}}_f|$ is manifested as $C_f \neq 0$. Proper CP violation in interference due to $\phi_M = \arg(q/p) \neq 0$ is manifested as $S_f \neq 0$. Thus, CP violation in interference allows to access both the direct asymmetry and the asymmetry due to $\phi_M \neq 0$ by fitting the lifetime dependence of the asymmetry to (1.67).

Note that the time-integrated version of (1.50) is just

$$A_f^{dir} = \frac{N(P\to f) - N(\overline{P}\to \overline{f})}{N(P\to f) + N(\overline{P}\to \overline{f})}. \tag{1.68}$$

If the mode is self-tagging (as e.g. $B^\pm \to J/\psi K^\pm$), direct CP asymmetry boils down to a simple charge asymmetry between the event yields.

1.3 More CP violation needed!

In spite of the tremendous success of the CKM description, there exist reasons to actively continue the CP violation studies. One of them is theoretical, another comes from observations.

Theoretical ground. The Standard Model solidified around 30 years ago, successfully accommodating C, P, and CP violation, and surviving the toughest experimental scrutinies possible with the available tools. Although experimentally successful, the Standard Model has some methodological issues. There is a lack of "naturalness" in the observed hierarchy of coupling constants [23], and the irritating lack of unification between the fundamental forces [24]. A number of New Physics theories have been proposed to address these issues. The most cited are the Supersymmetric theories (SUSY) [25], which overcome the methodological limitations of the Standard Model at the price of introducing additional free parameters. SUSY theories postulate a fundamental symmetry between fermions and bosons, so that every particle has a superpartner − an *sparticle*. As a result, the particle content of the theory doubles.

Contributing to the virtual intermediate states, SUSY particles would bring in new complex couplings that add to the effect from the Standard Model δ_{13}. So, in general, the New Physics models aiming to cure the methodological defects of the Standard Model introduce new CP violation phases. We will consider an example in due course.

Observational ground. Assuming that all the matter we observe around us is only the remnant of a tiny mismatch between matter and antimatter in the hot plasma of the early universe, the actual matter-antimatter asymmetry should have been

$$\eta = \frac{n_B - \overline{n}_B}{s} \sim \text{few} \times 10^{-10}, \tag{1.69}$$

where n_B and $\overline{n}_B$ denote the density of baryons and anti-baryons, and s is the density of Cosmic Microwave Background (CMB) photons. Already in 1967 Sakharov specified the conditions for a viable mechanism of baryon number generation in the early universe (*baryogenesis*) from the initial state with zero net baryon number [26]:

- There are baryon number violating transitions, which is obvious but

not sufficient, since for every baryon number changing transition $N \to f$ there is a CP conjugate one $\overline{N} \to \overline{f}$, and no net asymmetry can develop unless...

- There is CP violation:

  $$\Gamma(N \to f) \neq \Gamma(\overline{N} \to \overline{f}).$$

  Still, even this is not enough, since it can be shown that in the state of thermal equilibrium the net baryon charge remains zero due to the time-reversed reactions $f \to N$ and $\overline{f} \to \overline{N}$. In other words, assuming CPT invariance, it is impossible to realize CP violation unless T is also violated, i.e. ...

- The system remains out of thermal equilibrium, thus acquiring an "arrow of time".

The Standard Model, in conjunction with the Big Bang cosmology, seems to offer all three necessary ingredients. Baryon number violation is believed to have taken place through non-perturbative weak interaction processes in the hot plasma of the early universe [27]. The out-of-equilibrium state is provided by the electroweak phase transition when the Higgs field acquires its vacuum expectation value. The "new" vacuum nucleates in bubbles, which expand and drive the Big Bang plasma out of equilibrium [27]. The complex phase in the CKM matrix provides CP violation. However, the "conventional wisdom" denies that the observed baryon asymmetry (1.69) could have been generated all from the CKM complex phase. The baryon asymmetry expected from the Standard Model should be proportional to the quantity d_{CP} from (1.25). Since the asymmetry is a dimensionless number, d_{CP} should be divided by something with dimensions of (mass)^{12}. The natural mass parameter at the temperature of the electroweak phase transition: $T_{EW} \sim 100$ GeV, seems to be the temperature itself, so the asymmetry is at

most

$$\eta \lesssim \frac{d_{CP}}{T_{EW}^{12}} \sim 10^{-20}. \tag{1.70}$$

Were the maximal CP violation in the Standard Model realized according to (1.26), the prediction (1.70) would increase by an order of magnitude at most, remaining far below the observed value (1.69). Thus, the Standard Model as it stands, with a single CP violating phase, is believed to be unable to account for the observed matter-antimatter asymmetry of the Universe. The new sources of CP violation, usually parameterized in form of additional CP violating phases, have to be searched for. Such phases naturally arise in many New Physics models, which also address methodological defects of the Standard Model. In conclusion, both theory and cosmological observations demand the existence of new sources of CP violation.

1.4 Observables and motivation

Nowadays, the goal of CP studies is to discover non-Standard Model CP violation (ideally), or at least to constrain the New Physics phases, introduced either model-independently or in the frame of a particular New Physics construction. The general strategy of our search for non-Standard Model effects is as follows: we choose an observable theoretically constrained to be close to zero in the Standard Model. Then, any non-Standard Model enhancements can become noticeable. For this analysis we select the direct CP asymmetry in the $B^+ \to J/\psi K^+$ transition, $A^{dir}_{J/\psi K^+}$. Additionally, we measure the direct asymmetry in $B^+ \to J/\psi \pi^+$ transition, $A^{dir}_{J/\psi \pi^+}$.

In this section we consider in more detail the motivation, the Standard Model estimates, and the expectations from New Physics.

1.4.1 Direct CP asymmetry in the $B^+ \to J/\psi K^+$ decay

The measurement of direct CP asymmetry in the $B^+ \to J/\psi K^+$ decay has a long history. This asymmetry is defined as a charge asymmetry between

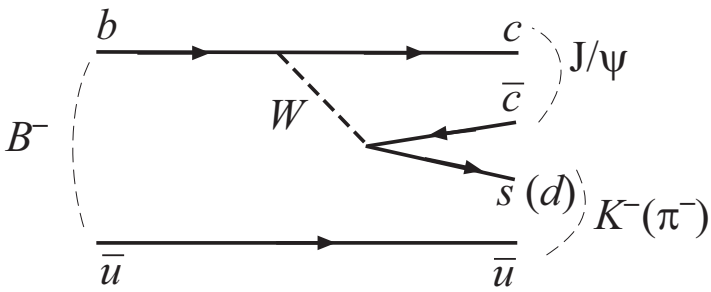

(a) Tree

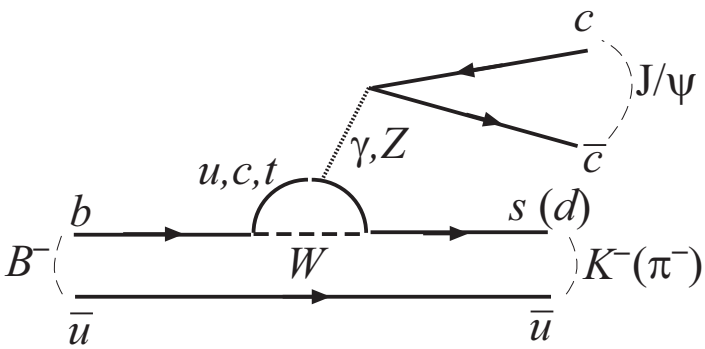

(b) Penguin

Figure 1.6: $B^+ \to J/\psi K^+(\pi^+)$: Standard Model diagrams.

the event yields of $B^-(b\overline{u}) \to J/\psi K^-$ and $B^+(\overline{b}u) \to J/\psi K^+$ decays:

$$\begin{aligned} A_{CP}(B^+ \to J/\psi(1S)K^+) &\equiv A^{dir}_{J/\psi K^+} \\ &= \frac{N(B^- \to J/\psi K^-) - N(B^+ \to J/\psi K^+)}{N(B^- \to J/\psi K^-) + N(B^+ \to J/\psi K^+)}. \end{aligned} \tag{1.71}$$

The $B^+ \to J/\psi K^+$ decay is governed by the $b \to sc\overline{c}$ transition, which occurs via either $b \to c$ tree or $b \to s$ penguin amplitude (see Fig. 1.6). In the Standard Model, the tree (T) and penguin (P) amplitudes are [21]:

$$T_{b\to c} = T\,\mathbf{V}_{cb}\mathbf{V}^*_{cs} = \mathcal{O}(\lambda^2), \tag{1.72}$$

$$P_{b\to s} = F_u\mathbf{V}_{ub}\mathbf{V}^*_{us} + F_c\mathbf{V}_{cb}\mathbf{V}^*_{cs} + F_t\mathbf{V}_{tb}\mathbf{V}^*_{ts} \tag{1.73}$$

$$= (F_u - F_c)\mathbf{V}_{ub}\mathbf{V}^*_{us} + (F_t - F_c)\mathbf{V}_{tb}\mathbf{V}^*_{ts} \tag{1.74}$$

$$= P^u_{b\to s}\mathbf{V}_{ub}\mathbf{V}^*_{us} + P^t_{b\to s}\mathbf{V}_{tb}\mathbf{V}^*_{ts} \tag{1.75}$$

$$= \mathcal{O}(\lambda^4) \qquad + \mathcal{O}(\lambda^2).$$

where the unitarity of the CKM matrix is used in (1.74). The only source of a sizable phase is the $\mathbf{V}_{ub}\mathbf{V}^*_{us}$ combination, which is strongly suppressed. The direct CP violation in the $b \to sc\overline{c}$ transition can be measured either in interference between the decay and mixing by fitting the lifetime dependence of the asymmetry to (1.67), or using direct decay. In both cases we expect

$$C_{b\to sc\overline{c}} \approx A^{dir}_{b\to sc\overline{c}} \approx 0. \tag{1.76}$$

Any New Physics in the $b \to s$ penguin can easily "spoil" (1.76).

The interest in the $b \to s$ penguin was triggered by the alarming pattern of deviations from the Standard Model observed in the $B \to K\pi$ decays. The complex of these deviations was collectively dubbed "$B \to K\pi$ puzzle". The observables in the $B \to K\pi$ sector (decay rates and CP asymmetries) receive there leading contributions from the gluonic $b \to s(u\overline{u})$ and $b \to s(d\overline{d})$ penguins [28].

The current set of $B \to K\pi$ data is shown in Table 1.1 (averaged in Heavy Flavor Averaging Group (HFAG) [21], reproduced from [29]). The

Measurement	BaBar	Belle	CLEO	Average
$\mathrm{Br}(K^0\pi^+)$	$23.9 \pm 1.1 \pm 1.0$	$22.8^{+0.8}_{-0.7} \pm 1.3$	$18.8^{+3.7+2.1}_{-3.3-1.8}$	23.1 ± 1.0
$\mathrm{Br}(K^+\pi^0)$	$13.6 \pm 0.6 \pm 0.7$	$12.4 \pm 0.5 \pm 0.6$	$12.9^{+2.4+1.2}_{-2.2-1.1}$	12.9 ± 0.6
$\mathrm{Br}(K^+\pi^-)$	$19.1 \pm 0.6 \pm 0.6$	$19.9 \pm 0.4 \pm 0.8$	$18.0^{+2.3+1.2}_{-2.1-0.9}$	19.4 ± 0.6
$\mathrm{Br}(K^0\pi^0)$	$10.3 \pm 0.7 \pm 0.6$	$19.2 \pm 0.7^{+0.6}_{-0.7}$	$12.8^{+4.0+1.7}_{-3.3-1.4}$	9.9 ± 0.6
$A_{CP}(K^0\pi^+)$	$-0.029 \pm 0.039 \pm 0.010$	$0.03 \pm 0.03 \pm 0.01$	$0.18 \pm 0.24 \pm 0.02$	0.009 ± 0.025
$A_{CP}(K^+\pi^0)$	$-0.030 \pm 0.039 \pm 0.010$	$0.07 \pm 0.03 \pm 0.01$	$-0.29 \pm 0.23 \pm 0.02$	0.050 ± 0.025
$A_{CP}(K^+\pi^-)$	$-0.107 \pm 0.018^{+0.007}_{-0.004}$	$-0.093 \pm 0.018 \pm 0.008$	$-0.04 \pm 0.16 \pm 0.02$	$-0.097 \pm 0.012^*$
$A_{CP}(K^0\pi^0)$	$-0.24 \pm 0.15 \pm 0.03$	$-0.05 \pm 0.14 \pm 0.05$		-0.14 ± 0.11
$S^{**}_{K_S\pi^0}$	$0.40 \pm 0.23 \pm 0.03$	$0.33 \pm 0.35 \pm 0.08$		0.38 ± 0.19

Table 1.1: Current experimental data for $B \to K\pi$. The branching ratios are in 10^{-6}. The average values are given by HFAG, updated by end 2007 [21]. Reproduced from [29].

*This average also includes CDF result: $-0.086 \pm 0.023 \pm 0.009$.

**S_f has been defined in (1.66).

problem initially was seen in the significant difference between the following observables:

$$R_c \equiv 2\frac{\mathrm{Br}(B^+ \to K^+\pi^0)}{\mathrm{Br}(B^+ \to K^0\pi^+)}, \tag{1.77}$$

$$R_n \equiv \frac{1}{2}\frac{\mathrm{Br}(B^0 \to K^+\pi^-)}{\mathrm{Br}(B^0 \to K^0\pi^0)}, \tag{1.78}$$

where the factors of 2 and 1/2 have been introduced to absorb the $\sqrt{2}$ factors originating from the wave functions of the neutral pions. In the Standard Model $R_c \approx R_n$, which basically follows from the isospin invariance [30]. As of 2004, the measured values of $R_c = 1.15 \pm 0.12$ and $R_n = 0.78 \pm 0.10$ showed 2.4σ difference [31]. As time passes R_c and R_n were getting closer to each other [32]. Most recent data (see Table 1.1) show $R_c = 1.12 \pm 0.05$ and $R_n = 0.98 \pm 0.07$, consistent with the Standard Model prediction.

However, the puzzle became more severe in the difference between the direct CP asymmetries in $B^+ \to K^+\pi^0$ and $B^0 \to K^+\pi^-$ decays, $\Delta A_{CP} \equiv A_{CP}(K^+\pi^0) - A_{CP}(K^+\pi^-)$. Contrary to the expectations, the significance of ΔA_{CP} has been increasing over the years. From the current HFAG averages (see Table 1.1) it is $\Delta A_{CP} = 0.147 \pm 0.028$, surpassing 5σ barrier.

Recently, an analytic calculation of a combined set of Standard Model and New Physics parameters in the quark diagram approach was performed

[29]. No specific New Physics model was assumed. The authors report that the consistent solution given the data of Table 1.1 is possible only if the large New Physics amplitude and the sizable associated phase are introduced. The conclusions of [29] basically repeat the conclusions of previous numerical model-independent analyzes [28, 33], suggesting the New Physics enhancement of the electroweak penguin amplitude, or New Physics entering in the color-suppressed tree amplitude. Generally, the electroweak penguin is considered better candidate for the New Physics to surface.

Further implications of possible New Physics enhancement of the electroweak penguin were analyzed in a paper by Hou [34]. The author pointed out that such an enhancement should generate sizable direct CP violating asymmetry in $B^+ \to J/\psi K^+$, and suggested this mode as especially suitable to verify (1.76). Due to the CKM-allowed tree diagram, the statistics is expected to be high. Also, the decay may be triggered in the channel with $J/\psi \to \mu\mu$ using easily identifiable muons.

Having chosen the mode, it makes sense to specify the Standard Model prediction more accurately. Hou parameterizes the decay amplitude as

$$\mathcal{A}(\overline{B} \to J/\psi \overline{K}) = ae^{i\delta} + be^{-i\phi}, \tag{1.79}$$

where the first term carries the strong phase difference, and the second the weak phase difference. Then, the penguin pollution of (1.76) in the Standard Model is [34]:

$$C^{SM}_{J/\psi K^0} \equiv A^{SM}_{J/\psi K^+} \approx -2\frac{b}{a}\sin\phi\sin\delta = \mathcal{O}(0.003). \tag{1.80}$$

Hou estimates the penguin fraction b/a from the decay $B \to \phi K$, dominated by the penguin transition $b \to s(s\overline{s})$. The strong phase is estimated from the angular analysis of the decay $B \to J/\psi K^*$ to be $\delta \sim 30°$. Finally, the CKM pattern is used: $\phi \approx \arg \mathbf{V}_{ub} \approx \gamma$.

To estimate possible New Physics enhancement of the direct asymmetry in the $B^+ \to J/\psi K^+$ decay, Hou considers a specific flavor changing neutral coupling between b and s quarks, $b \to sZ'$ (see Fig. 1.7). This coupling

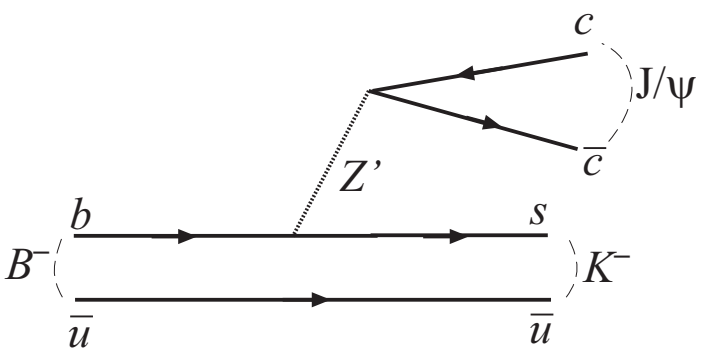

Figure 1.7: $B^+ \to J/\psi K^+$: hypothetical $b \to sZ'$ transition.

arises phenomenologically in some SUSY constructions [35]. The complex coupling of Z' to b and s, B_{sb}, introduces a new phase $\phi_{Z'} = \arg(B_{sb})$, which enhances $C_{J/\psi K^0}$ via the common weak phase $\phi = \phi^{SM} + \phi_{Z'}$. The authors of [31] show that the parameters of the model may be chosen to explain the $B \to K\pi$ puzzle, predicting at the same time large direct CP asymmetry in $B^+ \to K^+\pi^0$. Hou estimates that, depending on the strong phase δ, the corresponding direct CP asymmetry in $B^+ \to J/\psi K^+$ may be enhanced to $A^{dir}_{J/\psi K^+} = \mathcal{O}(0.05)$.

Present status

The $b \to sc\bar{c}$ transition was accessed at B factories using both lifetime analysis of the decays to CP eigenstates using (1.67), and the direct decays. For the lifetime analysis, as of end 2007, HFAG reports averages over the modes with $\eta_f = -1$: $J/\psi K^0_S$, $\psi(2S)K^0_S$, $\chi_{c1}K^0_S$, and $\eta_c K^0_S$, and with $\eta_f = +1$: $J/\psi K^0_L$. The HFAG sources and the averages are reproduced in Table 1.2. See [21] for the breakdown of the results in each charmonium-kaon final state. The results using the direct decay $B^+ \to J/\psi K^+$ are reproduced from PDG 2007 [13] in Table 1.3. As one can see, even the level of uncertainty necessary to establish the 2% asymmetry expected from the $b \to sZ'$ coupling has not been reached yet by the B factories.

Experiment	$N(B\overline{B})$	$C_{b\to sc\bar{c}}{}^{*}$
	$J/\psi K^0$	
BaBar [36]	384M	$+0.049 \pm 0.022 \pm 0.017$
Belle $J/\psi K^0$ [37]	535M	$-0.018 \pm 0.021 \pm 0.014$
Belle $\psi(2S)K^0$ [38]	657M	$-0.039 \pm 0.069 \pm 0.049$
Average		$\mathbf{0.012 \pm 0.020}$

Table 1.2: Measurements of $C_{b\to sc\bar{c}}$ used by HFAG for averages.

*HFAG uses BaBar sign convention: $C_f(\text{HFAG}) = C_f(\text{BaBar}) = -A_f(\text{Belle})$.

Experiment	$N(B\overline{B})$	$A^{dir}_{J/\psi K^+}$
	$J/\psi K^+$	
CLEO [39]	9.7M	$+0.018 \pm 0.043 \pm 0.004$
BaBar [40]	124M	$+0.030 \pm 0.014 \pm 0.010$
Belle [41]	31.9M	-0.026 ± 0.022(stat+syst)
Average		$\mathbf{0.015 \pm 0.017}$

Table 1.3: Averaged $A^{dir}_{J/\psi K^+}$ from the direct decays, from PDG 2007.

1.4.2 Direct CP asymmetry in the $B^+ \to J/\psi\pi^+$ decay

In analogy to (1.71), the direct CP asymmetry in the $B^+ \to J/\psi\pi^+$ decay should manifest itself as a charge asymmetry between the event yields:

$$\begin{aligned} A_{CP}(B^+ \to J/\psi(1S)\pi^+) &\equiv A^{dir}_{J/\psi\pi^+} \\ &= \frac{N(B^- \to J/\psi\pi^-) - N(B^+ \to J/\psi\pi^+)}{N(B^- \to J/\psi\pi^-) + N(B^+ \to J/\psi\pi^+)}. \end{aligned} \tag{1.81}$$

The corresponding tree and penguin Standard Model amplitudes are (see Fig. 1.6):

$$T_{b\to d} = T\,\mathbf{V}_{cb}\mathbf{V}^*_{cd} = \mathcal{O}(\lambda^3), \tag{1.82}$$

$$P_{b\to d} = F_u\mathbf{V}_{ub}\mathbf{V}^*_{ud} + F_c\mathbf{V}_{cb}\mathbf{V}^*_{cd} + F_t\mathbf{V}_{tb}\mathbf{V}^*_{td} \tag{1.83}$$

$$= (F_u - F_c)\mathbf{V}_{ub}\mathbf{V}^*_{ud} + (F_t - F_c)\mathbf{V}_{tb}\mathbf{V}^*_{td} \tag{1.84}$$

$$= P^u_{b\to d}\mathbf{V}_{ub}\mathbf{V}^*_{ud} + P^t_{b\to d}\mathbf{V}_{tb}\mathbf{V}^*_{td} \tag{1.85}$$

$$= \mathcal{O}(\lambda^3) \qquad + \mathcal{O}(\lambda^3).$$

So, the transition amplitude contains terms with different weak phases and of the same order of the CKM suppression. Dunietz [42] uses the same approach as Hou, and, with reasonable estimates for the weak and strong phases and the penguin fraction, reports the Standard Model prediction

$$A^{dir}_{J/\psi\pi^+} = \mathcal{O}(0.01). \tag{1.86}$$

Present status

The $b \to dc\bar{c}$ transitions were studied using lifetime analysis of various final states. Results on $C_{b\to dc\bar{c}}$ are available from both BaBar and Belle using final states $J/\psi\pi^0$, D^+D^-, and $D^{*+}D^{*-}$, see [21]. In Table 1.4 we reproduce HFAG inputs and averages. The measurements using the direct decay as listed in PDG 2007 are reproduced in Table 1.5. In general, the results are consistent with the prediction (1.86), but the uncertainties are still large to make any definite conclusion.

Experiment	$N(B\overline{B})$	$C_{b\to dc\bar{c}}{}^{*}$
	D^+D^-	
Belle [43]	535M	$-0.91 \pm 0.23 \pm 0.06$
BaBar [44]	364M	$+0.11 \pm 0.22 \pm 0.07$
Average		$\mathbf{-0.37 \pm 0.17}$
	$J/\psi\pi^0$	
BaBar [45]	232M	$-0.21 \pm 0.26 \pm 0.06$
Belle [46]	535M	$-0.08 \pm 0.16 \pm 0.05$
Average		$\mathbf{-0.12 \pm 0.14}$
	$D^{*+}D^{*-}$	
BaBar [47]	383M	$-0.02 \pm 0.11 \pm 0.02$
Belle [48]	152M	$+0.26 \pm 0.26 \pm 0.05$
Average		$\mathbf{0.02 \pm 0.10}$

Table 1.4: Measurements of $C_{b\to dc\bar{c}}$ used by HFAG for averages.
*HFAG uses BaBar sign convention: $C_f(\text{HFAG}) = C_f(\text{BaBar}) = -A_f(\text{Belle})$.

Our interest in this decay has been triggered by Belle measurement, which reported large direct CP asymmetry in the $B^0 \to D^+D^-$ decay, $C_{D^+D^-} = -0.91 \pm 0.23 \pm 0.06$ [43], in excess of the Standard Model estimate (1.86). However, this result was not confirmed by the subsequent measurement at BaBar, which reported $C_{D^+D^-} = +0.11 \pm 0.22 \pm 0.07$ [44]. Thus, an additional constraint is useful.

1.4.3 Perspectives for Tevatron and Analysis strategy

Both the measurements of $A^{dir}_{J/\psi K^+}$ and $A^{dir}_{J/\psi\pi^+}$ boil down to the measurement of the charge asymmetry (1.50). Both Tevatron accelerator complex (see Section 2.1) and the DØ detector (see Section 2.2) provide an excellent environment for such a measurement:

Experiment	$N(B\overline{B})$	$A^{dir}_{J/\psi\pi^+}$
	$J/\psi\pi^+$	
Belle [41]	31.9M	$-0.023 \pm 0.164 \pm 0.015$
BaBar [49]	89M	$+0.123 \pm 0.085 \pm 0.004$
Average		$\mathbf{0.09 \pm 0.08}$

Table 1.5: Averaged $A^{dir}_{J/\psi\pi^+}$ from the direct decays, from PDG 2007.

.

- Using hadronic collisions, instead of the electron-positron collisions, results in the production rate of $b\overline{b}$ pairs which is $\sigma_{b\overline{b}}(hadronic)/\sigma_{b\overline{b}}(e^+e^-) = (\alpha_S/\alpha_{EM})^2 \sim 100$ times larger; this ensures much faster accumulation of the same number of $B\overline{B}$ events.

- No production asymmetry of B hadrons is expected from the $p\overline{p}$ collisions (pp collisions would produce e.g. more $B^+(\overline{b}u)$ then $B^-(b\overline{u})$, since valence $\overline{u}$ quarks are absent).

- The polarities of DØ magnets (Section 2.2) are regularly reversed during the data-taking. In this way, the same part of the detector is exposed to the flux of particles of both charges. This feature of DØ helps to effectively account for various first-order systematic effects due to different reconstruction efficiencies of positive and negative particles, and allows to construct the detector model to disentangle the higher order systematic effects (Section 3.2).

The measurement of $A^{dir}_{J/\psi K^+}$ is based on approximately 40,000 of $B^+ \to J/\psi K^+$ decays collected at DØ by 2007. This can narrow the statistical uncertainty on $A^{dir}_{J/\psi K^+}$ down to 0.005, which is better than the 2007 PDG world average (see Table 1.3), and approaches the level of the Standard Model prediction. At this level of uncertainty we can establish a 2% asymmetry due to the $b \to sZ'$ coupling at 4σ level.

As the experience of the B factories shows, one of the major issues of concern in the measurements of CP asymmetry (1.50) in the direct decays $B^+ \to J/\psi K^+$ or $B^+ \to J/\psi \pi^+$ is the systematic bias due to different reconstruction efficiency of positive and negative tracks. The reconstruction asymmetry for positive and negative kaons is especially large. Different experiments deal with it differently. CLEO [39] estimates the kaon reconstruction asymmetry from the detector simulation. Belle [41] measures $\epsilon_{\pi^-}/\epsilon_{\pi^+}$ and $\epsilon_{K^-}/\epsilon_{K^+}$ in the data, using the samples of decays $D^\pm \to K^\mp \pi^\pm \pi^\pm$ and $D^0 \to K^- \pi^+ / \overline{D}^0 \to K^+ \pi^-$. BaBar [40] assigns a tracking efficiency error of 1.3% per track. All the estimates are included in the systematic uncertainty of the corresponding measurement.

Contrary to the B factories, hadron collider provides a way to fully account for the kaon asymmetry and perform a statistically-dominated measurement of $A^{dir}_{J/\psi K^+}$. Large number of c-mesons are produced in the $p\overline{p}$ collisions, which allows to have a large sample of semileptonic D^0 decays. CP violation in D^0 decays is suppressed due to the following factors:

- The corresponding box diagrams (see Fig. 1.4(b)) induced by the virtual b-quarks are suppressed by the small combination of CKM matrix elements $V^*_{ub}V_{cb} = \mathcal{O}(\lambda^4)$ (see Fig. 1.4(b)). As light quarks dominate the box diagram, the mixing is suppressed: in 2008 HFAG reported $x_D = \Delta M_D/\Gamma_D = 0.0084 \pm 0.0033$ [21]. Moreover, as the mixing matrix is effectively reduced to nearly 2×2, no sizable CP violation in D^0 mixing is possible. HFAG experimentally confirms the last conclusion, reporting no evidence for the CP violation in the D^0 system at the current precision.

- The semileptonic D^0 decays are pure tree level and governed by a single weak phase. Hence, so no direct CP violation is expected.

- Also, different New Physics theories [50] predict an enhancement of ΔM_D, but keep $\Delta\Gamma_D$ at its Standard Model level. Hence, the relation

$\Delta\Gamma_D/\Delta M_D \ll 1$ holds, which implies $|\,q/p\,|_D = 1$ (see Section 1.2). Thus, CP violation in D^0 mixing is expected to be suppressed even in the presence of the New Physics.

The kaon asymmetry can be measured using a sample of $\sim$ 2.7M of decays $D^* \to D^0(\mu K \nu_\mu)\pi$, collected at DØ by 2007. No CP asymmetry between the semileptonic decay $D^0 \to \mu^+ K^- \nu_\mu$ and its charge conjugate is expected, so all the asymmetry between μ^+K^- and μ^-K^+ may be attributed to the asymmetry of the kaon reconstruction. The statistical uncertainty is expected at the level of $\Delta A = 1/\sqrt{2.8 \cdot 10^6} \sim 0.001$, therefore, it will not contribute significantly to the statistical uncertainty of the $A^{dir}_{J/\psi K^+}$.

As for the yield of the $B^+ \to J/\psi\pi^+$ decays, it is expected to be reduced by the factor $\lambda^2 \sim 0.04$ relative to the $B^+ \to J/\psi K^+$ signal. We therefore expect around 1600 events and the corresponding statistical uncertainty on $A^{dir}_{J/\psi\pi^+}$ of order 0.03. The reconstruction asymmetry for positive and negative pions is tiny, and can be accounted for in the systematic uncertainty of the measurement.

The outline of the remainder of this work is as follows: in Chapter 2 we describe the experimental apparatus – the Tevatron accelerator complex and the DØ detector. In Chapter 3 we detail the procedure of the measurement of direct CP violation asymmetries in $b \to sc\bar{c}$ and $b \to dc\bar{c}$ transitions using the decays $B^+ \to J/\psi K^+$ and $B^+ \to J/\psi\pi^+$ (Section 3.4). The kaon asymmetry A_K, necessary for the former, is measured separately on a sample of $D^0 \to K\mu\nu$ decays (Section 3.3), and converted to the kaon asymmetry measurement in the $J/\psi K$ sample, $A_K(J/\psi K)$.

Chapter 2

Experimental Apparatus and Data Acquisition

2.1 Accelerator complex

The DØ detector is one of the two multi-purpose detectors located at the Tevatron collider at Fermilab, Batavia, Illinois, USA. In the present (2008) state of operation, called Run II, the Tevatron accelerator complex is capable of providing $p\overline{p}$ collisions at $\sqrt{s} = 1.96$ TeV at peak luminosity of $\sim 10^{32}$ $\mathrm{cm}^{-2}\,\mathrm{s}^{-1}$.

2.1.1 Accelerator chain

The simplified drawing of the Tevatron accelerator complex is shown in Fig. 2.1. The acceleration chain starts in a Cockcroft-Walton chamber [51]. Here the hydrogen atoms are ionized to make H^- ions which are then accelerated through the initial stages of the accelerator complex. The Cockroft-Walton machine accelerates the ions to an energy of about 750 keV, before feeding them to a linear accelerator, Linac, where they are accelerated to 400 MeV. Then the electrons are removed from the ions to leave protons, by passing a beam of ions through the carbon foil. The protons then enter a synchrotron accelerator, Booster, and are accelerated to 8 GeV before

entering the Main Injector.

The Main Injector performs the following functions:

- It accepts 8 GeV protons from the Booster, and 8 GeV antiprotons from the antiproton Accumulator (see below);
- It accelerates the protons to 120 GeV and delivers them to the antiproton production target;
- It accelerates protons and antiprotons to 150 GeV and injects them into the Tevatron.

For antiproton production, the 120 GeV protons are sent to hit a nickel target. The negatively charged particles of approximately 8 GeV are selected and sent to the Debouncher (not shown), where their momentum spread is reduced. From the Debouncher the antiprotons are transferred to the Accumulator (not shown), where the antiproton beam emittance is thoroughly reduced through stochastic cooling [52]. The cooled 8 GeV antiprotons are transferred to the Main Injector where they are pre-accelerated to 150 GeV and subsequently injected into the Tevatron.

The Tevatron provides the final acceleration before collisions, from 150 GeV to 980 GeV. Once collision energy is reached, the beams are focused for collisions in two collision points, inside both of the Fermilab detectors, DØ and CDF. The protons and antiprotons circle in bunches, with bunch crossing occurring every 396 ns. The beams continue to circle and collisions are recorded during a period known as a *store*. The interaction of particles with molecules of residual gas in the beam pipe and long range bunch-bunch interactions increase the emittances of the beams with time. The luminosity reduces, and after a certain period the beams are dumped and a new store is started.

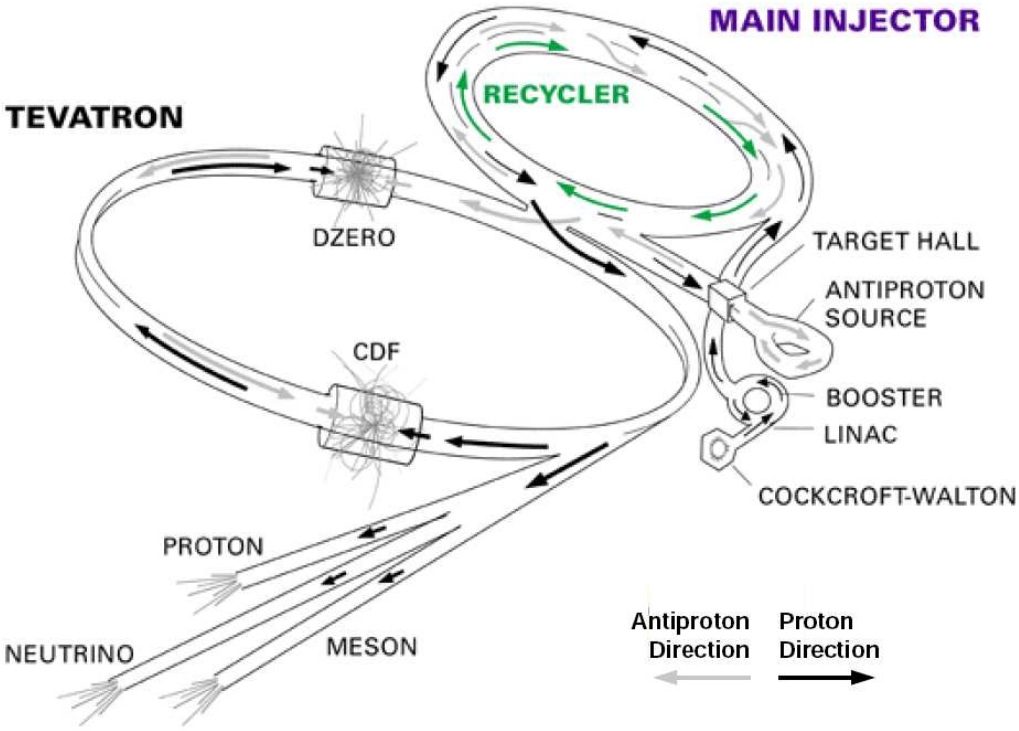

Figure 2.1: Tevatron accelerator complex.

Energy, GeV	980
Proton bunches	36
Antiproton bunches	36
Protons/bunch	2.7×10^{11}
Antirotons/bunch	3.0×10^{10}
Bunch length, m	0.37
Bunch spacing, ns	396
Interactions/crossing	2.3
Peak luminosity, $\mathrm{cm}^{-2}\,\mathrm{s}^{-1}$	$0.86 \times 10^{32}/3.2 \times 10^{32}$
Integrated luminosity, pb^{-1} /week	17.3/30

Table 2.1: Tevatron parameters for Run II(a/b)

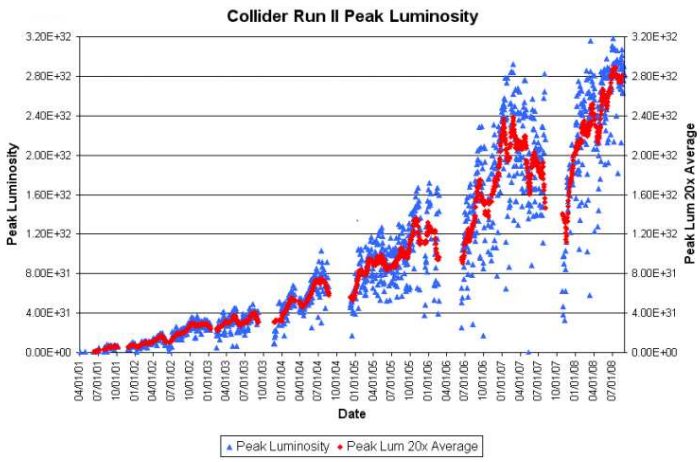

Figure 2.2: Peak luminosities during the Run II of Tevatron.

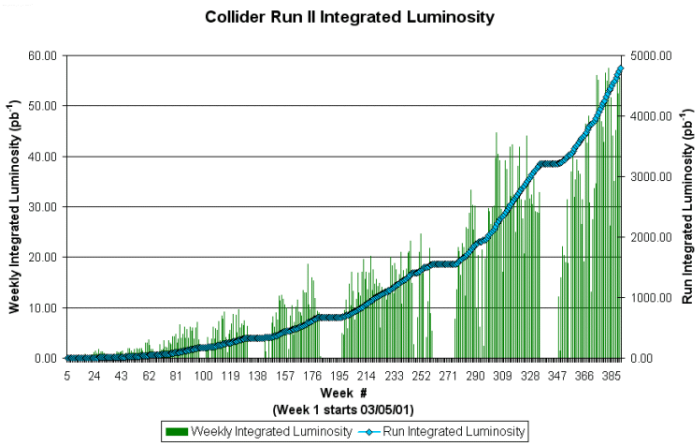

Figure 2.3: Weekly integrated luminosity and its cumulative total during the Run II.

2.1.2 Accelerator performance

Measures are constantly undertaken to increase the Tevatron luminosity by overcoming the limitations of the antiproton beam [53]. The result can be appreciated from the evolution chart of the Tevatron peak luminosity (the luminosity at the beginning of the store) (see Fig. 2.2).

The integrated luminosity delivered by Tevatron in Run II is shown in Fig. 2.3. At the end of Run IIa in March 2006, 1.6 fb^{-1} were delivered, of which 1.3 fb^{-1} were recorded by DØ. After some upgrades during the 2006 shutdown, the Tevatron Run IIb commenced. The main parameters of

the Tevatron in Run IIa and IIb are shown in Table 2.1. The status of the Tevatron accelerator as of 2006 and perspectives for the rest of Run II are summarized in [54].

2.2 DØ detector

DØ Run II detector (see Fig. 2.4) is a general-purpose detector positioned around DØ interaction point. Its layout is standard for detectors of this type. From the inside out there are: tracking system inside a solenoidal magnet, electromagnetic calorimetry, hadron calorimetry, and muon detectors. The feature which distinguishes the DØ detector from other general-purpose detectors is the toroid magnet sandwiched between the muon chambers. The magnetic field created by the toroid magnet allows local measurements of the muon momentum, which in turn improves the matching of central tracks to muon hits. Also, local muon measurements open additional possibilities for detector characterization, allowing to measure different tracking and muon identification efficiencies.

Another important property of DØ detector is the regular (approximately every two weeks) reversal of polarities of both solenoid and toroid magnets. In this way, the same part of the detector is exposed to the flux of particles of both charges. This allows to cancel many charge-dependent systematic effects. Many DØ analyses, including the present one, rely on this polarity reversal. We will give more information in Section 3.2.

The Cartesian coordinate system associated with the DØ detector has the detector's geometric center as its origin. The z-axis points in the direction of the proton beam, the y axis points upwards, and the x axis is in the plane of accelerator ring pointing outwards. The center of the detector roughly coincides with the beam crossing region.

The detector is roughly cylindrical and forward-backward symmetric,

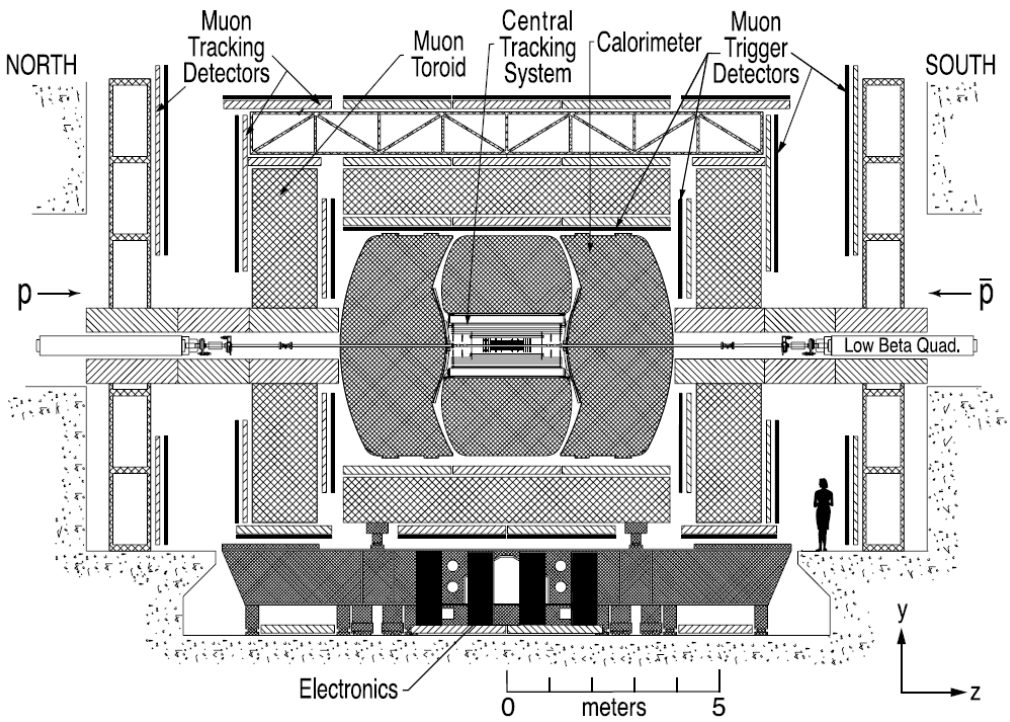

Figure 2.4: General view of DØ Run II detector.

so it is often convenient to work in cylindrical (z, ρ, ϕ) or polar (r, θ, ϕ) coordinates. The z axis is the same as for the Cartesian system. The azimuthal angle ϕ runs in the transverse (x, y) plane with $\phi = 0$ being the positive direction of the x axis. The polar angle θ is counted from the positive direction of the z axis. Often the angle θ is replaced with pseudorapidity

$$\eta = -\log \tan \frac{\theta}{2}. \tag{2.1}$$

The choice of (r, η, ϕ) is appropriate, because it reflects the symmetries of the experiment. Indeed, physical processes are invariant under rotation around the unpolarized beam, making ϕ a natural choice. The pseudorapidity η is the ultra-relativistic limit of the rapidity

$$\zeta \equiv \frac{1}{2} \log \frac{E + p_z}{E - p_z}, \tag{2.2}$$

It can be shown that under a Lorentz boost β along z axis the rapidity transforms as $\zeta' = \zeta + \tanh^{-1} \beta$. Thus, ζ, and, therefore, η intervals are Lorentz-invariant. Lorentz boosts are created by asymmetric interactions of

partons in $p\overline{p}$ collisions. Therefore, it is appropriate (wherever possible) to achieve uniform coverage in ϕ and η to avoid detector artifacts in kinematic distributions. This approach is adopted at DØ.

In the following we give a general description of the DØ detector with an emphasis on the elements relevant to the present analysis – the central tracking and the muon systems. A detailed description of the DØ detector can be found in [55].

2.2.1 Central Tracking System

A charged particle excites, or, in the limit, ionizes, atoms of matter as it passes though it. Typically this excitation is localized near the particle's trajectory in little clusters called *hits*. The purpose of tracking devices is to detect the position of those hits, which are used to reconstruct the particle's trajectory in the process of *tracking*. In High Energy Physics (HEP) experiments we are interested in the momentum of the fundamental participants of the processes (quarks, leptons, etc.), which are correlated with the momentum of the outgoing particles. So the tracking system is normally placed inside a magnetic field to bend the tracks of charged particles and infer the momentum from track curvatures. The motion of a charged particle in the magnetic field is governed by the Lorentz force law:

$$\frac{d\mathbf{p}}{dt} = q\mathbf{v} \times \mathbf{B}. \tag{2.3}$$

Parameterized in terms of the path length s, (2.3) is equivalent to

$$\frac{d^2\mathbf{x}}{ds^2} = \left(\frac{q}{p}\right)\frac{d\mathbf{x}}{ds} \times \mathbf{B} = \left(\frac{\omega_c}{B}\right)\frac{d\mathbf{x}}{ds} \times \mathbf{B}, \tag{2.4}$$

where $\omega_c = qB/p$ is the cyclotron frequency. For a uniform magnetic field equation (2.4) can be integrated exactly, and the solution is a helix characterized by five integration constants, three of which define the radius-vector of the helix's starting point, and two define the unit vector of the direction. For the purposes of tracking, however, the following equivalent set is used at DØ :

ϵ^z – z coordinate of the point of the closest approach to the z axis, dubbed "longitudinal" or "stereo" impact parameter,

ϵ^d – distance from the point of the closest approach to the z axis, dubbed "transverse" or "axial" impact parameter,

ϕ_0 – direction of the transverse momentum of the particle at the point of the closest approach to the z axis,

$\tan\lambda$ – ratio of the helix step to its diameter (helix pitch),

$\rho = q/2R$ – helix signed curvature. The sign reflects that particles of opposite charges bend in opposite directions in the magnetic field.

The parameters of the helix are determined at the track reconstruction (*tracking*) stage. The transverse and longitudinal components of the particle momentum, p_T and p_z, and the momentum proper, p_{tot}, are then calculated as:

$$p_T = \frac{cB}{2|\rho|}, \tag{2.5}$$

$$p_z = p_T \tan\lambda, \tag{2.6}$$

$$p_{tot} = \sqrt{p_T^2 + p_z^2}. \tag{2.7}$$

The energy of a particle can be inferred from the tracking information alone, using a specific mass hypothesis m:

$$E = \sqrt{m^2 + p^2}. \tag{2.8}$$

The transverse impact parameter is a signed quantity:

$$\epsilon^d = q(\sqrt{x_c^2 + y_c^2} - R), \tag{2.9}$$

where q is the particle charge, (x_c, y_c) is the center of the helix as projected onto the xy-plane, and R is helix's radius (see Fig. 2.5).

The central tracking at DØ is provided by the Silicon Microstrip Tracker (SMT) located inside the Central Fiber Tracker (CFT), both within a 1.92 T solenoidal magnet (see Fig. 2.6). The combined SMT and CFT system

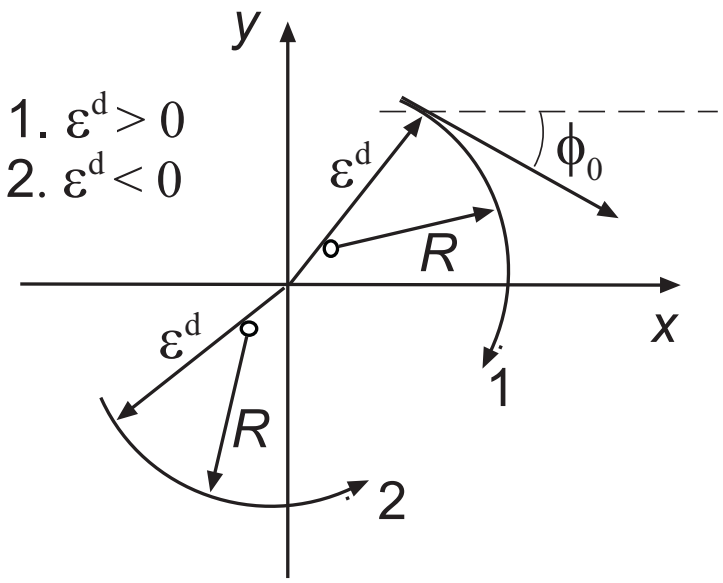

Figure 2.5: Track parameters on a z plane.

provides coverage up to $|\eta| < 3$ and achieves the resolution of the longitudinal projection of the impact parameter around $\sigma(\epsilon^z)$ =35 μm. The resolution of the transverse projection of the impact parameter is around $\sigma(\epsilon^d)$ =15 μm for tracks with $p_T > 10$ GeV/c, which is better then the pitch of the SMT silicon detectors (see next section). For low momentum tracks of $p_T \approx 1$ GeV/c the resolution degrades to $\sigma(\epsilon^d)$ =50 μm.

SMT

For the purposes of B physics measurements (B lifetime, b-tagging) one has to accurately measure tracks close to the interaction point. Also, the detector located there has to sustain the radiation-hard environment. Currently, silicon microstrip detectors are best suited for this kind of task.

The principle of a microstrip detector is illustrated in Fig. 2.7. In a typical *single-sided* detector, finely spaced strips of strongly doped p-type silicon (p) are implanted on a lightly doped n-type silicon (n) substrate. On the opposite side, a thin layer of strongly doped n-type silicon (n^-) is deposited. A positive voltage is applied to the n^- side, which depletes the n volume of free electrons and creates an electric field. When a charged

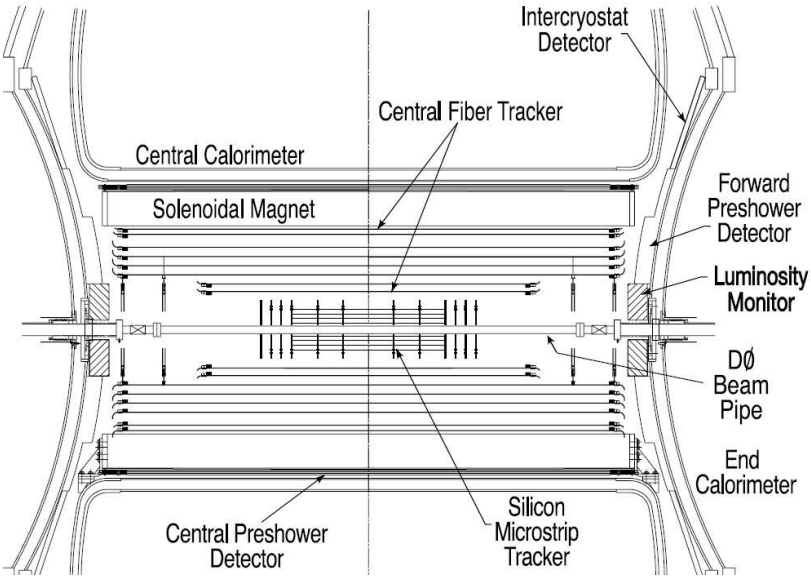

Figure 2.6: Central tracking system of DØ Run II detector, view in (x, z) plane.

particle crosses the substrate it leaves a trail of electron-hole pairs from ionization. In the electric field, holes drift to the p strips producing a well-localized signal. The signal is then detected on a small cluster of strips, and the particle position is extracted by weighting the strip positions by the amount of charge collected. In this way the achieved resolution can be better than the pitch between the strips. The n^- side can also be made in form of read-out strips, making a *double-sided* detector. Moreover, the n^- strips may be tilted relative to the p strips, making a 3D stereo measurement possible.

The general view of the SMT detector is shown in Fig. 2.8. To achieve better resolution of cluster position, the track should enter the substrate perpendicularly. This fact motivated the general SMT design consisting of barrels for low $|\eta|$ interspaced with disks for high $|\eta|$ tracks. The detector has six barrels in the central region, each barrel contains eight silicon read-out layers, or "ladders" (see Fig. 2.9). Ladders are mounted on beryllium bulkheads. "Active" bulkheads contain the cooling channels and the connections to the outer support cylinder. "Passive" bulkheads serve to set the

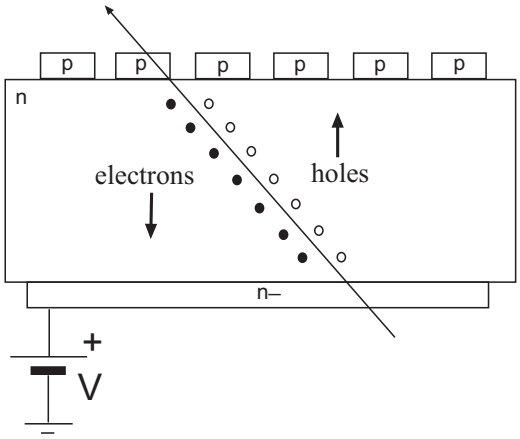

Figure 2.7: Principle of silicon microstrip tracker.

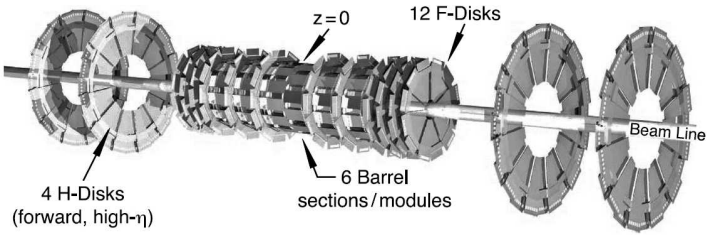

Figure 2.8: The disk-barrel structure of the DØ silicon microstrip tracker.

spacing of the ends of the ladders without read-out chips. Each barrel is capped at high $|z|$ with a disk of twelve double-sided wedge detectors, called "F-disks". Forward of the three disk/barrel assemblies on each side there is a unit consisting of three F-disks. In the far forward region, two single-sided large-diameter disks, "H-disks", provide additional tracking at high η. The outer diameter of a SMT barrel is about 10 cm. The H-disks are located at $|z|$ =100 and 121 cm.

Various types of silicon sensors are used throughout the SMT. Most of the ladders are double-sided sensors, with p-side axial strips oriented parallel to the beam, and n-side strips at a stereo angle. In layers 3, 4, 7 and 8, this angle is 2°. In layers 1, 2, 5, and 6 it is 90° with the exception of the outermost two barrel sections which contain single-sided axial detectors. The H-disk wedges each contain two single-sided detectors mounted back-to-back, with the strips having the relative angle of 15°. The pitch of the

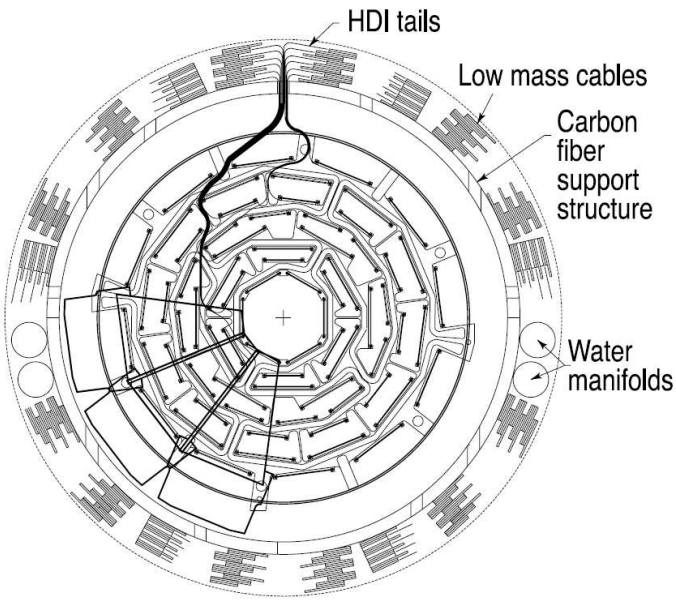

Figure 2.9: Cross-section of SMT barrel module. Ladders mounted on the beryllium bulkhead are shown.

strips varies between the sensor types, as shown in Table 2.2. The sensors are characterized by the signal to noise ratio between 12:1 and 18:1.

The sensors are read out using the custom made SVXIIe chip [56]. A sketch of double-sided 2° ladder with nine SVXIIe read-out chips is shown in Fig. 2.10. The pulse height information is used to calculate the centers of clusters of hit strips, achieving a precision of around 20 μm.

Central Fiber Tracker

The DØ Central Fiber Tracker provides coverage up to $|\eta| < 1.7$. It consists of scintillating fibers mounted on eight concentric support cylinders and occupies the radial space from 20 to 52 cm from the center of the beampipe. The support cylinders are double-walled with a 6.3 mm thick core of Rohacell [57]. The walls are constructed from linear carbon fibers impregnated with about 40% resin. The total thickness of carbon per cylinder is 0.5 mm. To accommodate the forward SMT H-disks, the two innermost cylinders are 1.66 m long; the outer six cylinders are 2.52 m long. Each cylinder contains one doublet layer in which fibers are oriented parallel to the beam, and one

Sensor	Pitch, μm
Barrel axial	50
Barrel stereo 2°	62.5
Barrel stereo 90°	153.5
F-disk (p-side)	50
F-disk (n-side)	62.5
H-disk	80

Table 2.2: Pitches of different silicon detectors comprising DØ Silicon Mictrostrip Tracker.

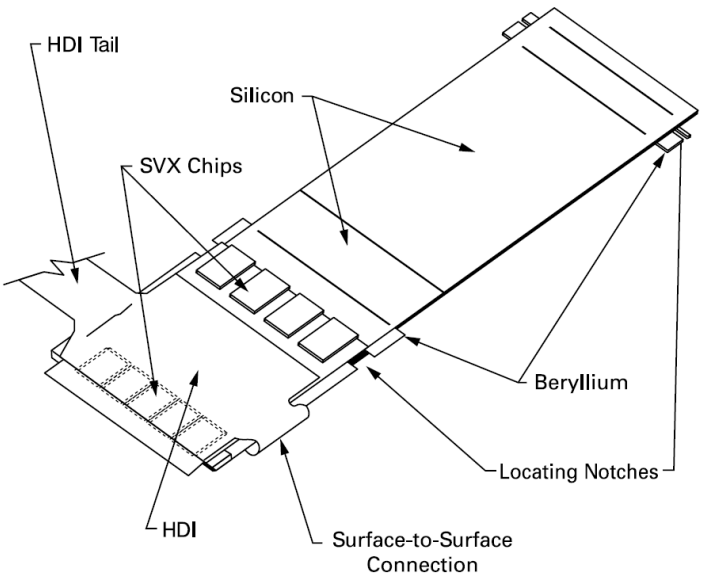

Figure 2.10: The design of double-sided 2° ladder. The SVXIIe read-out chips shown as dashed lines are located on the p-side of the ladder.

doublet layer in which the fibers are at a stereo angle. The stereo angle alternates between $+3°$ and $-3°$ in the adjacent cylinders.

The fibers are constructed from a polystyrene core with two claddings and have an overall diameter of 825 μm. The polystyrene is doped with the fluorescent dye paraterphenil and the wave-shifter dye 3-hydroxyflavon. Excitations in the polystyrene are transferred to the paraterphenyl, which undergoes fluorescent decay emitting light with wavelength of around 340 nm. This wavelength is quickly attenuated in the polystyrene, so the wave-shifter dye is used to absorb it and emit the light with 530 nm, well within the transparency window of polystyrene.

Each fiber is connected by a clear fiber waveguide to a visible light photon counter (VLPC). The VLPCs are silicon avalanche photodiodes operating at 9 K with high gain and high quantum efficiency, capable of detecting single photons. The flex circuits guide the electric signal from VLPC to the preamplifiers on the analog front-end boards (AFE). To facilitate commonality with SMT further downstream, the same chip is used to digitize the CFT and SMT signals − the SVXIIe. However, because the SVXIIe digitization speed is too low to generate trigger decision, a special chip, the SIFT chip, provides a trigger pick-off.

The fiber diameter of 835 μm ensures the inherent doublet layer resolution of about 100 μm, taking into account that the position of individual fibers is known to better than 50 μm.

Solenoidal magnet

The superconducting solenoidal magnet surrounds the tracking system (see Fig. 2.6). The solenoid was designed to optimize the momentum resolution, $\delta p_T/p_T$, within the space inside the Run I calorimeter, which is still in use in the current detector. The solenoid is 2.73 m long and 1.42 m in diameter, and achieves 2 T by operating at the current of 1500 A. Uniform field distribution is important for tracking, so that the track trajectories were closer

to the ideal helix, see Section 2.2.1. The magnetic field inside the solenoid is homogeneous to within 0.5%, which is achieved by using larger winding density at both ends of the coil.

The regular reversal of the solenoid polarity allows to cancel many charge-dependent systematic effects due to the tracking system. Solenoid polarity is reversed using a 5000 A DC mechanical motorized polarity reversing switch and a switch controller. The controller confirms that the polarity reversal occurs at zero current load and that the power supply is turned off.

2.2.2 Muon system

Muons directly couple to the intermediate vector bosons W and Z. As they are clearly identifiable they may serve as an indicator of the processes involving $W \to \mu\overline{\nu}_\mu$ or $Z \to \mu^+\mu^-$, allowing to trigger on such events. In the same way muons are the characteristic signature of the weak decays of heavy quarks, such as $b \to cW$ and $c \to sW$ (here W is virtual). Triggers requiring two muons allow to collect a large sample of $J/\psi \to \mu^+\mu^-$ decays which constitutes the basis for a large portion of DØ B physics program, and is also extensively used for detector understanding/calibration.

DØ detector uses the system of muon drift chambers and scintillators. The drift tubes provide precise spatial measurement, while the scintillators produce fast signal to allow triggering. Individual muon candidates are detected in the muon chambers from the track segments they leave. If the local muon track matches a certain track measured by the central tracking system, the two are combined into a "global" muon. As already mentioned, the muon chambers are interspaced with the toroid magnet. The muon tracks bend in the magnetic field created by the toroid, which allows the local measurement of muon transverse momentum. This information is used for low p_T cut in L1 trigger, and for better matching with central tracks.

The remainder of this section is devoted to a more detailed description of the muon systems.

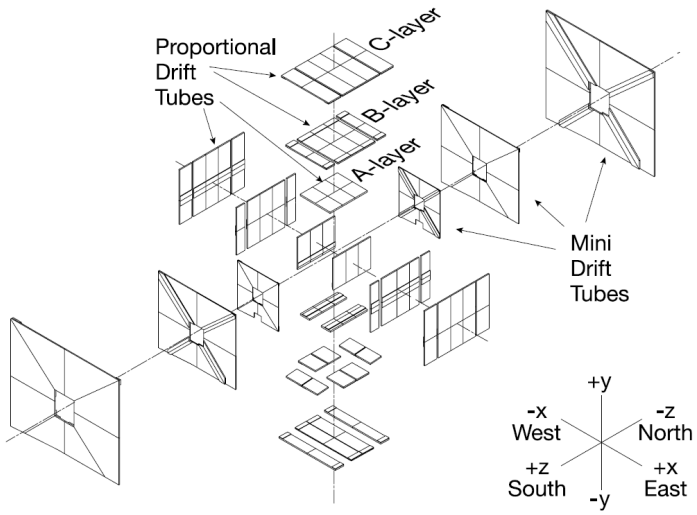

Figure 2.11: Exploded view of the muon wire chambers.

Toroidal magnet

The toroidal magnet can be seen in Fig. 2.4. Its central part is a square annulus 109 cm thick, with its inner surface about 318 cm away from the beamline. It covers $|\eta| < 1$. End toroids are located at $454 < |z| < 610$ cm. The toroid coils operate at 1500 A to achieve a magnetic field of about 1.8 T. The regular reversal of the toroid polarity allows to cancel many charge-dependent systematic effects due to the muon chambers.

Central muon system

The exploded view of the muon chamber is shown in Fig. 2.11. The central muon system consists of three layers of proportional drift tubes (PDT), which extend up to $|\eta| < 1$ (see Fig. 2.4).

The inner "A" layer is inside the central toroid, the "B" and "C" layers are outside. The PDTs are made from rectangular drift tubes approximately 10 cm across and 6 m long, filled with a gas mixture consisting of 84% argon, 8% methane, and 8% CF_4. The anode wire runs through the center of each cell, with cathode pads located above and below it. The wires are ganged together in pairs and read out by electronics located at one end of each PDT.

PDTs allow to measure the drift time of electrons to the anode wire, which gives the position of the hit in (x, y) with resolution of 1 mm. The drift time to cathode pad measures the position along z with resolution 5 mm. The "A" layer pads are fully instrumented with electronics; only about 10% of the "B" and "C" layer pads are instrumented. The reason for this was that, first, for tracks traversing all three layers, the pad coordinate does not improve the pattern recognition or resolution significantly, and second, fully instrumenting the "B" and "C" layer pads was too expensive. If the pad is not instrumented, the z position is inferred from the difference in the arrival time of the signal pulse at the end of the hit cell's wire and at the end of its read-out partner's wire, giving resolution of 10-50 cm.

The "$A\phi$" scintillator counters cover the A-layer PDTs, those between the calorimeter and the toroid. They provide a fast read-out for triggering on muons and for rejecting out-of-time backscatter from the forward direction. The scintillator hits are matched with tracks in the Level 1 trigger for high p_T single muon and dimuon triggers. $A\phi$ scintillator counters are uniformly segmented in ϕ and provide timing resolution of 2 ns.

Forward muon system

The forward muon system covers $1.0 \lesssim |\eta| \lesssim 2.0$, and consists of mini drift tubes (MDT) and scintillator counters. The MDTs are similar to PDTs, but have a cross-section of only 9.4 mm $\times$ 9.4 mm. The MDTs are arranged similar to PDTs in the central region, with A layer inside the toroid and B and C layers outside. The intrinsic resolution of the chamber is 350 μm, however, the hit resolution degrades to 0.7 mm due to the digitizing electronics, which measures the signal arrival time with an uncertainty of 18.8 ns.

The muon scintillators are located inside (layer A) and outside (layers B and C) of the toroidal magnet, uniformly segmented in ϕ and η. The scintillators achieve timing measurements with a resolution of better than 1

ns.

2.2.3 Other systems

Calorimeter and Preshower

The DØ uranium/liquid-argon calorimeter provides energy measurements for electrons, photons, and jets in the absence of a central magnetic field (as was the case during Run I of the Tevatron). Also, it assists in the identification of electrons, photons, jets, and muons and measures the transverse energy balance in events. The Preshower detectors, Central and Forward, are scintillator strips located right in front of the calorimeter (see Fig. 2.6). They aid both in calorimetry and tracking, enhancing spatial matching between tracks and calorimeter showers. More information can be found in [55].

Luminosity monitor

Luminosity monitor (LM) consists of two arrays of plastic scintillator counters with PMT read-out located at $z = \pm 140$ cm. The location of the arrays can be seen in Fig. 2.6. The counters cover the pseudorapidity range $2.7 < |\eta| < 4.4$.

The luminosity $\mathcal{L}$ is determined from the average number of inelastic collisions per beam crossing $\bar{N}_{LM}$ measured by LM:

$$\mathcal{L} = \frac{f\bar{N}_{LM}}{\sigma_{LM}}, \tag{2.10}$$

where f is the Tevatron beam crossing frequency and σ_{LM} is the effective cross-section of the luminosity monitor, which takes into account its acceptance and efficiency. The number of collisions per crossing is Poisson distributed. So, $\bar{N}_{LM}$ is determined from the Poisson statistics taking into account the beam crossings with no collisions.

The fundamental unit of luminosity measurement is the *luminosity block*. Each luminosity block lasts no more than 60 sec. This time lapse is short

enough so that the instantaneous luminosity is effectively constant, and no uncertainty is introduced in the measurement of the luminosity due to the time slice width. Each luminosity block corresponds to a separate raw data file.

2.2.4 Trigger system

In the Tevatron proton and antiproton bunches cross every 396 ns. Taking into account the total $p\overline{p}$ cross-section, $\sim$ 100 mb, this corresponds to the order of 10^6 $p\overline{p}$ interactions per second. However, most processes of interest have a cross-section of $10-100$ μb or smaller, so the rate of interesting events is correspondingly lower. So it makes sense to filter out interesting events on the fly, according to some pre-selection criteria, and store them on tape for the detailed offline analysis. Thus, the three level trigger design is adopted at general purpose particle detectors, with additional buffering between the triggers (see Fig. 2.12). At the first stage (Level 1 or L1), interesting event signatures are looked for in different subdetectors independently. Most of the $p\overline{p}$ collisions are rejected at this stage, and the output rate is reduced to 2 kHz. Level 2 or L2 receives the L1 information and does a more careful analysis of the event taking longer time; this reduces the accept rate further down to 1 kHz. The joint functioning of L1 and L2 triggers is shown in Fig. 2.13. Only if the event is accepted in L2, the whole detector is read out and the event is built by the Level 3 Data Acquisition System (L3DAQ) and sent to the L3 farm for the limited event reconstruction. There the event rate is reduced further to 50 Hz suitable for storing on tape. L3 decisions are based on complete physics objects as well as on the relationships between such objects (such as the rapidity or azimuthal angle separating physics objects or their invariant mass).

The overall coordination and control of DØ triggering is handled by the COOR package running on the online host. COOR interacts directly with the trigger framework (for L1 and L2 triggers) and with the L3DAQ

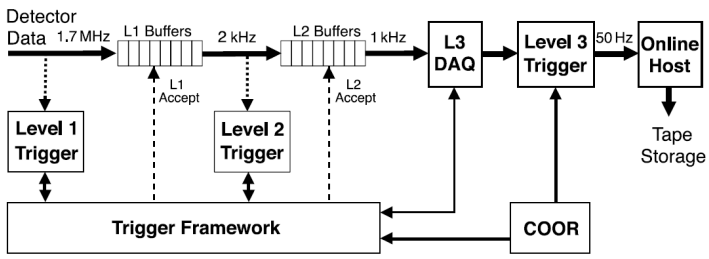

Figure 2.12: Overview of DØ trigger and Data Acquisition System.

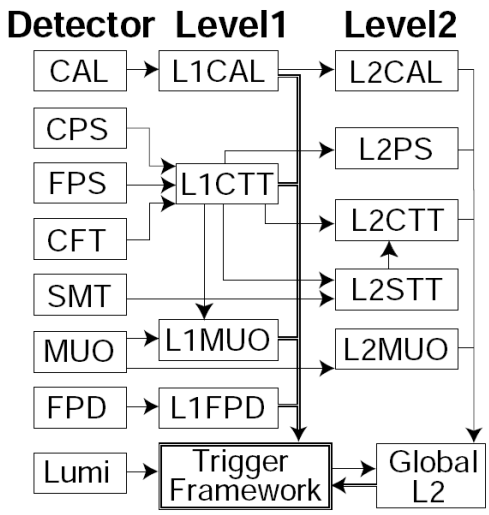

Figure 2.13: Block diagram of L1 and L2 trigger systems.

supervising systems (for the L3 triggers). In the remainder of this section we will give a short description of DØ trigger system with an emphasis on the elements important for the present analysis.

L1 trigger

L1 is implemented in the specialized hardware. The calorimeter trigger (L1Cal) looks for energy deposition patterns exceeding programmed limits on transverse energy deposits; the central track trigger (L1CTT) and the muon system trigger (L1Muon) compare tracks, separately and together, to see if they exceed preset thresholds in transverse momentum. The track reconstruction starts in the L1 central track trigger, which looks for track patterns in CFT, matched to the hits in the Central Preshower Detector.

L2 trigger

In L2, tracking continues in L2 SMT Track Trigger (L2STT). The L2STT performs online pattern recognition in the data from the SMT. It reconstructs charged particle tracks found in the CFT at L1 with increased precision by utilizing the much finer spatial resolution of the SMT. L2STT is able to measure the impact parameter of tracks precisely enough to tag the decays of long-lived particles, specifically B hadrons.

L3 trigger

L3 trigger is a fully programmable software trigger which performs all basic elements of detailed offline reconstruction in a limited scope. It unpacks raw data, locates hits, forms clusters, applies calibration, and reconstructs tracks, electrons, muons, taus, jets, vertices, and missing E_T. Online monitoring keeps track of current beam spot information (the mean position and spread in (x, y) along with tilts in (x, z) and (y, z)). Using this information, L3 can calculate a fully 3-dimensional primary vertex for each event. By recalculating L3 track parameters using the 3-d vertex, L3 is capable of triggering on the impact parameter of tracks. With input provided by the tracking, jet and vertex tool, b-tagging is implemented in L3.

Trigger bits

Each trigger level maintains a collection of bits which classify standard signatures of interest, e.g. a muon with a p_T exceeding a threshold. The Trigger Framework (Fig. 2.12-2.13) receives signals from various parts of the detector and fires corresponding L1 bits. Upon L1 accept, the mask of L1 trigger bits is sent to L2. Depending on run configuration, L2 invokes a filter script for every L1 bit. The filter script fires a corresponding L2 trigger bit if all its conditions are satisfied. Upon L2 accept, the detector is fully read out, and L3 runs scripts corresponding to L2 trigger bits. Most of the triggers fire more often than the "accept" may be issued, so the trigger rates are

artificially scaled down ("prescaled") by a factor. The prescale factors are chosen depending on the physics program of the experiment.

2.3 Event reconstruction

2.3.1 DØRECO

The DØ Offline Reconstruction Program (DØRECO) [58] reconstructs objects used in the DØ physics analysis. It processes either collider events recorded during online data taking or simulated events produced with the DØ Monte Carlo (MC) program. The executable runs on the offline production farms and the results are placed into the central data storage system for further analysis. DØRECO is designed to produce two output formats. The Data Summary Tape (DST) contains the reconstructed physics objects together with intermediate information available at the level of subdetectors, and is designed to be 150 kB per event. The Thumbnail (TMB) contains a summary of the DST, and is designed to be 15 kB per event. In most cases, the TMB format is used for the physics analyses.

DØRECO is structured to reconstruct events in several hierarchical steps (see Fig. 2.14). Step 1 involves detector-specific processing. Detector unpackers process the raw detector information by unpacking individual detector data blocks. They decode the raw information, associate electronics channels with physical detector elements and apply detector specific calibration constants. For many detectors, this information is used at step 2 to reconstruct clusters (for example, from the calorimeter and preshower detectors) or hits (from the tracking detectors and muon chambers). These objects use geometry constants obtained during alignment to associate detector elements with physical positions in space. The step 3 in DØRECO focuses on the output of the tracking detectors. Hits in the silicon (SMT) and fiber tracker (CFT) detectors are used to reconstruct global tracks. This is one of the most CPU-intensive activities of DØRECO , and involves

running several algorithms. The results are stored in corresponding track chunks, which are used as input to the step 4 of DØRECO , vertexing. First, primary vertex candidates are searched for. These vertices indicate the locations of $p\overline{p}$ interaction and are used in the calculation of various kinematical quantities (e.g. transverse energy). Next, displaced secondary vertex candidates are identified. Such vertices are associated with the decays of long-lived particles. The results of the above algorithms are stored in vertex chunks, and are then available for the final step 5 of DØRECO − particle identification. This step produces the objects most associated with physics analyses and is essential for successful physics results. Using a wide variety of sophisticated algorithms, information from each of the preceding reconstruction steps is combined and standard physics object candidates are created. DØRECO first finds electron, photon, muon, neutrino (missing E_T) and jet candidates, which are based on detector, track and vertex objects. Next, using all previous results, candidates for heavy-quark and tau decays are identified. The DØRECO code is organized in a complex system of packages with many overlapping functions.

The B physics analyses, including the present one, rely mostly on tracking and the muon identification. Therefore, the reconstruction of tracks in the central tracking system, and the reconstruction of the muon clusters with subsequent matching to the central tracks, will be our main concern in the following sections. Vertexing and identification of physics objects for the purposes of B physics analyses is performed by a specially developed DØRECO package, BANA (see Fig. 2.14). BANA relies on the collection of tracks and global muon candidates available after stage 3. It is optimized for B physics studies. More information on BANA package is given in Section 3.1.2.

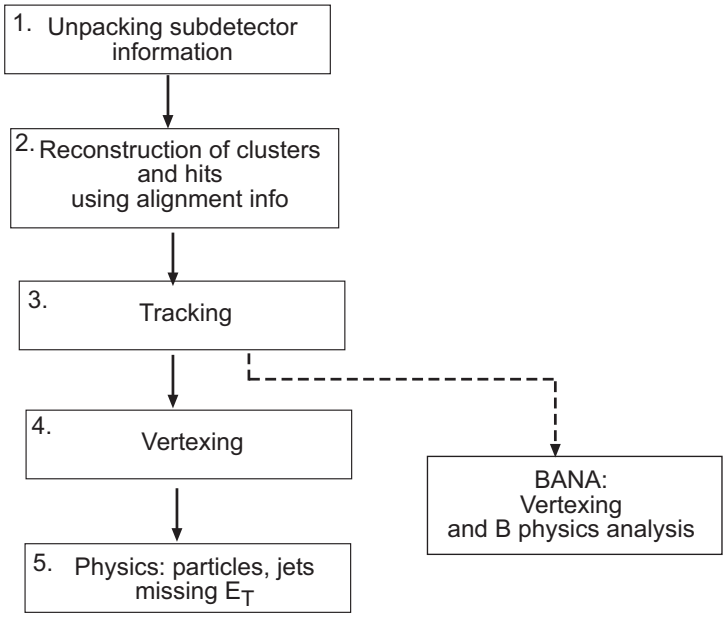

Figure 2.14: Steps of DØ Offline Reconstruction Program and BANA package. See text for details.

2.3.2 Tracking at DØ

The current DØ tracking procedure has been developed as a result of continuous tests of different algorithms on different data and MC samples in search for the optimal combination. It was acknowledged by a special committee [59] to be the best in terms of event reconstruction time, tracking efficiency, rates of fake tracks, and b-tagging efficiency, and remains a default since p14 release [60] of DØRECO package. The tracking procedure uses three algorithms (see Fig. 2.15): the Histogram Track Finding (HTF), the Alternative Algorithm (AA), and the Global Track Finder (GTR). HTF uses a combination of Hough transform and Kalman filter technique, where Hough transform helps to reduce combinatorics from axial-stereo hit association at the early stage, then followed by a more time-consuming Kalman filtering. The AA algorithm uses the Kalman filter technique with simplified track propagator to facilitate track finding, and leaves accurate propagation and determination of track parameters to the later stage. Both algorithms complement each other, since AA has higher efficiency for low p_T and high impact parameter tracks, whereas HTF has better performance for high p_T

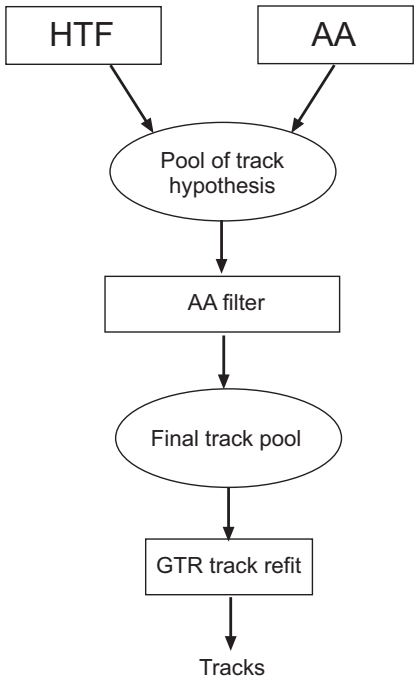

Figure 2.15: DØ tracking procedure as of 2008.

tracks. The algorithms fill the common pool of track hypothesis, to which the filter phase of AA is applied. The filtered tracks are supplied as a collection of hits to the final GTR track refit stage for more accurate Kalman fitting, taking into account multiple scattering and energy loss in the detector material. The output tracks are then used to construct physics objects: primary and secondary vertices, jets, etc. Also, they are matched to muon and calorimeter clusters to obtain global track fits for muons and electrons. In what follows we will give some details about the DØ detector model adopted for the purposes of tracking, and briefly describe the AA and HTF algorithms.

DØ Detector surfaces

The hits left by the particle in the tracking system lie on a 3D helix. However, for the purposes of tracking it is not feasible to consider a 3D picture – it will result in large combinatorics due to ambiguous association between axial and stereo hits and hence will vastly increase the reconstruction time.

Surface	Cylinder	x-y plane	z plane
Constant parameters	radius, r	u, ϕ (see Fig. 2.16)	z_0
Position parameters	ϕ, z_0	v, z_0	x_0, y_0
Direction parameters	α, $\tan\lambda$	dv/du, dz/du	dx/dz, dy/dz
Curvature	q/p_T*	q/p	q/p

Table 2.3: Helix parameters at different surfaces.
*q/p_T is used instead of q/p for historical reasons.

Instead, considering the hits separately in 2D axial and stereo projections of the detector reduces this effect substantially.

Moreover, the Kalman filtering technique is used at several stages of the track reconstruction. It involves propagation of the current best track hypothesis through the detector material, for which the errors of local measurements in the subdetectors need to be propagated to the track parameter errors. This transformation is more easily performed if the track parameters are measured in local coordinate systems of subdetectors, defined on the abstract *surfaces*. The system of surfaces at DØ corresponds to the internal structure of the detector. The SMT barrels are represented by the *xy-planes*, whereas the SMT disks – by *z-planes*, and the CFT layers – by *cylinders* of constant r (see Fig. 2.16). The error on the cluster position in the tracking system is considerably larger along z than in the transverse plane (see Section 2.2.1), which is naturally reflected in the definition of the local coordinate systems.

The parameters of helix track are defined *separately at each surface in local coordinate system of that surface*. Although different for each type of surface, these parameters are: two position parameters, two direction parameters, and the curvature, q/p or q/p_T (see Table 2.3). More details can be found in [61].

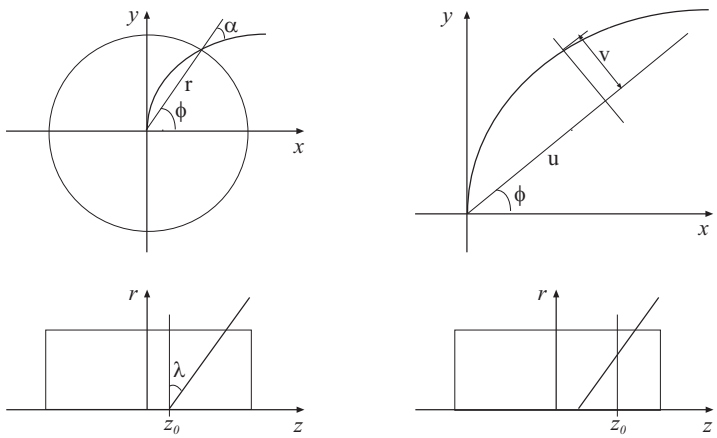

(a) Cylinders represent the CFT layers

(b) xy-planes represent the SMT barrels

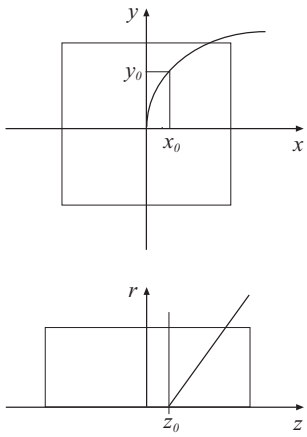

(c) z-planes represent the SMT disks

Figure 2.16: DØ detector surfaces defined for the purposes of track propagation in the Kalman filter.

Track finding by AA

AA algorithm (Alternative Algorithm) [62] implements the Kalman filtering technique. The Kalman filter is an optimal data processing algorithm to extract parameters of an evolving system. It can incorporate the knowledge of the system and measurement device dynamics and the statistical description of system noises to obtain the best current estimate of parameters of interest. The Kalman filter technique was for the first time proposed in radar applications. General information about it can be found in [63], and a sim-

ple but illuminating example is considered in [64]. Technically, the Kalman filter is a set of equations which allows to update the current estimators of track parameters after the new measurement on the next surface arrives.

At the first step of AA running, all possible track hypotheses are constructed from the seeds built from different combinations of 3 hits in different SMT super-layers. Then, each track hypothesis is propagated to the next detector surface, and the hits within $\pm 3\sigma$ expectation window of the predicted measurement are considered (see Fig. 2.17). Every hit, for which the χ^2 of the track fit does not increase too much, $\chi^2(N_{hits}+1) - \chi^2(N_{hits}) < \Delta_{max}$, starts a new track hypothesis. One hypothesis can have several stereo projections to account for all possible combinations of stereo hits associated with a given axial hit. This ambiguity is resolved at the later stages. In this way the pool of track hypothesis is created.

It is also possible that the Kalman filter does not find a cluster on a particular surface because of detector gaps or inefficiencies. If the corresponding subdetector is operational and the expectation window is completely within the sensitive boundaries of the subdetector, a *missing hit* (a *miss*) is added to the list of missing hits.

At the last stage the filtering is applied to the pool of track hypotheses: hypotheses are sorted according to the number of hits, misses, and the overall fit χ^2; best hypotheses are placed first. The hypotheses are considered one by one and accepted as tracks ("AATracks") if they do not share too many hits with other hypotheses. Refer to [62] for the details of the "shared hits policy".

Track finding by HTF

HTF algorithm implements the Hough transform technique. The Hough transform [65] was first proposed for the pattern recognition in the bubble chamber photographs. Applied to tracking, the idea is as follows: every measurement (hit) corresponds to a line in a multi-dimensional space of track

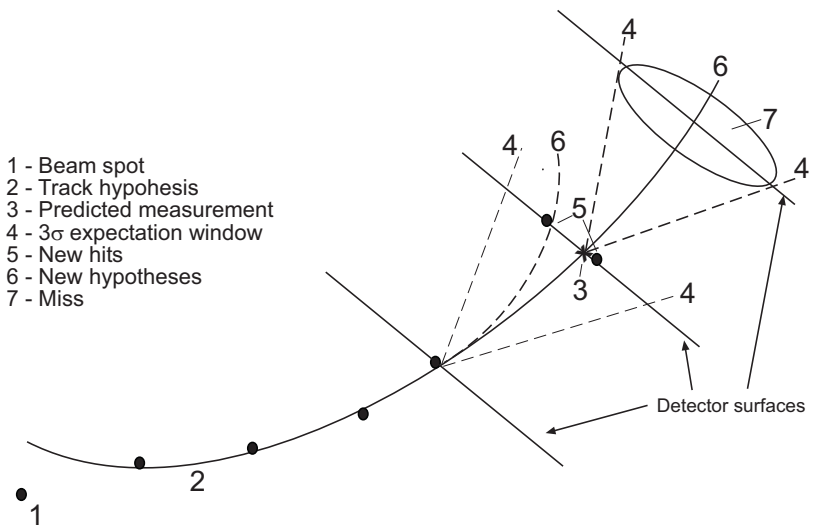

Figure 2.17: Track propagation (Kalman filtering) in AA.

parameters, or to a band, if errors are taken into account. Then, if the hits really belong to the same track, all bands intersect in the same area in the parameter space (see Fig. 2.18). The parameter space is divided into cells. Cell's dimensions reflect the parameter errors obtained by propagation of the position measurement errors into the parameter space. As more hits are added, the number of entries in the cells corresponding to real tracks increases. Then, the peaks in the parameter space constitute track hypothesis which are further purified by the Kalman filter.

A particle in a homogenous magnetic field in the absence of material moves along the helix, which projects into a circle in the transverse (x,y) plane. This circle is characterized by the curvature ρ, impact parameter ϵ^d, and the direction of the track at the point of the closest approach ϕ_0 (Section 2.2.1). A track with a negligible impact parameter, $\epsilon^d \approx 0$, is represented by a point in the 2D parameter space (ρ, ϕ_0). To decrease the combinatorics from the association between axial and stereo hits, the Hough transform from the coordinate space (r, z) has to be performed. The track with $\epsilon^d \approx 0$ looks in (r, z) as a straight line with parameters $(z_0, \tan\lambda)$, where z_0 is the position of the track origin along z axis, and $\tan\lambda$ is the track inclination in (r, z) (see Fig. 2.16).

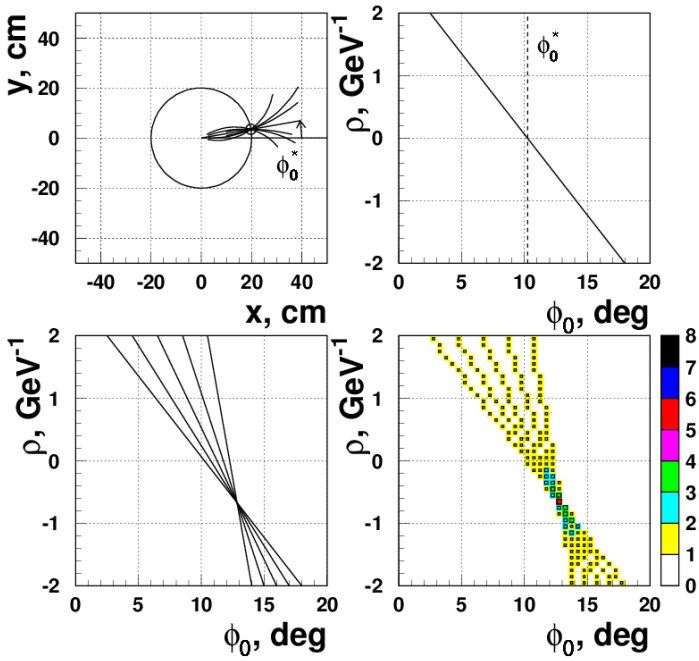

Figure 2.18: Hough transform in HTF.

So, HTF works in the following steps [66]:

- *Hough transform* $(x, y) \rightarrow (\rho, \phi_0)$.
- *2D Kalman filtering in* (ρ, ϕ_0). Peaks in parameter space serve as candidate tracks for the next stage of Kalman filtering at which multiple scattering and energy loss are taken into account.
- *Hough transform* $(r, z) \rightarrow (z_0, \tan\lambda)$.
- *2D Kalman filtering in* $(z_0, \tan\lambda)$.
- *Final 3D Kalman filtering.* At this stage 3D SMT tracks are built and extrapolated into CFT. Alternatively, the tracking may start in CFT and propagate back to SMT.

The parameters of the Kalman filter used in HTF is similar to that of AA. The filter can handle misses, the pool of track hypothesis is filtered on the basis of χ^2 of track's fit, number of hits and number of misses on a track. A simple interacting propagator is used to propagate tracks between surfaces.

GTR track refit

GTR track refit (see Fig. 2.15) accounts for energy loss and the multiple scattering in the tracking system. The details can be found in [67]. The full Bethe-Bloch formula is not implemented, instead, the energy loss δE on a distance x is modelled by a simple constant term and a small relativistic rise with energy:

$$\delta E = (1.66 + 0.0138 \times E)\rho x, \tag{2.11}$$

where ρ is the density of the material. The quantities characterizing multiple scattering are illustrated in Fig. 2.19. A Gaussian fit to the central 98% of scattering angle θ has a width given by [13]

$$\delta\theta = \frac{13.6\,\mathrm{MeV}}{\beta p} z \sqrt{\frac{x}{X_0}} \left[1 + 0.038 \log \frac{x}{X_0}\right], \tag{2.12}$$

where p, β and z are the momentum (in MeV), velocity (as a fraction of the speed of light) and charge (in units of e) of the incident particle, x is the thickness of the material (in cm), and X_0 is the radiation length of the material. In the case of several layers of different materials the combined x and X_0 is calculated before (2.12) is applied.

The parameter δy describes the mean effect of scattering on the position of a particle. It is related to $\delta\theta$ by

$$\delta y = \frac{1}{\sqrt{3}}\, x\, \delta\theta. \tag{2.13}$$

For a thin layer x is small and δy is negligible − this assumption is used in the tracking system.

The uncertainties (2.12) and (2.13) are converted to errors on five track parameters used to describe tracks at different surfaces [67]. These mean values are then added to the relevant terms of the error matrix of the track parameters. The values of p and β corresponding to the average of incoming (E) and outgoing ($E - \delta E$) energy are used to calculate multiple scattering by (2.12) and (2.13).

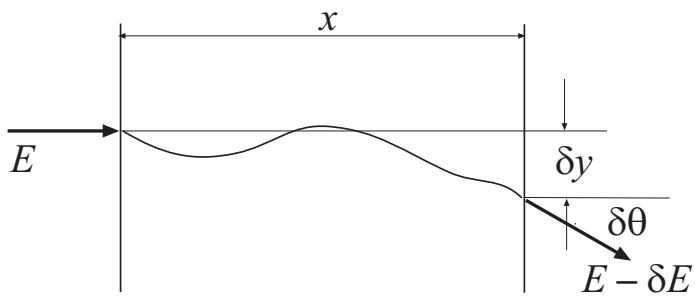

Figure 2.19: Parameters describing multiple scattering.

Vertexing

Vertexing is performed after track reconstruction. Because measurement errors along z and in the transverse plane are different, the 3D impact parameter is not used. Instead, its transverse ("axial") and longitudinal ("stereo") projections are considered. Let ϵ^d and ϵ^z be respectively axial and stereo projection of the impact parameter of a track with respect to the primary (secondary) vertex V. To find the 3D coordinates of primary (secondary) vertex, V_x, V_y, V_z, a procedure developed at LEP is used [68]. The primary vertex is found by minimizing the function

$$\chi^2(N_{trk}) = \sum_{a=1}^{N_{trk}} \frac{(\epsilon_a^d)^2}{(\sigma_a^d)^2} + \sum_{a=1}^{N_{trk}} \frac{(\epsilon_a^z)^2}{(\sigma_a^z)^2} + \sum_{i=x,y,z} \frac{(b_i - V_i)^2}{(\sigma_b^z)^2}. \tag{2.14}$$

The first and second sums are taken over all tracks in the event. The quantity σ_a^d is an error on the axial impact parameter, obtained by the error propagation of the (5×5) covariance matrix of the track parameters to the point of closest approach of a track to the vertex. The quantity σ_a^z is an error on the stereo impact parameter. Due to different errors in the transverse and longitudinal directions, their contribution is decoupled in (2.14): even if the track is not measured along z, the transverse information is still used. The last sum corresponds to a constraint from the position of the interaction point (the beamspot), where b_i and σ_i^b are the beamspot position and size, respectively.

The position of a beamspot in xy-plane is parameterized as a function

of z, since the beams have a small tilt angle with respect to the nominal z axis, and primary interactions occur over the large range of z. The parameterization is obtained by measuring the positions of 1000 primary vertices in each run and performing a fit to the distribution. The typical width of this distribution in a usual run is about 40 μm along x and y. Results are stored in the databases and can be sent automatically to the main accelerator control room for improvement of the beam alignment. The uncertainty in the beamspot position affects the quality of the offline primary vertex reconstruction using (2.14), and therefore influences the b tagging efficiency.

Most of the tracks in the event come from the primary vertex (PV). So, for PV searches, the "tear down" approach is adopted: initially all tracks are used in (2.14), and then excluded one by one until $\chi^2(N_{trk}) - \chi^2(N_{trk} - 1) < \Delta_{max}$, where Δ_{max} is a pre-set algorithm parameter. Multiple interaction may result in several PVs in the event, these are found among the tracks excluded during the previous PV search. In this way the list of PV positions is obtained. The secondary vertices (SV) may include two tracks only ("V-seed"), so opposite "tear up" approach is used: tracks are added to the good V-seeds until $\chi^2(N_{trk} + 1) - \chi^2(N_{trk}) > \Delta_{min}$. In this way the list of SVs is formed.

Two following quality parameters of the vertex fit are often used for event selection:

- χ^2_{res}/ndf of the vertex, where χ^2_{res} is a residual χ^2 after minimizing (2.14), and ndf= $2N_{trk} - 3$;

- The combined significance of a track with respect to the found primary vertex:

$$S = \sqrt{[\epsilon^d/\sigma^d]^2 + [\epsilon^z/\sigma^z]^2}, \tag{2.15}$$

  where ϵ^d, ϵ^z, σ^d, σ^z have been defined in the beginning of this section.

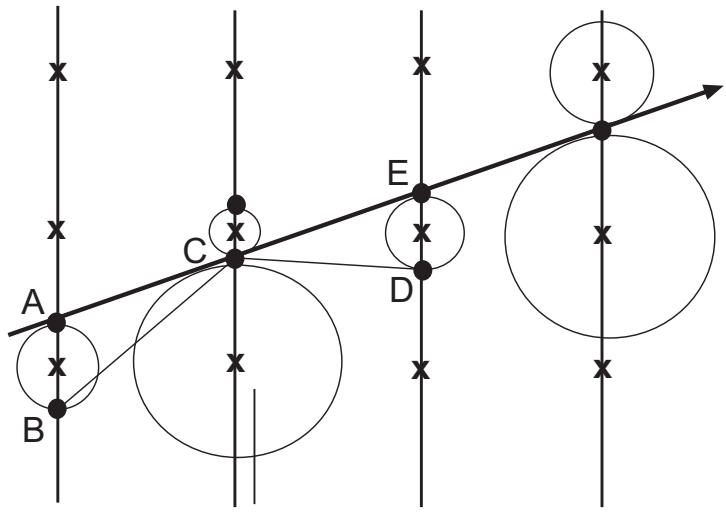

Figure 2.20: Muon local segments from drift circles.

2.3.3 Muon identification

Muons are important objects for B physics, which allow to perform tagging and to measure semileptonic B decays and B decays involving J/ψ. So, muons need to be identified among the central tracks. For this the hits in the muon drift tubes and the muons scintillator are used to form local muon candidates. Then their local trajectories are extrapolated through the detector to match with tracks from the tracking system and form global muon candidates.

The local trajectories are found by the linked list algorithm [69] from the timing information measured by the PDTs and MDTs (Section 2.2.2). The electron drift distance is calculated for each wire registering a hit, and the drift circles are plotted around the wires (see Fig. 2.20). A hit candidate is assigned at each point where a drift circle intersects with a wire plane, hence two hit candidates are associated with each wire hit. The algorithm then connects the pairs of hits with straight link segments, and tries to unite those segments which are compatible with a straight line. A set of algorithms are then used to associate A layer segments (inside the toroid) with those in either or both of B and C layers (outside the toroid). These algorithms take into account the energy loss as a function of the momentum, and the multiple

Number of layers ($nseg$)	**Muon Type**	**Central track matching algorithm**
3	Central track + local muon track (A and BC segments)	Muon to central if local muon track fit converges; central to muon otherwise
2	Central track + BC only	central to muon
1	Central track + A only	central to muon
0	Central track + muon hit	central to muon
-1	A segment only	no match
-2	BC segment only	no match
-3	Local muon track (A+BC)	no match

Table 2.4: Possible cases of track-muon matching. Negative number of segments corresponds to the case when matching track is not found.

scattering in the material [70]. If the measurements inside and outside the toroid are combined, local momentum measurements are obtained from the deviation angle. Such muon candidates with measured momentum are then propagated backwards to the cental tracking system, and associated with a track. In the case of successful association the measurements of track parameters are combined in a global measurement, and the error matrix is recomputed.

However, the local measurement may not be complete (e.g. only A or BC measurements may be present with no local momentum information), or local fit may not converge. In this case the tracks from the central tracking with the associated error matrices are extrapolated to the muon chambers, and the parameters of central tracks are assigned to the matched muons. The possible cases of track-muon matching are listed in Table 2.4.

Reconstructed muon candidates are classified by muon *type* and *quality*

[71]. The type is given by the number of layers in the muon system, $nseg$, associated with the muon candidate. A positive value of $nseg$ indicates that the muon reconstructed in the muon system ("local muon") was matched to a track in the central tracking system. A negative value of $nseg$ tells that the local muon could not be matched to a central track. The absolute value of $|nseg| = 1, 2$ or 3 indicates that the local muon is made up of a A-layer only hits, B- or C-layer only hits, or both A- and B- or C-layer hits.

The muon quality can be Loose, Medium, or Tight. The definitions are as follows:

- *Tight muons.* Tight muons must have $|nseg| = 3$, and
  - at least two A layer wire hits;
  - at least one layer scintillator hit;
  - at least three BC layer wire hits;
  - at least one BC scintillator hit;
  - a converged local fit.
- $|nseg| = 3$ *Medium/Loose muons.* When $|nseg| = 3$ muon candidate fails the Tight criteria it may still be Medium or Loose. An $|nseg| = 3$ muon is Medium if it has
  - at least two A-layer wire hits;
  - at least one A-layer scintillator hit;
  - at least two BC layer wire hits;
  - at least one BC scintillator hit.

  An $|nseg| = 3$ Loose muon is defined as a Medium muon but allowing one of the above tests to fail.
- $|nseg| = 2$ *Loose/Medium muons.* Muons with $|nseg| < 3$ can only be Loose or Medium if they are matched to the central track. Loose requires:

  - at least one BC layer scintillator hit;
  - at least two BC layer wire hits.

  An $|nseg| = 2$ muon is defined as Medium if it fulfills the above requirements and it is located in the bottom part of the detector.

- $|nseg| = 1$ *Loose/Medium muons.* An $nseg = +1$ muon is Loose if it has

  - at least one scintillator hit;
  - at least two A-layer wire hits.

  An $|nseg| = 1$ muon is Medium if it fulfills the above requirements and if it is located in the bottom part of the detector.

If no segment can be formed, the muon is classified as having $nseg = 0$ (see Table 2.4). The classification of wire and scintillator hits can be found in [72].

2.4 DØ upgrade for RunIIb

The 2006 shutdown marks the transition from Run IIa to Run IIb configuration of DØ detector. The major changes to the tracking system included:

- Installation of the additional radiation-hard layer of SMT (Layer 0, L0) in the inner-most part of the detector.
- Upgrade of the read-out electronics of the fiber tracker to read out the time-of-flight information for every fiber.

Also, Trigger/DAQ was upgraded to meet higher luminosity requirements expected in Run IIb. The DØRECO and the DØRECO file formats were modified accordingly.

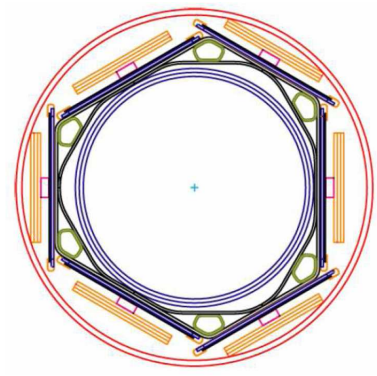

Figure 2.21: The L0 design. The six blue (dark-grey) planes near the beam pipe indicate the sensors, other six light-brown (light-grey) planes indicate the analog cables.

The addition of the SMT Layer 0 is the most important modification for the purposes of this work. L0 improves the resolution of the displaced vertices and provides increased redundancy for failures in the existing detector [73, 74]. The severe space constraints determined the L0 design. It had to be fit between the beam pipe ($r = 15$ mm) and the inner-most SMT support ($r = 23$ mm). The solution was to deploy two layers of single-sided detectors on a carbon fiber support (with pitches 71 μm for the inner and 81 μm for the outer), with the read-out chip mounted outside the fiducial region. The L0 design is shown in Fig. 2.21.

2.5 Event simulation

Event simulation is used in the analysis to estimate certain properties of the signal and background events. A full simulation of the interaction and the detector response is performed. This section outlines the simulation procedure and lists the tools.

The simulation of the physics processes is performed by one of the several event generator programs. These use theoretical knowledge and Monte Carlo techniques to generate different processes in the event. All samples used in the presented analysis were produced by Pythia [75]. Pythia uses

the leading order predictions in perturbation theory to model the interaction of two partons inside a proton and antiproton, using the experimentally known parton distribution functions (PDF). Then the hadronization of outgoing quarks is performed using a non-perturbative model. The decays of the unstable particles are also computed in Pythia. However, in the case of b-hadrons, Pythia is usually prevented from performing a decay. Instead, the decay is calculated by the EvtGen package [76], which uses the decay amplitudes to correctly model various phenomena in b-decays, including angular distributions of the products and CP-violation effects.

The events containing the decays of interest are selected at the generation stage and run through the DØ_MESS (DØ Monte Carlo Event Selection System) package [77]. DØ_MESS applies some adjustment cuts, which usually require the presence of a specified particle, which may also be required to originate from a specified parent. Some soft momentum and pseudorapidity cuts are normally applied here.

The response of the DØ detector to each selected event is then modelled. At the first stage the energy deposits in various detector subsystems are calculated in DØGSTAR [78] (DØ GEANT Simulation of the Total Apparatus Response), an implementation of the CERN GEANT package [79]. DØGSTAR contains a model of DØ detector built from many small volumes of specified materials, through which the generated particles are propagated. Then, a package called DØSIM [80] models the detector electronics to include the effect of the read-out: detector noise, inefficiencies, and the effects of data digitization.

The output of DØSIM is finally passed to DØRECO for reconstruction using the same methods as used for data. The output format is identical to real data, except that the TMB also contains the generated Monte Carlo information, in order to allow comparison of reconstructed and generated objects.

Chapter 3

Data analysis

3.1 Tools

The measurement presented in this dissertation is based on a sample of $p\overline{p}$ collisions corresponding to an integrated luminosity of 2.8 fb^{-1}, selected in RunIIa and a part of RunIIb of Tevatron during the period from April 2003 to July 2007 (see Fig. 3.1). The RunIIa part of the data sample was reconstructed using version p17 of DØRECO, with the first production release p17.03 [81]. The RunIIb part was reconstructed using version p20 of DØRECO, with the first production release p20.03 [82]. The p20 release of DØRECO reflects the DØ detector upgrade performed in 2006 (Section 2.4).

3.1.1 Triggers for B physics

The on-line selection of events for the present analysis is controlled by special triggers, used for B physics and exotic searches at DØ. The triggers relevant for B physics and their prescale factors are summarized in [83]. These triggers can be divided into three groups [84]:

1. *Impact parameter-biased single inclusive muon triggers.* These triggers identify long-lived mesons by requiring a significant impact parameter. The requirement of having a significant impact parameter

enriches data samples with events containing high lifetime mesons. Consequently, such data samples cannot be used to measure lifetimes and, correspondingly, bias B tagging.

2. *Unbiased single inclusive muon triggers* [85]. These triggers do not have requirements on the impact parameter, and therefore do not produce biased event samples. The unbiased single inclusive muon triggers are distributed over all three levels of DØ trigger system (see Section 2.2.4). As the name suggests, they require at least one muon to be detected in the muon chambers. At Level 1, there are two types of trigger bits, scintillator- and wire-based [72]. At Levels 2 and 3 muons are classified as Loose, Medium, or Tight (see Section 2.2.2). At Level 2 the transverse momentum, obtained from the muon system, can be required to be above a given threshold. At Level 3 the cut is made on the p_T of the matched central track, or, if there is no track match, using the information from the local muon system. Almost all unbiased single muon triggers for B physics require Medium muons with a $p_T > 2, 3$ or 4 GeV/c. Additionally, the position of the primary vertex is required to satisfy $|z| < 35$ cm, to reject the halo interactions. The triggers are prescaled at Level 1, usually by a factor of 2 at a luminosity above 20×10^{30} sm^{-2} s^{-1}, and turned off at a luminosity of 40×10^{30} sm^{-2} s^{-1}.

3. *Di-muon triggers* are used to look for B decays involving J/ψ or Υ. The di-muon triggers in general require at least two track-matched muons of Loose or Medium quality, with $p_T > 2$ GeV/c each. Primary vertex is required to be within $|z| < 35$ cm. The Level 1 bits require simultaneous presence of two CFT tracks and two local muons in the event. The Level 2 bits may in addition require $\eta - \phi$ separation between the tracks. Level 3 requires muons matched to central tracks. The di-muon triggers run unprescaled. Additionally, there is a special

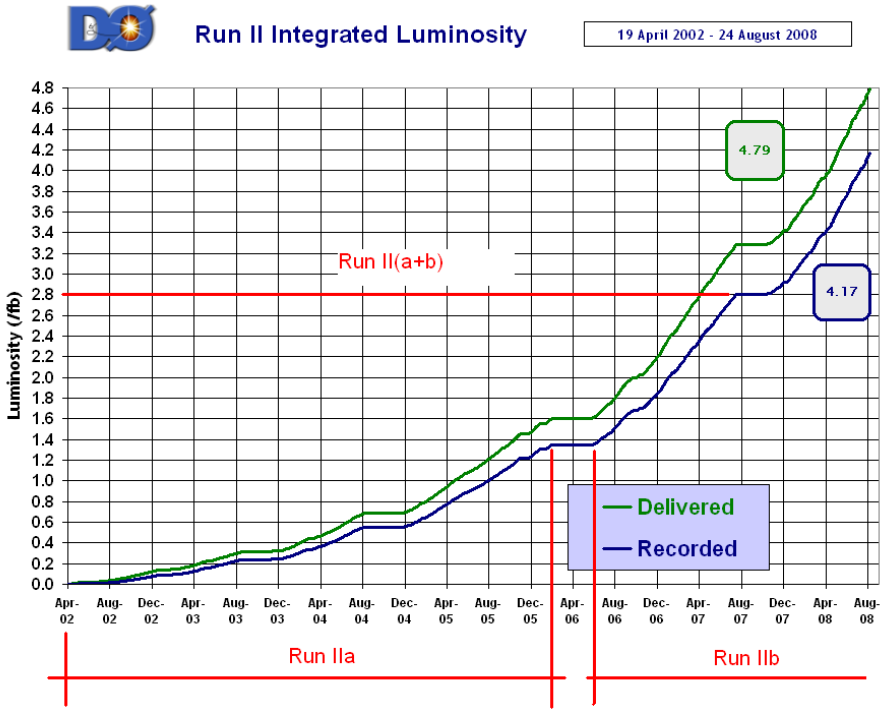

Figure 3.1: Integrated luminosity delivered by Tevatron, and the luminosity recorded by DØ in the current Run II.

Level 3 di-muon trigger which requires invariant mass of the two muons between 2.5 and 2000.0 GeV/c^2. This trigger runs unprescaled up to a luminosity of 60×10^{30} sm^{-2} s^{-1}, at which it is turned off.

The events selected for the present analysis had to satisfy the requirements of any unbiased single muon or a di-muon trigger.

3.1.2 BANA package

The analysis presented in this dissertation has been performed using the BANA package [86] that is used for many B physics analyses at DØ. The package can access data in DST and TMB DØRECO formats, but is normally used with the stand-alone format AADST. AADST contains only the information required by the B physics analyses:

- Complete track information;
- Triggers block;

- Muon ID block.

The files in this compact format can be stored directly on disk. As it is not necessary to retrieve data from the database, the development and debugging of the analysis code greatly speed up.

The BANA package provides basic methods for the B physics analysis:

- Reconstruction of primary and secondary vertices;
- Calculation of transverse and longitudinal projections of impact parameters of tracks, with errors; calculation of the combined significance of a track with respect to the primary vertex according to (2.15);
- Reconstruction of jets using the DURHAM clustering algorithm [87];
- Reconstruction of particle decays by assigning masses to non-muon tracks and combining them into parent particles. The position of decay vertex, invariant mass, and momentum of a parent particle can be calculated by the methods provided; in this way one can reconstruct basic B decays e.g. $B_{(s)} \to D_{(s)}\mu\nu$, $B \to D\pi$, $B \to J/\psi K$, decays of D, K, J/ψ and Λ;
- Constraining momenta of daughter particles from parent's mass, which allows to improve the mass resolution;
- Flavor tagging.

The defined observables can be stored in PAW [88] or ROOT [89] trees for further analysis.

3.1.3 Inclusive muon skim

From the events satisfying the ORed unbiased single muon and di-muon triggers the *single muon skim* was selected and stored on disk in AADST format. The skimming requirements were [90]:

- Muon candidate with segments in the BC or ABC layers of the muon system; local muon fit should converge;
- Matched central track with > 1 SMT hits and > 1 CFT hits;
- $p_T(\mu) > 1.5$ GeV/c.

This combination of requirements provides the broadest selection of events for B physics studies.

3.2 Detector-induced asymmetries

As it was shown in Section 1.2, the measurement of direct CP violation in $b \to sc\overline{c}$ transition using $B^+ \to J/\psi K^+$ (in $b \to dc\overline{c}$ transition using $B^+ \to J/\psi\pi^+$) technically reduces to the measurement of the charge asymmetry between $J/\psi K^+$ ($J/\psi\pi^+$) and $J/\psi K^-$ ($J/\psi\pi^-$) final states reconstructed from charged B decays. The measurement of the kaon reconstruction asymmetry using the decay $D^* \to D^0(\mu K\nu_\mu)\pi$ also reduces to the measurement of the charge asymmetry, this time between $(\mu^+K^-\nu_\mu)\pi^+$ and $(\mu^-K^+\overline{\nu}_\mu)\pi^-$ coming from $D^{*\pm}$. However, the detector can introduce apparent charge asymmetries. This happens if the detector has global or local differences in the acceptance and efficiency for positive and negative particles.

An example of global difference may be a forward-backward asymmetric production of charged particles (e.g. of muons (electrons) from the decays of asymmetrically produced W bosons), which then convolves with asymmetric reconstruction efficiency to give an apparent charge asymmetry. Let us consider this effect in closer detail. The dominant subprocess of W^+ production in $p\overline{p}$ collisions is $u + \overline{d} \to W^+$, whereas of W^- production is $\overline{u}+d \to W^-$. Since the valence u quark carries more proton momentum than the d quark, and, moreover, there are two valence u quarks, the $W^+(W^-)$ should preferably be produced in the proton (anti-proton) direction. The

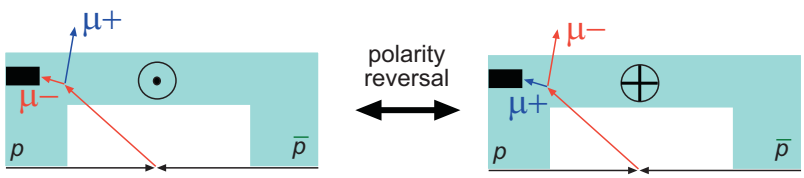

Figure 3.2: Polarity reversal helps reduce systematic effects by exposing different parts of the detector to the same flux of oppositely charged particles.

same correlation should be observed in their decay products – muons and electrons. This effect was measured at CDF by looking at the pseudorapidity distribution of the electrons produced in the decays of W [91]. If, in addition to the forward-backward asymmetric production of charged particles, the detector itself is forward-backward asymmetric, we observe an apparent charge asymmetry of the W decay products.

The local difference may arise if e.g. the tracks bending in opposite directions inside the solenoid/toroid are reconstructed with different efficiencies due to specific distribution of the dead material.

As noted in Section 2.2, the polarities of DØ magnets, those of both the solenoid and the toroid, are regularly reversed during the data-taking. After the magnet polarity is reversed, the same part of the detector is exposed to the flux of particles of the opposite charge (see Fig. 3.2). So, the net effect of the global differences in reconstruction efficiencies of positive and negative tracks cancels if we consider data samples that have equal event counts for each toroid/solenoid polarity. In practice, however, it is not possible or desirable to reduce the data sample collected at one polarity to bring it in correspondence with the data sample collected at the opposite polarity. Instead, to account for the different size of samples collected at the opposite polarities and for possible detector-induced asymmetries we proceed as follows. We divide the initial sample of events into subsamples according to the polarity of the toroid/solenoid, β, the particle's direction, γ ($\gamma = +1$ for $\eta > 0$), and its charge, q. There are $2^3 = 8$ subsamples corresponding

to 8 possible combinations of β, γ, and q. In the ideally symmetric process measured by an ideally symmetric detector on equal amount of data at both polarities, all the subsamples contain the same number of events,

$$n_q^{\beta\gamma} = \frac{1}{4} N \epsilon^\beta = \frac{1}{8} N, \tag{3.1}$$

where $\epsilon^\beta = \frac{1}{2}$ is the fraction of signal events with toroid/solenoid polarity β.

Now, if the number of positively charged events differs from the number of negatively charged events due to the physics asymmetry A (for example, due to CP violation asymmetry) then the sizes of subsamples of opposite charge q differ proportionally:

$$n_q = \frac{1}{2} N (1 + qA). \tag{3.2}$$

The asymmetry A can be found by dividing the initial sample into two subsamples and solving for A. The exact solution is simply the definition of the charge asymmetry:

$$A = \frac{n_+ - n_-}{n_+ + n_-}. \tag{3.3}$$

However, in the case of the asymmetric forward-backward particle production, there may be a different number of particles of fixed sign q reconstructed in the forward ($\gamma > 0$) and backward ($\gamma < 0$) parts of the detector. Thus, we will observe asymmetry between the number of events with $q\gamma > 0$ and $q\gamma < 0$, $A_{q\gamma} \equiv A_{fb}$. The number of events in subsamples will differ in addition due to A_{fb}:

$$n_q^\gamma = \frac{1}{4} N (1 + qA)(1 + q\gamma A_{fb}). \tag{3.4}$$

For small asymmetries, neglecting higher orders, the system (3.4) can be considered linear:

$$n_+^+ = \frac{1}{4} N (1 + A + A_{fb}) \tag{3.5}$$

$$n_-^+ = \frac{1}{4} N (1 - A - A_{fb}) \tag{3.6}$$

$$n_+^- = \frac{1}{4} N (1 + A - A_{fb}) \tag{3.7}$$

$$n_-^- = \frac{1}{4} N (1 - A + A_{fb}). \tag{3.8}$$

Then the solutions for A and A_{fb} decouple: we add (3.5) and (3.7) to solve for A, and add (3.5) and (3.8) to solve for A_{fb}. However, we do not know in advance the size of detector asymmetries. So, for the sake of generality and exactness, the system (3.4) should be solved explicitly using numerical methods.

To complete the model, the following detector asymmetries have to be accounted for, which adds corresponding terms to (3.4) in a similar manner:

- Asymmetry accounting for the change in the reconstruction efficiency of particles of charge q after toroid polarity flip. This is therefore the asymmetry between the number of events with $q\beta > 0$ and $q\beta < 0$, $A_{q\beta}$;

- Detector north-south asymmetry accounting for the different distribution of dead material, and, therefore, different reconstruction efficiency in the northern ($\gamma > 0$) and southern ($\gamma < 0$) parts of the detector, A_{γ};

- Asymmetry accounting for the range-out of particles in the magnet. This effect is most pronounced for muons in the toroid: magnetic field pulls the muons passing close to the toroid end into the gap between the central and the end toroid, where the reconstruction efficiency for muons drops (see Fig. 3.3). The range-out effect is expected to be the dominant detector asymmetry for muons due to the detector geometry. For particles reconstructed in the tracking system inside the solenoid (e.g. kaons) there is no range-out and the corresponding asymmetry is expected to be negligible. As inferred from Fig. 3.3, the range-out effect changes sign if q, β, or γ changes sign, so this is an asymmetry between events with $q\beta\gamma > 0$ and those with $q\beta\gamma < 0$, $A_{q\beta\gamma} \equiv A_{ro}$;

- The last asymmetry that completes the system accounts for any detector-related forward-backward asymmetries which remain after toroid po-

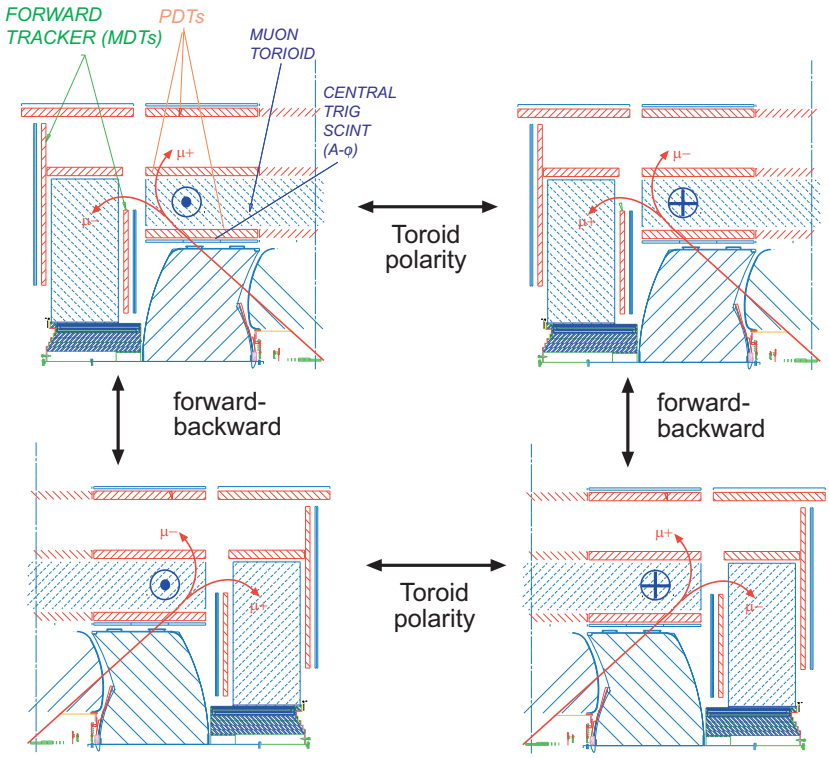

Figure 3.3: The range-out changes when the sign of either q, β, or γ changes.

larity flip. This is therefore an asymmetry between the events with $\beta\gamma > 0$ and $\beta\gamma < 0$, $A_{\beta\gamma}$.

To summarize, the number of events in eight $\beta\gamma q$ subsamples may differ due to the unequal number of event counts at different magnet polarities, $\epsilon^{\beta} \neq \frac{1}{2}$, to the physics charge asymmetry A, and to various detector-related asymmetries A_i. This is reflected in the following detector model:

$$\begin{aligned} n_q^{\beta\gamma} &= \frac{1}{4} N \epsilon^{\beta} (1 + qA)(1 + q\gamma A_{fb})(1 + \gamma A_{det})(1 + q\beta\gamma A_{\beta\gamma q})(1 + q\beta A_{q\beta}) \\ &\times (1 + \beta\gamma A_{\beta\gamma}). \end{aligned} \tag{3.9}$$

Eq. (3.9) suggests a method of disentangling detector-related asymmetries:

1. We divide the initial sample into 8 subsamples corresponding to 8 combinations of particle charge, q, pseudorapidity, γ, and magnet polarity, β;

2. In every subsample we extract the number of signal events, $n_q^{\beta\gamma}$, by whatever method is appropriate (mass peak fit, sideband subtraction of the background under the peak, etc.);

3. Then we solve the system (3.9) for N, ϵ^β, and six asymmetries. In this way we account for the difference in the signal counts at different magnet polarities and disentangle the detector-induced asymmetries at all orders of magnitude.

In all that follows our main interest will be in the charge asymmetry, A.

3.3 Measurement of the kaon charge asymmetry using the decay $D^0 \to \mu^+ K^- \nu_\mu$

As mentioned in Section 1.4.3, a sizable kaon reconstruction asymmetry (from now on dubbed simply "kaon asymmetry") is expected, because positive and negative kaons have different cross-section of inelastic interaction with matter. For kaons, $\sigma(K^- d) > \sigma(K^+ d)$ (d – deuterium) [13], which is explained by the quark content: $K^-(s\overline{u})$ does interact inelastically with $p\,(uud)$ and $n\,(udd)$ to form resonances $\Sigma^+(uus)$ and $\Lambda^0(uds)$, but $K^+(\overline{s}u)$ does not. Thus, the negative kaon asymmetry develops,

$$A_K = \frac{N(K^-) - N(K^+)}{N(K^-) + N(K^+)} < 0. \tag{3.10}$$

A_K is a function of the material distribution in a particular detector, which can be seen as follows. The nuclear interaction length of a particle in the material is

$$l_0 = \frac{A}{\sigma N_A \rho}, \tag{3.11}$$

where A is an atomic weight of the material, ρ is the density of the material, $N_A = 6.02 \times 10^{23}$ mol^{-1} is the Avogadro number. The loss of particles ΔN in the length l due to inelastic interactions is

$$\frac{\Delta N}{N} = 1 - \exp\left(-\frac{l}{l_0}\right), \tag{3.12}$$

where N is the initial number of particles, l_0 is a nuclear interaction length. Let us assume that the positive and negative particles of the type i are produced in the charge conjugate processes in the equal amount, N, and are lost only due to the inelastic interactions with nuclei in the detector material. Then the reconstruction asymmetry A_i developing on the length l is:

$$\begin{aligned} A_i &= \frac{N^- - N^+}{N^- + N^+} \\ &= \frac{(N - \Delta N^-) - (N - \Delta N^+)}{(N - \Delta N^-) + (N - \Delta N^+)} \\ &= \frac{1}{2}\left[\frac{\Delta N^+}{N} - \frac{\Delta N^-}{N}\right] = \frac{1}{2}\left[\exp\left(-\frac{l}{l_0^-}\right) - \exp\left(-\frac{l}{l_0^+}\right)\right], \end{aligned} \tag{3.13}$$

where l_0^- (l_0^+) is a nuclear interaction length of negative (positive) particle in the material.

The kaon asymmetry A_K adds to any CP violation asymmetry A_{CP} due to the Standard Model or possible New Physics effects in the processes where a single kaon in the final state is reconstructed, as e.g. in the decay $B^+ \to J/\psi K^+$:

$$n_q = \frac{1}{2}\left(1 + qA_{CP}\right)\left[1 + qA_K(J/\psi K)\right]. \tag{3.14}$$

Neglecting higher order terms, (3.14) can be written as:

$$\begin{aligned} n_q &\approx \frac{1}{2}\left(1 + qA_{CP} + qA_K\right) \\ &= \frac{1}{2}\left[1 + q(A_{CP} + A_K)\right] \\ &= \frac{1}{2}\left(1 + qA\right). \end{aligned}$$

E.g. in the case of $B^+ \to J/\psi K^+$ decay, A_K is the kaon charge asymmetry in the $J/\psi K$ sample, and A is the charge asymmetry between $B^- \to J/\psi K^-$ and $B^+ \to J/\psi K^+$ as measured in the detector. The CP violation asymmetry is therefore simply:

$$A_{CP} = A - A_K. \tag{3.15}$$

3.3.1 Choice of the decay channel

We measure the detector-induced kaon asymmetry in the process where the physics charge asymmetry is expected to be zero: we compare the rate of $c \to s$ quark transition in the decay chain

$$c \to D^{*+} \to D^0\pi^+,\ D^0 \to \mu^+K^-\nu_\mu, \tag{3.16}$$

and in the charge conjugate process, using the muon charge as a D^* flavor tag. As shown in Section 1.4.3, it is theoretically very safe to attribute all the asymmetry between $\mu^+K^-\pi^+$ and $\mu^-K^+\pi^-$ measured in this channel to the kaon asymmetry.

3.3.2 Event selection

The $D^* \to D^0(\mu\nu K)\pi$ events are selected from the 2.8 fb^{-1} sample collected by the DØ experiment in Run II of the Fermilab Tevatron collider. The selection cuts are summarized in Table 3.1. Muons are required to have the transverse momentum $p_T > 2$ GeV/c, and to leave signal in at least two layers of the muon system, $nseg > 1$ (see Section 2.3.3 for a detailed description of the $nseg$ variable). The D^0 candidate is reconstructed from the muon track by adding another track, which is assigned a kaon mass. The invariant mass of the two tracks is required to be in the window $1.2 < m(\mu K) < 2.2$ GeV/c^2. The requirement $m(\mu K) < 2.2$ GeV/c^2 is chosen to include the sideband of D^0 peak. The requirement $m(\mu K) > 1.2$ GeV/c^2 suppresses the events $D^0 \to K^*\mu\nu$, with subsequent decay $K^{*-} \to K^0\pi^-$. If a π^- is wrongly identified as a K^-, a D^0 candidate is formed from a muon and a pion. The invariant mass distribution of the $\mu\pi$ system dies out kinematically at $m(D^0) - m(K^0) \approx 1.37$ GeV/c^2 (overestimate, since the neutrino from the D^0 decay escapes detection). We account for the remaining contamination from this process in the sample composition.

The D^* candidate is reconstructed by adding a third track associated with the same primary vertex as the muon. It is assigned a pion mass,

Quantity	Cut
All tracks:	
#hits in SMT	> 1
#hits in CFT	> 1
Muon:	
$nseg$	> 1
Transverse momentum	> 2.0 GeV/c
Kaon:	
p_T	> 0.5 GeV/c
Pion:	
Combined significance of the pion track with respect to the primary vertex	$S_\pi < 9$
D^0 candidate:	
mass $m(\mu K)$	$1.2 < m(\mu K) < 2.2$ GeV/c^2
The angle between the D^0 momentum and the direction from the primary vertex to the D^0 vertex in the transverse plane	$\cos(\alpha_T^{D^0}) > 0.9$
Combined significance of the D^0 track with respect to the primary vertex	$S_{D^0} < 16$
Distance to the primary vertex in the transverse plane	$L_{xy}(D^0)/\sigma[L_{xy}(D^0)] > 3$
D^* candidate:	
mass difference $\Delta m = m(\mu K\pi) - m(\mu K)$	$\Delta m < 0.22$ GeV/c^2

Table 3.1: Summary of the event selection cuts for the $D^* \to D^0(\mu\nu K)\pi$ decay.

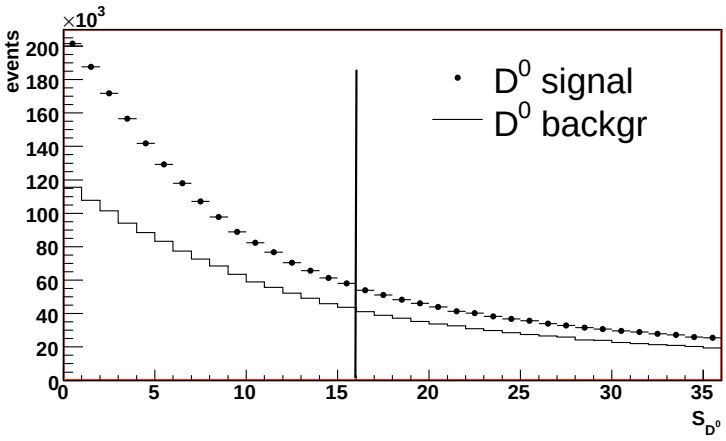

Figure 3.4: The combined significance of the D^0 with respect to the primary vertex for the events with $1.35 < m(\mu K) < 1.65$ GeV/c^2 ("D^0 signal"), and $1.90 < m(\mu K) < 2.20$ GeV/c^2 ("D^0 background"). The invariant mass distribution of the μK system, $m(\mu K)$, is shown in Fig. 3.5. The vertical line shows the cut applied in this analysis.

the invariant mass of the $\mu K\pi$ system is computed and the mass difference $\Delta m = m(\mu K\pi) - m(\mu K)$ is required to be $\Delta m < 0.22$ GeV/c^2.

All tracks are required to have signals in both SMT and CFT and to form a common vertex using a method described in Section 2.3.2. The primary vertex of the $p\bar{p}$ interaction is determined for each event using the method described in the same section. The pion track is used to determine the axial, ϵ^d, and stereo, ϵ^z, projections of the impact parameter with respect to the primary vertex, together with the corresponding errors, $\sigma(\epsilon^d)$ and $\sigma(\epsilon^z)$. The combined significance of the pion with respect to the primary vertex is defined according to (2.15):

$$S_\pi = \left(\frac{\epsilon^d_\pi}{\sigma(\epsilon^d_\pi)}\right)^2 + \left(\frac{\epsilon^z_\pi}{\sigma(\epsilon^z_\pi)}\right)^2. \tag{3.17}$$

To reduce the combinatorial background from b decays, we require $S_\pi < 9$.

The track of the D^0 is assumed to pass through the reconstructed vertex and to be directed along the momentum of the μK system. The combined significance of D^0, S_{D^0}, is defined similarly to (3.17). The distribution of S_{D^0} for the events with $1.35 < m(\mu K) < 1.65$ GeV/c^2 ("D^0 signal"), and

$1.90 < \Delta m < 2.20$ GeV/c^2 ("D^0 background") is shown in Fig. 3.4. The requirement on S_{D^0} is less tight, $S_{D^0} < 16$, since neutrinos from D^0 decay escape detection and introduce an uncertainty in the D^0 track reconstruction.

To ensure that the D^0 comes from the primary vertex, the cosine of the angle between the D^0 momentum and the direction from the primary vertex to the D^0 vertex is required to be greater than 0.9. The distance L_{xy} in the transverse plain from the primary vertex to the D^0 decay vertex is required to satisfy $L_{xy}/\sigma(L_{xy}) > 3$, to ensure the selection of the long-lived D^0 mesons.

The D^* mesons can come from the decays of B^0 mesons, which are CP asymmetric. However, only the semileptonic CP asymmetry does not vanish when integrated over time [92]. The semileptonic asymmetry in B^0 mixing is predicted theoretically at the order of 10^{-3} [93], and experimentally measured to be consistent with zero (see the review of the measurements as of end 2007 in the HFAG report [21]). This asymmetry is diluted by the fraction of the semileptonic decays in the inclusive $B^0 \to D^*X$ sample, estimated from [13] to be $\mathrm{Br}(B^0 \to D^*\mu\nu_\mu)/\mathrm{Br}(B^0 \to D^*X) < 0.24$. The semileptonic asymmetry in the selected sample is further diluted by the contribution from decays of other b hadrons, and can be safely neglected.

3.3.3 Signal extraction

The invariant mass distribution of the μK system for all selected events is shown in Fig. 3.5. It has a peak shifted to the lower values from the D^0 mass, $m(D^0) = 1.86$ GeV/c^2, and smeared due to the neutrino from $D^0 \to \mu K\nu$ which escapes detection. The D^* resonance is easily observed in the mass difference $\Delta m = m(\mu K\pi) - m(\mu K)$, due to the cancellation of the mass shifts from the neutrino loss (see Fig. 3.6). No charge correlations are required at this stage.

We select signal (background) subsamples by requiring the charge cor-

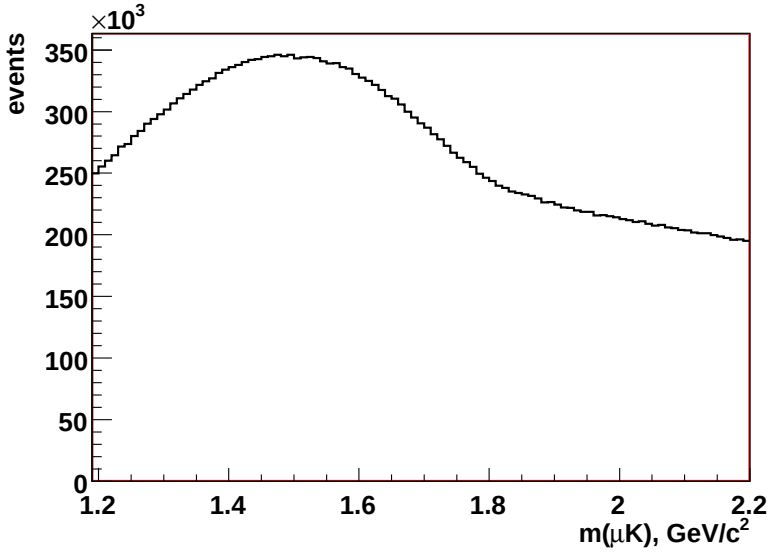

Figure 3.5: The invariant mass distribution of the μK system. The wide peak is due to the resonance from the decay $D^0 \to \mu K \nu_\mu$, smeared by the neutrino loss.

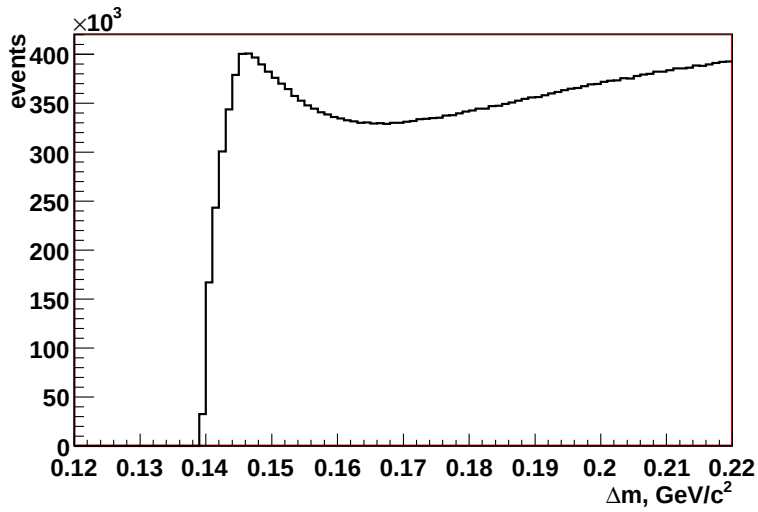

Figure 3.6: The distribution of the mass difference $\Delta m = m(\mu K \pi) - m(\mu K)$, which allows to clearly see the resonance $D^* \to (\mu K \nu)\pi$.

relations which do (do not) match the topology of the D^* decay (3.16). To select the D^* signal we require:

$$q_\mu \cdot q_K < 0 \text{ and } q_\mu \cdot q_\pi > 0. \tag{3.18}$$

To describe the combinatorial background under the D^* peak, we require $q_\mu \cdot q_K > 0$. At this point we can further require $q_\mu \cdot q_\pi > 0$ or $q_\mu \cdot q_\pi < 0$. Among the three choices

$$q_\mu \cdot q_K > 0, \tag{3.19}$$

$$q_\mu \cdot q_K > 0 \text{ and } q_\mu \cdot q_\pi < 0, \tag{3.20}$$

$$q_\mu \cdot q_K > 0 \text{ and } q_\mu \cdot q_\pi > 0, \tag{3.21}$$

we expect that the combination of three tracks of the same charge according to (3.21) corresponds to the combinatorial background best of all. To verify this suggestion, we use the following technique.

"Background 1" consists of the events from the sideband of the D^0 peak, $1.9 < m(\mu K) < 2.2$ GeV/c^2, which satisfy the charge correlation (3.18). The Δm distribution of the events in the "Background 1" is shown as a histogram with error bars in Fig. 3.7, a), c), e). "Background 2" consists of the events from the full $m(\mu K)$ region, $1.2 < m(\mu K) < 2.2$ GeV/c^2, which satisfy the alternative charge correlations (3.19)-(3.21). The corresponding Δm distributions are shown as solid histograms in Fig. 3.7, a), c), e). On the right-hand part of Fig. 3.7, b), d), f), the two corresponding histograms from the left are compared by dividing and fitting to a straight line. As one can see, requiring tracks of different charges by (3.19) and (3.20) allows a resonance process to get through. However, requiring all three tracks to have the same charge by (3.21) is the best way of describing the combinatorial background in the sidebands of the D^0 peak, as it was expected beforehand.

From now on we call "right sign" the events selected by (3.18), and "wrong sign" the events selected by (3.21). The $m(\mu K)$ distributions for

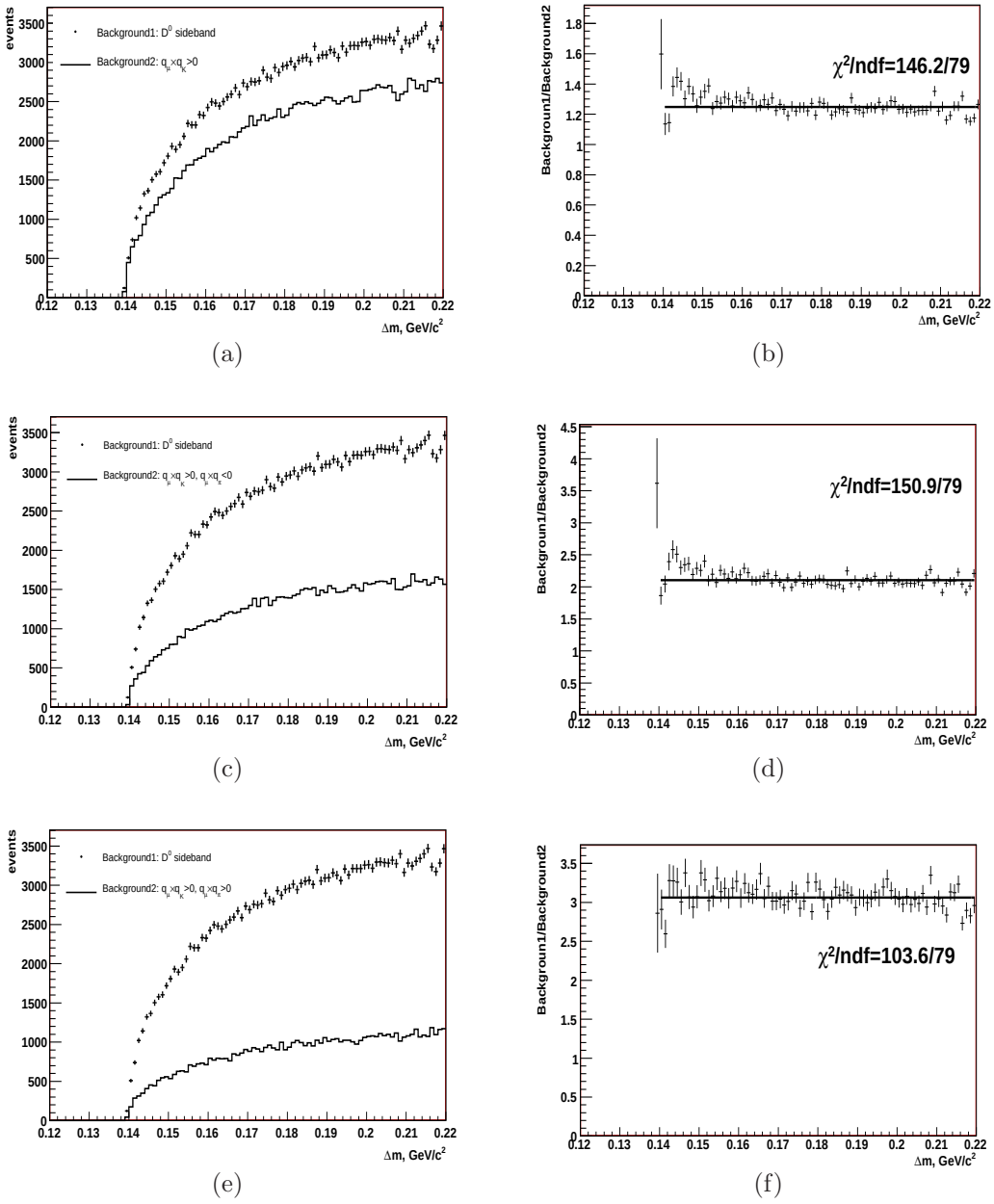

Figure 3.7: Δm distributions in the sideband of the D^0 peak of Fig. 3.5. a), c), e): histogram with error bars − after requiring the charge correlation (3.18); solid histograms − after requiring the charge correlations (3.19)-(3.21) respectively. b), d), f): ratio of the two histograms, fitted to a straight line.

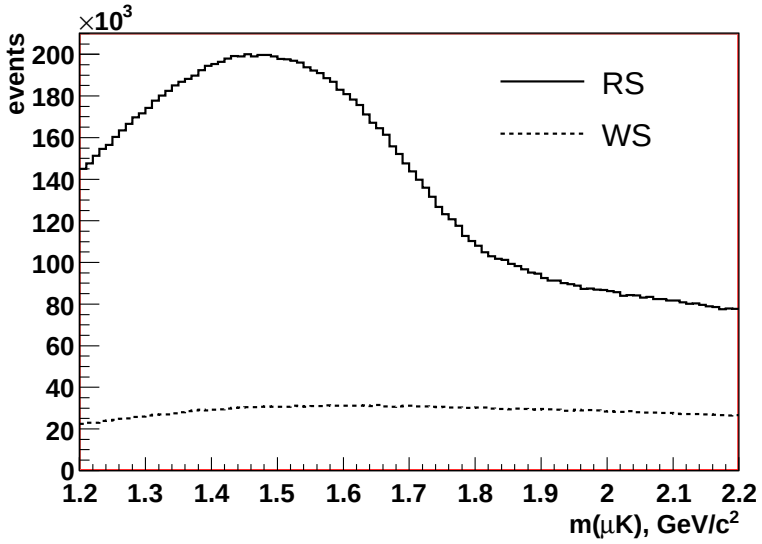

Figure 3.8: The distribution of the μK invariant mass for right sign (RS) events, selected by $q_\mu \cdot q_K < 0$, $q_\mu \cdot q_\pi > 0$, and wrong sign (WS) events, selected by $q_\mu \cdot q_K > 0$, $q_\mu \cdot q_\pi > 0$.

right sign (RS) and wrong sign (WS) events are shown in Fig. 3.8. The corresponding Δm distributions are shown in Fig. 3.9.

The combinatorial background under the D^* peak of Fig. 3.9 is renormalized and sideband subtracted as follows. The sideband is chosen far from the D^* peak, in the range $0.19 < \Delta m < 0.22$ GeV/c^2. The signal band is chosen from $\Delta m = 0.14$ GeV/c^2 to the upper bound which is varied to maximize the signal significance $S/\sqrt{S+B}$, where S and B are defined below. Let N_{sig}^{WS} and N_{side}^{WS} be the number of wrong sign events in the signal and the sideband. Let N_{sig}^{RS} and N_{side}^{RS} be the number of right sign events in the signal and the sideband. To obtain the number of signal events in the D^* peak, we renormalize the number of wrong sign events in the signal band, N_{sig}^{WS}, to the number of right sign events in the sideband, N_{side}^{RS}, and subtract the result from the number of right sign events in the signal band:

$$B = \frac{N_{side}^{RS}}{N_{side}^{WS}} N_{sig}^{WS}, \qquad S = N_{sig}^{RS} - B. \tag{3.22}$$

We optimize the position of the upper bound of the signal band by maximizing the significance $S/\sqrt{S+B}$.

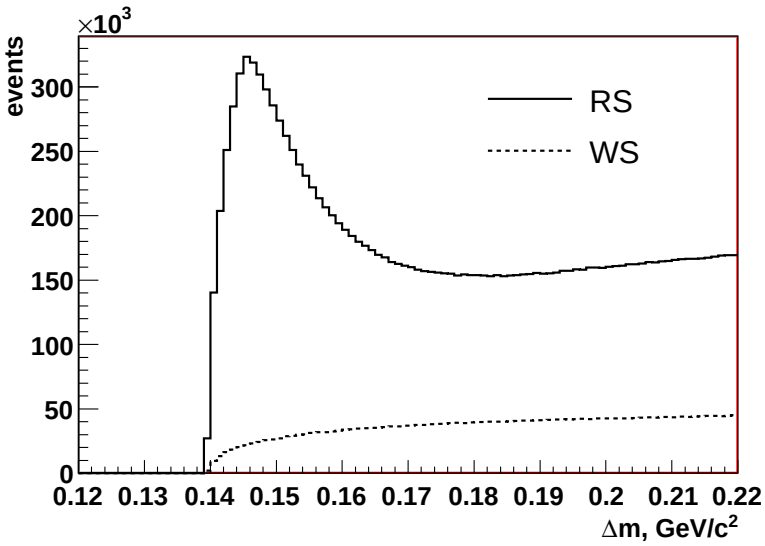

Figure 3.9: The Δm distribution for right sign (RS) and wrong sign (WS) events.

Note, that the width of the Δm peak, and, therefore, the optimal position of the upper signal bound, is different in different $m(\mu K)$ regions (see Fig. 3.10). Therefore, using just one common upper bound would result in the loss of significance. To avoid this, we divide the range $1.2 < m(\mu K) < 1.9$ GeV/c^2 in seven equal bins, and investigate the dependence of the signal significance on the position of the upper signal bound in each bin (see Fig. 3.11). Using the optimal upper signal bound in every $m(\mu K)$ bin, we determine S according to (3.22) separately in seven $m(\mu K)$ bins. The total number of signal events is obtained by summing the numbers S over seven $m(\mu K)$ bins. The total number of background events is obtained by summing the numbers N_{sig}^{WS} over seven $m(\mu K)$ bins.

3.3.4 Solving the detector model

We remind here that the kaon asymmetry is measured as a charge asymmetry A between the $D^{*+} \to D^0(\mu^+ K^- \nu_\mu)\pi^+$ and $D^{*-} \to \overline{D}^0(\mu^- K^+ \overline{\nu}_\mu)\pi^-$ events

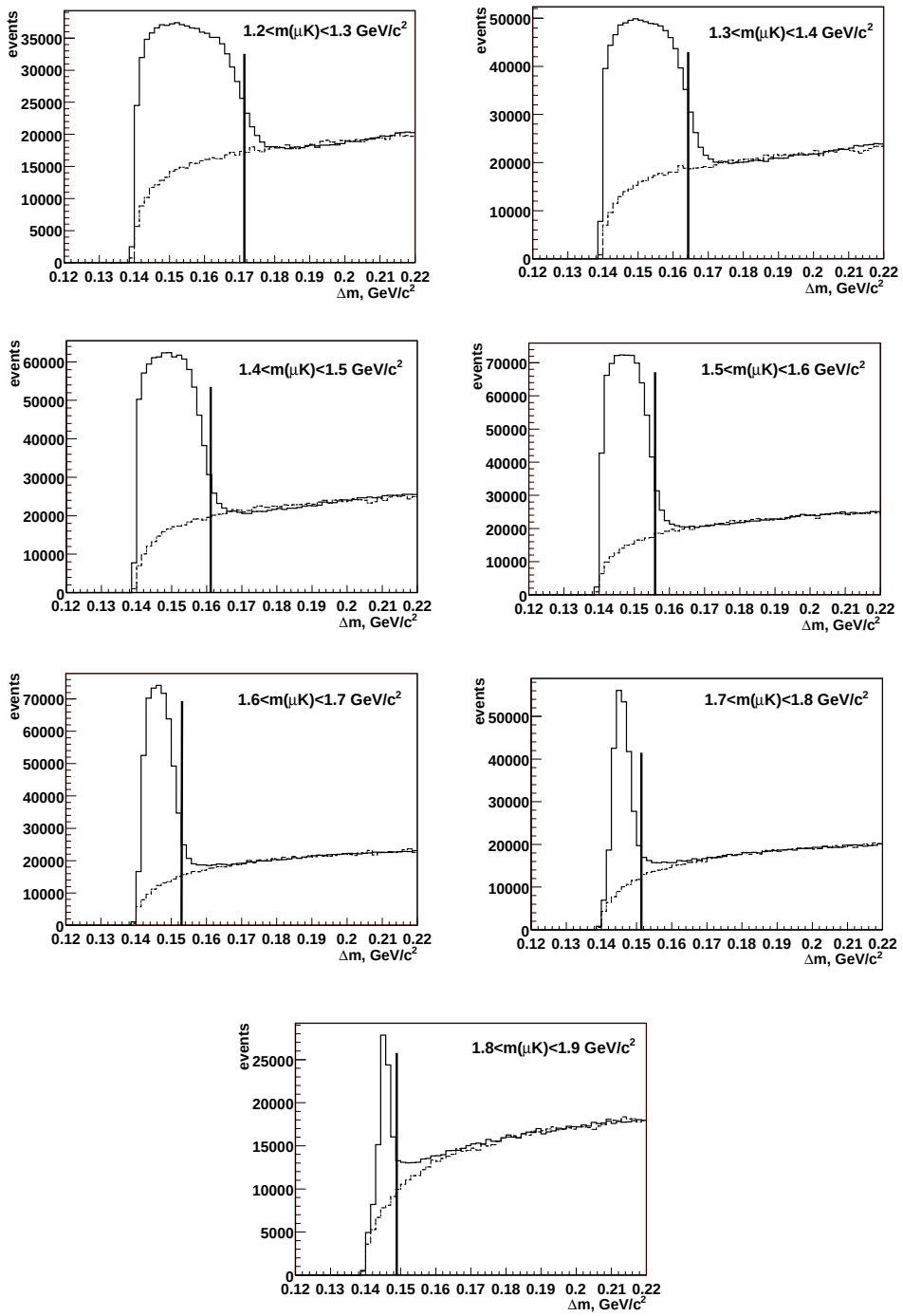

Figure 3.10: Signal distribution (solid line) and background distribution (dashed line) for different $m(\mu K)$ bins. The background distribution is rescaled to fit the tail of the signal distribution for visual clarity. The side band is chosen in the range $0.19 < \Delta m < 0.22$ GeV/c^2. The signal band is defined from $\Delta m = 0.14$ GeV/c^2 to the optimal cut (vertical line) which maximizes the significance $S/\sqrt{S+B}$, where S and B are defined in the text.

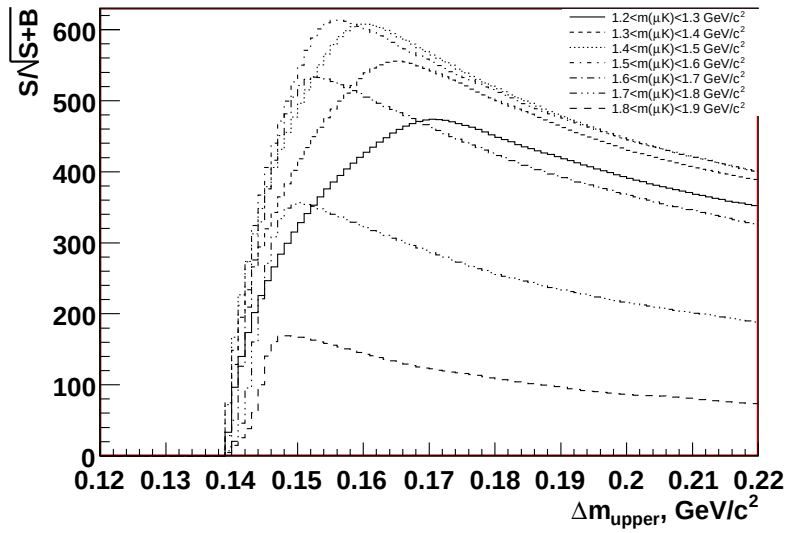

Figure 3.11: The dependence of the signal significance $S/\sqrt{S+B}$ on the position of the upper signal bound for seven $m(\mu K)$ bins from Fig. 3.10.

Subsample $\beta\gamma q$	$n_q^{\beta\gamma}$ (Signal, events)	$n_q^{\beta\gamma}$ (Backgr, events)
$+++$	$331,060 \pm 839$	$32,267 \pm 179$
$+-+$	$348,247 \pm 870$	$34,216 \pm 185$
$++-$	$358,092 \pm 880$	$34,278 \pm 185$
$+--$	$332,842 \pm 836$	$31,661 \pm 178$
$-++$	$345,522 \pm 870$	$35,622 \pm 189$
$--+$	$323,732 \pm 827$	$32,456 \pm 180$
$-+-$	$337,379 \pm 842$	$32,698 \pm 180$
$---$	$356,122 \pm 874$	$35,011 \pm 187$

Table 3.2: The numbers of D^* events $n_q^{\beta\gamma}$ in eight subsamples for the signal and the background. Nominal definition of the background according to (3.21) is used.

	Signal	Backgr
N	$2,733,000 \pm 2,000$	$268,200 \pm 500$
ϵ^+	0.5014 ± 0.0004	0.4938 ± 0.0010
A	-0.0131 ± 0.0009	0.0034 ± 0.0019
A_{fb}	-0.0006 ± 0.0009	0.0029 ± 0.0019
A_{det}	0.0042 ± 0.0009	0.0057 ± 0.0019
A_{ro}	-0.0304 ± 0.0009	-0.0374 ± 0.0019
$A_{q\beta}$	0.0048 ± 0.0009	0.0009 ± 0.0019
$A_{\beta\gamma}$	0.0014 ± 0.0009	-0.0005 ± 0.0019

Table 3.3: The physics and detector asymmetries for the D^* and the background events (MINUIT output). Uncertainties are statistical.

using muon charge as a D^* flavor tag. According to the method described in Section 3.2, the event sample is divided into eight subsamples, corresponding to all possible combinations of the toroid polarity $\beta = \pm 1$, the sign of the muon pseudorapidity $\gamma = \pm 1$, and the sign of the muon charge $q = \pm 1$, see Table 3.2. The number of events in the D^* peak and in the combinatorial background under the peak is obtained in each subsample by the sideband subtraction method described in the previous section. The extracted numbers of D^* events are used to disentangle the detector-induced asymmetries by solving Eq. (3.9) using MINUIT [94]. The results are presented in Table 3.3, separately for the D^* events and the background. We see that the measured charge asymmetry of D^* events, $A = -0.0131 \pm 0.0009$, is negative as expected. Also, the largest detector asymmetry for both the D^* signal and the background is the range-out asymmetry A_{ro}, as expected. Note, that the charge asymmetry in the combinatorial background, 0.0034 ± 0.0019, deviates from zero by not more than two standard deviations.

For the cross-check, the analysis is repeated with background selected by (3.20), see Tables 3.4 and 3.5. Note, that the charge asymmetry calculated with alternative background differs from the nominal value, -0.0131, by

Subsample $\beta\gamma q$	$n_q^{\beta\gamma}$ (Signal, events)	$n_q^{\beta\gamma}$ (Backgr, events)
$+++$	$357,195 \pm 776$	$40,279 \pm 201$
$+-+$	$376,141 \pm 802$	$41,121 \pm 205$
$++-$	$386,439 \pm 812$	$42,055 \pm 205$
$+--$	$358,612 \pm 774$	$38,730 \pm 197$
$-++$	$373,622 \pm 802$	$44,064 \pm 210$
$--+$	$349,229 \pm 766$	$40,013 \pm 200$
$-+-$	$363,460 \pm 780$	$39,883 \pm 200$
$---$	$384,024 \pm 807$	$43,158 \pm 208$

Table 3.4: The numbers of D^* events $n_q^{\beta\gamma}$ in eight subsamples for the signal and the background. The background is defined according to (3.20).

	Signal	Backgr
N	$2,949,000 \pm 2,000$	$330,300 \pm 570$
ϵ^+	0.5014 ± 0.0004	0.4942 ± 0.0009
A	-0.0123 ± 0.0007	0.0082 ± 0.0017
A_{fb}	-0.0005 ± 0.0007	0.0061 ± 0.0017
A_{det}	0.0044 ± 0.0007	0.0069 ± 0.0017
A_{ro}	-0.0311 ± 0.0007	-0.0377 ± 0.0017
$A_{q\beta}$	0.0048 ± 0.0007	0.0021 ± 0.0017
$A_{\beta\gamma}$	0.0009 ± 0.0007	0.0026 ± 0.0017

Table 3.5: The physics and detector asymmetries for the D^* and the background events, background selected by (3.20). Uncertainties are statistical.

No	Mode	Br, %
1	$\mu^+K^-\nu$	3.51 ± 0.11
2	$\mu^+K^{*-}(K^-\pi^0)\nu$	$0.72 \pm 0.05^*$
3	$\mu^+K^{*-}(K^0\pi^-)\nu$	see text
4	$\mu^+\pi^-\nu$	0.28 ± 0.02
5	$\mu^+\rho^-(\pi^-\pi^0)\nu$	0.19 ± 0.04

Table 3.6: D^* sample composition: contributing D^0 decay modes.
$^*\mathrm{Br}(\mu^+K^{*-}(K^-\pi^0)\nu) = 1/3\,\mathrm{Br}(\mu^+K^{*-}\nu)$.

only +0.0008. This difference is assigned as a systematic uncertainty from the background description. Note also, that there is a significant charge asymmetry, 0.0082 ± 0.0017, in the background selected by (3.20). This is not surprising, since, as already shown, (3.20) does not provide the best description of the combinatorial background, and some charge asymmetric signal can penetrate.

3.3.5 Sample composition

The measured charge asymmetry of D^* events is $A = -0.0131 \pm 0.0009$. It is related to the kaon asymmetry A_K via

$$A = f_K\, A_K + f_\pi\, A_\pi, \tag{3.23}$$

where f_K is a fraction of modes with a kaon in the final state, f_π is a fraction of modes with a pion in the final state, which contribute since a pion may be misidentified as a kaon. The branching fractions of the leading D^0 decay channels are taken from PDG [13] and listed in Table 3.6. Modes 1 and 2 constitute a signal, modes 3-5 are included into background. The contribution of the decay $\mu^+K^{*-}\nu$, where K^{*-} subsequently decays into $K^0\pi^-$, and a pion is misidentified as a kaon, is suppressed kinematically for $m(\mu K) > 1.2$ GeV/c^2. The remaining contamination is estimated as follows.

Using a part of available statistics corresponding to approximately 1M

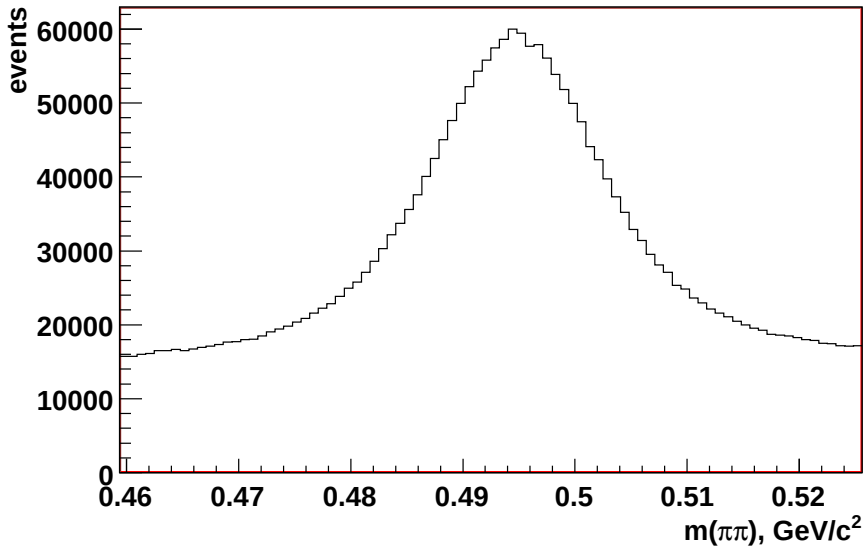

Figure 3.12: The distribution of the invariant mass of two pions selected in addition to the $\mu K\pi$ system.

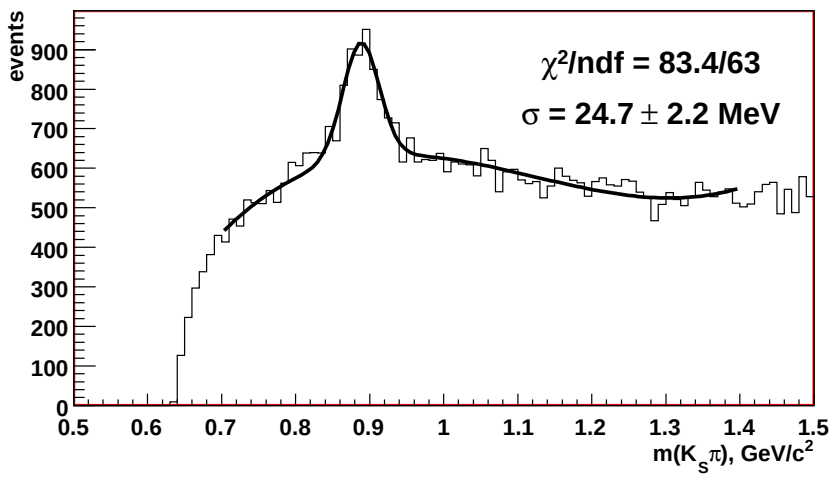

Figure 3.13: The distribution of the invariant mass of the $K_S\pi$ system in the signal region of the whole $m(\mu K)$ range, $1.2 < m(\mu K) < 1.9$ GeV/c^2. The fit function is explained in the text.

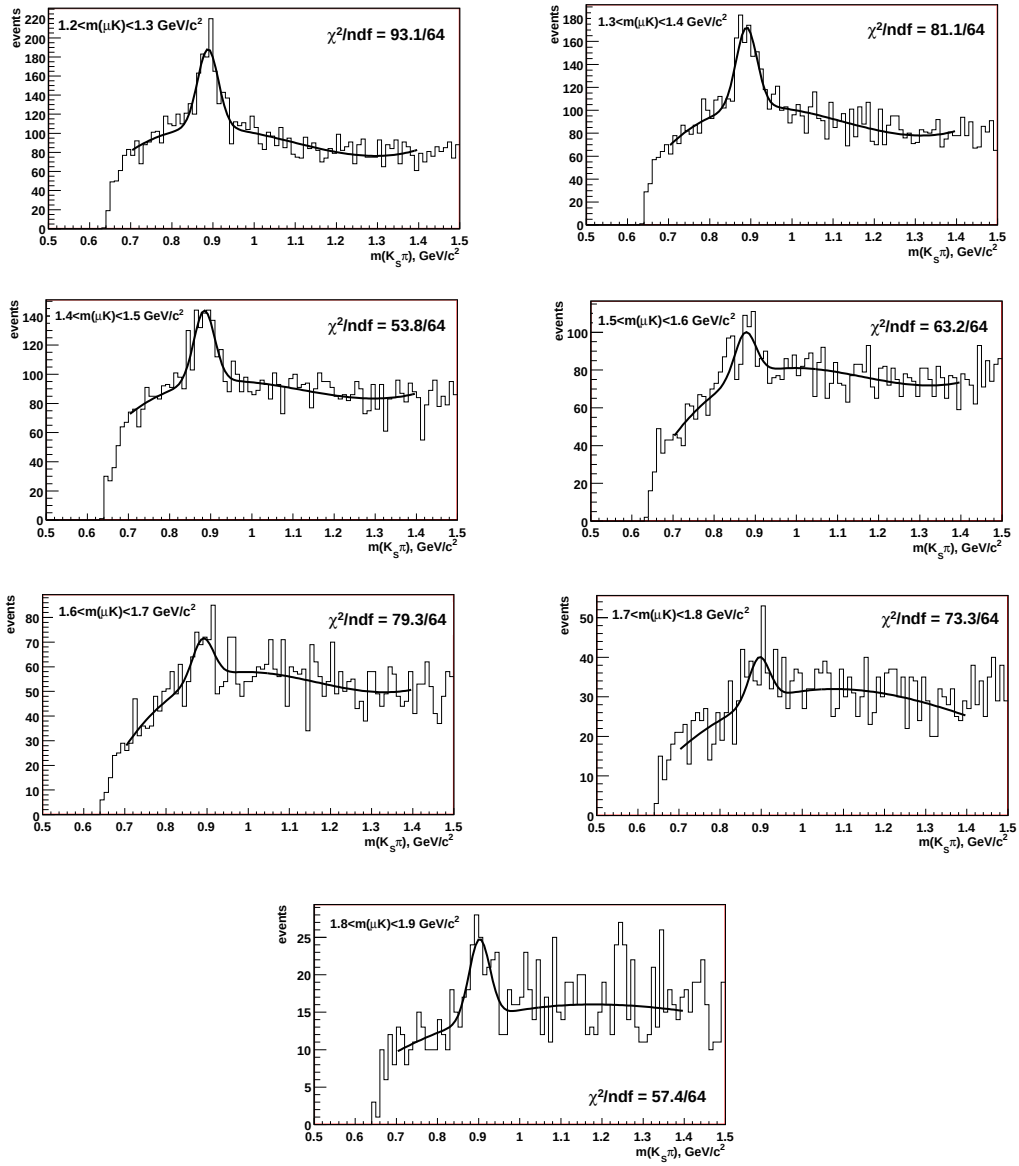

Figure 3.14: The distribution of the invariant mass of the $K_S\pi$ system in the signal regions of seven $m(\mu K)$ bins shown in Fig. 3.10. The fit function is explained in the text.

of D^* events, we reconstruct a K^{*-} decay in the channel $K^{*-} \to K^0\pi^-$, $K^0 \to K_S \to \pi^+\pi^-$ (and the charge conjugate). From the remaining tracks in the event, we select two forming a secondary vertex. We assign the masses of pions to the tracks, and require the invariant mass $m(\pi\pi)$ in the window around the K_S mass, $0.460 < m(\pi\pi) < 0.525$ GeV/c^2 (see Fig. 3.12). The K_S candidate is constructed from the two pions. Its trajectory is assumed to pass through the K_S decay vertex, and to be directed along the reconstructed momentum of the two-pion system.

The kaon candidate in the $\mu K\pi$ system is assigned a pion mass, and the invariant mass of the $K_S\pi$ system, $m(K_S\pi)$, is calculated. The $K^* \to K_S\pi$ signal in the signal band of the whole $m(\mu K)$ range, $1.2 < m(\mu K) < 1.9$ GeV/c^2, is shown in Fig. 3.13. The same $K^* \to K_S\pi$ signal, split into seven $m(\mu K)$ bins of Fig. 3.10, is shown in Fig. 3.14.

To extract the $K^* \to K_S\pi$ signal, we fit the $m(K_S\pi)$ distributions in Fig. 3.14 using a single Gaussian for the peak, and a third order polynomial for the background. From the fit in the whole $m(\mu K)$ range (see Fig. 3.13), we determine the width of the K^* peak: $\sigma = 24.7 \pm 2.2$ MeV. We fix the width of the K^* peak to its central value, 24.7 MeV, during the fit in seven $m(\mu K)$ bins. The seven peaks in Fig. 3.14 contain a total of 1639 $K^* \to K_S\pi$ events. So, the measured fraction of the decay $D^0 \to \mu^+K^{*-}\nu_\mu$ with $K^{*-} \to K^0\pi^-$, $K^0 \to K_S \to \pi^+\pi^-$ (and the charge conjugate) in our signal is around 0.16%. We have to convert this number into the actual fraction of the $D^0 \to \mu^+K^{*-}(K^0\pi^-)\nu_\mu$ decay. We take into account that the fractions of K_S and K_L state in K^0 are 0.5 each, and from [13] we learn that $\mathrm{Br}(K_S \to \pi\pi) = 0.69$. Also, the reconstruction efficiency of the $K_S \to \pi\pi$ decay at DØ is conservatively estimated at the level of 30% [95]. Finally, we estimate the fraction of the $D^0 \to \mu^+K^{*-}(K^0\pi^-)\nu_\mu$ decay in the D^* sample to be 1.6%. We assign a conservative uncertainty of $\pm 1.6\%$ to this number.

The modes 2 and 5 containing intermediate states are assumed to be reconstructed with an efficiency 50%, to which we assign a conservative un-

certainty of $\pm 50\%$. This uncertainty is propagated into the systematic uncertainty of the measurement of the kaon asymmetry. Using Table 3.6, and taking into account the $1.6 \pm 1.6\%$ contribution from the decay $\mu^+ K^{*-}(K^0\pi^-)\nu$, we estimate the signal fraction to be $f_K = 0.90 \pm 0.04$, and the background fraction to be $f_\pi = 0.10 \pm 0.04$.

To estimate the pion reconstruction asymmetry A_π in (3.23), we proceed as follows. The interaction cross-sections of positive and negative pions with matter differ by $(1.3 \pm 0.3)\%$ in the range 1−2 GeV/c [96]. We estimate A_π assuming a pion crosses 5 cm of pure beryllium on its way through the tracking system (which is an overestimate, see the description of SMT in Section 2.2.1). From [96] we take $\sigma(\pi^\pm d) \approx 70$ mb. We vary this number by 1%, and from (3.13) obtain the upper limit on the pion reconstruction asymmetry $A_\pi \lesssim 0.0002$. Thus, we neglect the term $f_\pi A_\pi \lesssim 2 \times 10^{-5}$ in (3.23), and correct the measured kaon asymmetry for the sample composition as

$$A_K = \frac{A}{f_K}. \tag{3.24}$$

So, the corrected kaon asymmetry is $A_K = -0.0145 \pm 0.0012$(stat.). Varying the reconstruction efficiency of the modes 2 and 5 by -50%, we obtain a signal fraction $f_K^{-50\%} = 0.91$. The corresponding variation of the kaon asymmetry is $\Delta A_K^{-50\%} = -0.0002$. Varying the reconstruction efficiency of the modes 2 and 5 by $+50\%$, we obtain a signal fraction $f_K^{+50\%} = 0.89$. The corresponding variation of the kaon asymmetry is $\Delta A_K^{+50\%} = +0.0002$. Finally, we assign a symmetric systematic uncertainty of $\Delta A_K = \pm 0.0002$ from the sample composition.

3.3.6 Systematic uncertainties

All the contributions to the systematic uncertainty on the kaon asymmetry are summarized in Table 3.7. The systematic uncertainty from the choice of the sideband in Δm is determined by varying the sideband limits, and

Source	ΔA_K
Choice of the sideband in Δm	–
Background description	0.0008
Sample composition	0.0002
Total	0.0008

Table 3.7: The systematic uncertainties on A_K.

is found to be negligible. The systematic uncertainty from the background description is estimated by using different background selection, (3.20) instead of (3.21). The sideband subtraction according to (3.22) is repeated, and the detector model (3.9) is solved. The result is shown in Table 3.5. The corresponding variation of the kaon asymmetry is +0.0008. We assign a symmetric systematic uncertainty, ±0.0008, from this source. The systematic uncertainty caused by the uncertainty of the sample composition (see previous section) is found by varying the reconstruction efficiency of modes containing intermediate states by ±50%. We assign a symmetric systematic uncertainty ±0.0002 from this source.

The total systematic uncertainty is obtained by summing the above contributions in quadrature. Finally, the kaon asymmetry in the D^* sample is found to be $A_K = -0.0145 \pm 0.0012(\text{stat.}) \pm 0.0008(\text{syst.})$.

3.3.7 Kaon asymmetry in other event samples

The procedure developed in the previous section can be used to measure the kaon asymmetry A_K in any sample of events with a single kaon in the final state. For this we should:

1. Find as many observables as possible which the kaon asymmetry depends on;

2. Convolve the kaon asymmetry dependence measured in the D^* sample with the probability distribution functions (pdf) of these observables

in another sample. This takes into account potentially different distributions of the particular observable in the D^* sample and in the target sample.

We consider the potential dependencies of A_K on:

1. Kaon momentum p_K, since the inelastic cross-sections of K^+ and K^- have a complicated dependence on p_K, see [13];

2. Kaon direction in the detector, θ_K, due to the following. According to (3.13),

$$A_K = \frac{1}{2}\left[\exp\left(-\frac{l}{l_0^-}\right) - \exp\left(-\frac{l}{l_0^+}\right)\right]. \tag{3.25}$$

In order to be reconstructed, a kaon should traverse the whole SMT and at least two inner-most CFT layers (see Table 3.1). From Fig. 3.15, assuming the distribution of the material in the detector is homogenous,

$$l = \frac{R}{\sin\theta_K}, \tag{3.26}$$

where R is the total thickness of the material traversed by a particle emitted at $\theta = \frac{\pi}{2}$. R is of order of several cm, the typical nuclear interaction length is of order 100 cm, so $R \ll l_0^\pm$ holds, and (3.25) can be approximated to:

$$A_K \approx -\frac{1}{2}R\left(\frac{1}{l_0^-} - \frac{1}{l_0^+}\right)\frac{1}{\sin\theta_K} \propto -\frac{1}{\sin\theta_K}. \tag{3.27}$$

To obtain the dependence of the kaon asymmetry on the kaon momentum, $A_K(p_K)$, we repeat the procedure of Section 3.3.3 in eight p_K bins of approximately equal statistics. The corresponding values of kaon asymmetry, corrected for the sample composition, are shown in Table 3.8 and plotted in Fig. 3.17. We observe an overall decrease of the kaon asymmetry with

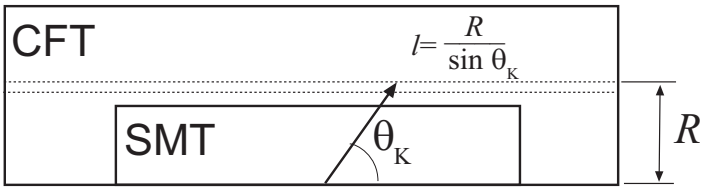

Figure 3.15: The θ dependence of the length of the kaon trajectory in the tracking volume.

	p_K bin, GeV/c	A_K
1	$(0.7, 1.7)$	-0.0275 ± 0.0037
2	$(1.7, 2.4)$	-0.0191 ± 0.0031
3	$(2.4, 3.2)$	-0.0160 ± 0.0029
4	$(3.2, 4.2)$	-0.0115 ± 0.0027
5	$(4.2, 5.5)$	-0.0129 ± 0.0026
6	$(5.5, 7.5)$	-0.0104 ± 0.0026
7	$(7.5, 11.5)$	-0.0078 ± 0.0026
8	> 11.5	-0.0091 ± 0.0027

Table 3.8: The kaon asymmetry, A_K, measured in eight bins of kaon momentum, p_K, of approximately equal statistics. Errors are statistical.

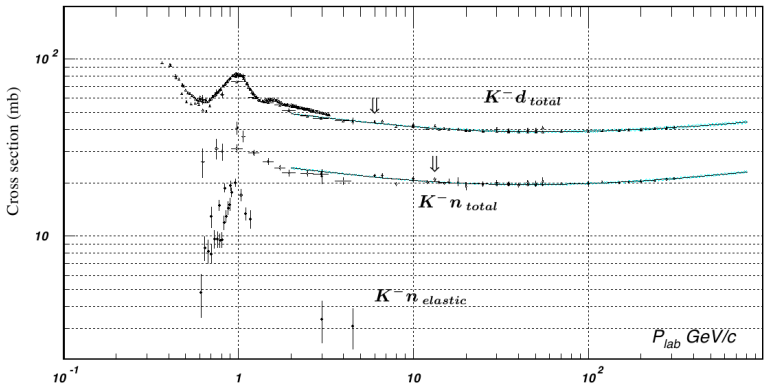

(a)

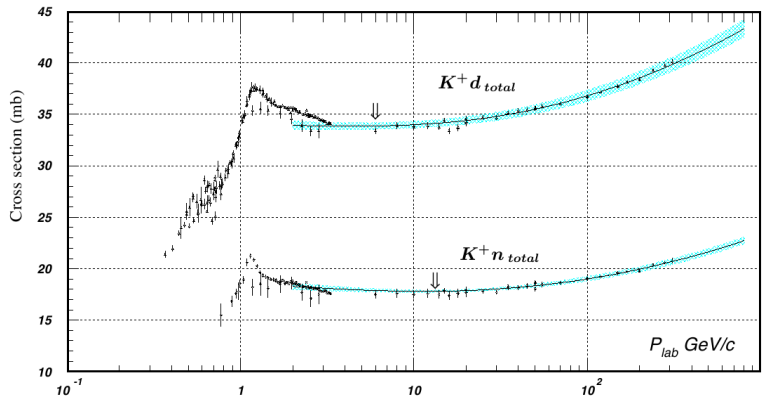

(b)

Figure 3.16: The cross-sections of inelastic interaction of a) negative and b) positive kaons with matter. Reproduced from PDG.

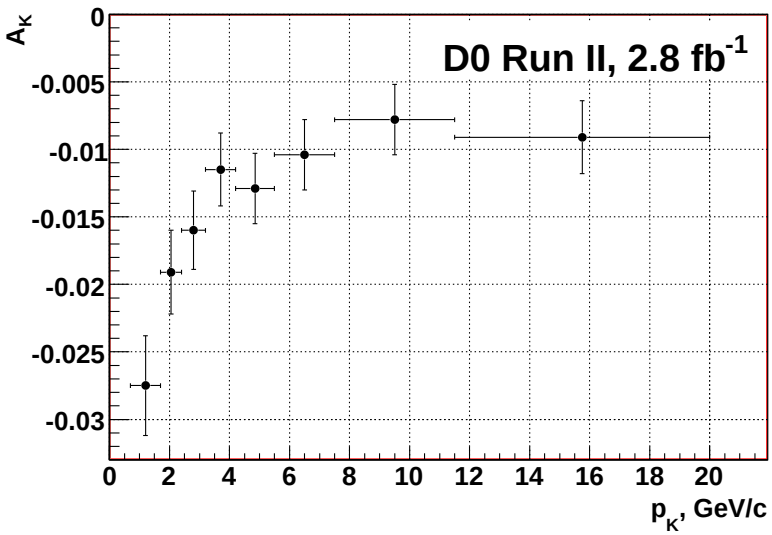

Figure 3.17: The dependence of the kaon asymmetry, A_K, on the kaon momentum, p_K, in eight bins of approximately equal statistics. Errors are statistical.

p_K, which corresponds to the decreased difference between the nuclear cross-sections $\sigma(K^-d)$ and $\sigma(K^+d)$ at $p_K \sim 10$ GeV/c (see Fig. 3.16 reproduced from PDG [13]).

The measured dependence of the kaon asymmetry on $1/\sin\theta_K$ is shown in Fig. 3.18. The value of $1/\sin\theta_K = 3.0$ corresponds to $\eta \approx 1.7$, close to the boundary of the CFT acceptance. The range $1.0 < 1/\sin\theta_K < 3.0$ contains 97% of the full event statistics. The expected dependence (3.27) is not observed, most probably due to the high inhomogeneity of the material distribution in SMT and CFT. Because it is impossible to conclude on the character of the dependence in Fig. 3.18, this is considered flat for the purposes of this analysis.

3.3.8 Results and Conclusions

Using the event sample of approximately 2.7M of decays $D^* \to D^0(\mu^+K^-\nu_\mu)\pi^+$ (and the charge conjugate) we perform the measurement of the kaon reconstruction asymmetry in DØ detector. We investigate the possible depen-

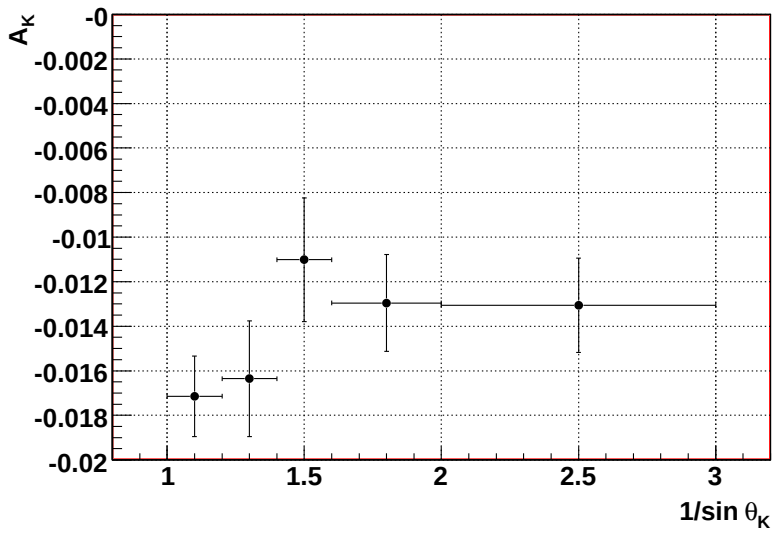

Figure 3.18: The dependence of the kaon asymmetry, A_K, on $1/\sin\theta_K$. Errors are statistical.

dences of the kaon reconstruction asymmetry on the absolute value of the kaon momentum and on the direction of the kaon in the detector. We observe a pronounced dependence on the kaon momentum (see Table 3.8 and Fig. 3.17). No significant dependence on the kaon direction is seen (see Fig. 3.18). The dependence shown in Fig. 3.17 can be used for precise measurements of the kaon reconstruction asymmetry in the samples with a single kaon in the final state, which then can be taken into account in CP violation measurements using (3.15).

3.4 Measurement of direct CP violation in $b \to sc\bar{c}$ and $b \to dc\bar{c}$ quark transitions using $B^+ \to J/\psi K^+$ and $B^+ \to J/\psi \pi^+$ decays

According to Section 1.4.1, direct CP violation asymmetry in $B^+ \to J/\psi K^+$ decay is defined as:

$$A^{dir}_{J/\psi K^+} = \frac{N(B^- \to J/\psi K^-) - N(B^+ \to J/\psi K^+)}{N(B^- \to J/\psi K^-) + N(B^+ \to J/\psi K^+)}. \tag{3.28}$$

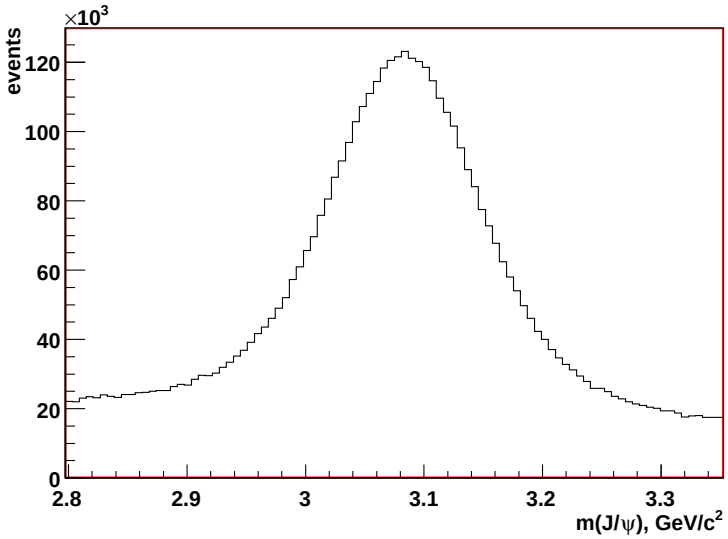

Figure 3.19: The invariant mass distribution of the two-muon system.

In the $B^+ \to J/\psi K^+$ decay, there is a single kaon in the final state, so the measured charge asymmetry between $B^- \to J/\psi K^-$ and $B^+ \to J/\psi K^+$, $A(J/\psi K)$ includes both $A^{dir}_{J/\psi K^+}$ and the kaon reconstruction asymmetry $A_K(J/\psi K)$. According to Section 3.3,

$$A^{dir}_{J/\psi K^+} = A(J/\psi K) - A_K(J/\psi K). \tag{3.29}$$

Direct CP asymmetry in $b \to dc\bar{c}$ manifests itself as (see Section 1.4.2):

$$A^{dir}_{J/\psi \pi^+} = \frac{N(B^- \to J/\psi \pi^-) - N(B^+ \to J/\psi \pi^+)}{N(B^- \to J/\psi \pi^-) + N(B^+ \to J/\psi \pi^+)}. \tag{3.30}$$

3.4.1 Event selection

The selection requirements are summarized in Table 3.9. The B^+ meson is reconstructed in the exclusive decay $B^+ \to J/\psi K^+$ with J/ψ decaying to $\mu^+\mu^-$. Each muon is required to leave signal in at least two layers of the muon system, $nseg > 1$ (see Section 2.3.3 for a detailed explanation of the $nseg$ variable), to have an associated track in the central tracking system with at least two measurements in the SMT, and a transverse momentum $p_T^\mu > 1.5$ GeV/c. At least one of the two muons is required to have matching

Quantity	Cut
Muons:	
$nseg(\mu_1)$ and $nseg(\mu_2)$	> 1
$nseg(\mu_1)$ or $nseg(\mu_2)$	> 2
Transverse momentum	> 1.5 GeV/c
#hits in SMT	> 1
J/ψ candidate mass	$2.80 < m(J/\psi) < 3.35$ GeV/c^2
Hadronic track:	
Transverse momentum	> 0.5 GeV/c
Total momentum	> 0.7 GeV/c
#hits in SMT	> 2
3-track system:	
Vertex fit χ^2	< 16 for 3 d.o.f.
The transverse projection of B^+ decay length divided by its error	$L_{xy}(B^+)/\sigma[L_{xy}(B^+)] > 3$
Combined significance of the B^+ with respect to the primary vertex	< 40

Table 3.9: Summary of the event selection cuts for the $B^+ \to J/\psi(\mu\mu)K^+$ decay.

track segments both inside and outside the toroidal magnet, $nseg > 2$. The two muons have to form a common vertex and to have an invariant mass between 2.80 and 3.35 GeV/c^2, to form a J/ψ candidate (see Fig. 3.19). An additional charged hadronic track with $p_T > 0.5$ GeV/c, with total momentum p >0.7 GeV/c and with at least two measurements in the SMT, is selected. This particle is assigned the mass of a kaon and is required to have a common vertex with the two muons, with $\chi^2 < 16$ for 3 degrees of freedom. The primary vertex of the $p\bar{p}$ interaction is determined for each event using the method described in Section 2.3.2. The transverse projection of the B^+ decay length calculated from the primary vertex is required to exceed 3 standard deviations.

From each set of three particles fulfilling these requirements, a B^+ candidate is constructed. The J/ψ mass constraint is applied to improve the precision of the measured muon momenta. The trajectory of the B^+ is assumed to pass through the reconstructed vertex and to be directed along its momentum. The reconstructed track of the B^+ is used to determine the axial, ϵ^d, and stereo, ϵ^z, projections of the impact parameter with respect to the primary vertex, together with the corresponding errors, $\sigma(\epsilon^d)$ and $\sigma(\epsilon^z)$. Since the B^+ track should originate from the primary vertex, the combined significance of the B^+ with respect to the primary vertex,

$$S_B = \left(\frac{\epsilon_B^d}{\sigma(\epsilon_B^d)}\right)^2 + \left(\frac{\epsilon_B^z}{\sigma(\epsilon_B^z)}\right)^2, \tag{3.31}$$

is required to be less then 40. The distribution of the invariant mass of the $J/\psi K$ system after the described selection is shown in Fig. 3.20.

The obtained event samples were used to construct the final selection of $B^+ \to J/\psi K^+$ using the likelihood ratio method described below. It is assumed that a set of discriminating variables can be constructed for a given event. It is also assumed that the probability density functions $f^s(x_i)$ for the signal and $f^b(x_i)$ for the background can be built for each variable x_i.

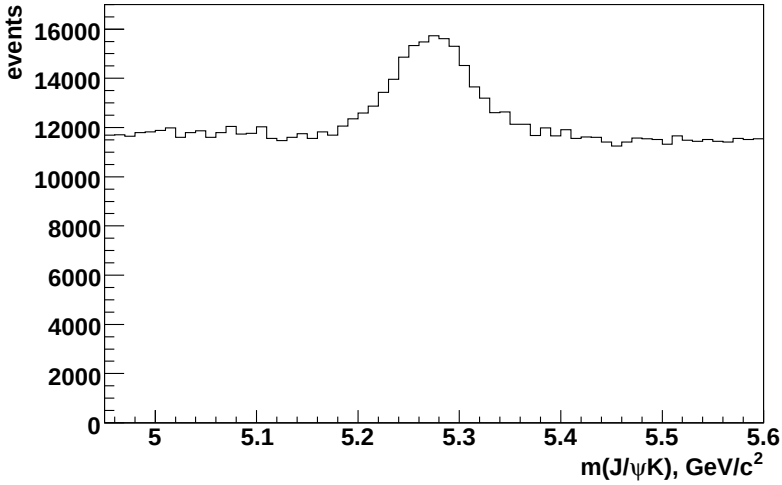

Figure 3.20: Distribution of the invariant mass of the $m(J/\psi K)$ system after applying the cuts of Table 3.9.

The combined tagging variable y is defined as

$$y = \prod_{i=1}^{n} y_i; \qquad y_i = \frac{f^b(x_i)}{f^s(x_i)}. \tag{3.32}$$

A given variable x_i can be undefined for some events. In this case the corresponding variable y_i is set to 1. The selection of the signal is obtained by applying the cut $y < y_{max}$.

The following discriminating variables are used:

- Minimal transverse momentum of the two muons, $p_T^{\mu,min}$;
- Transverse momentum of the kaon, p_T^K;
- Isolation of the $J/\psi K$ system, computed as

  $$\text{Isolation} = \frac{p^{tot}(J/\psi K)}{p^{tot}(J/\psi K) + \sum p_i^{tot}},$$

  where the sum is taken over all charged particles in the cone $\sqrt{(\Delta\phi)^2 + (\Delta\eta)^2} < 0.5$, and $\Delta\phi$ and $\Delta\eta$ are the pseudorapidity and the azimuthal angles with respect to the $J/\psi K$ direction. The momenta of final state particles (the two muons and the kaon) are not included in the sum;

- The transverse projection of B^+ decay length divided by its error, $L_{xy}/\sigma(L_{xy})$;
- The χ^2 of the B^+ decay vertex, defined in Section 2.3.2;
- Combined significance of the B^+ with respect to the primary vertex defined in (3.31);
- Combined significance of the kaon with respect to the primary vertex defined similarly to (3.31).

The probability density functions both for signal and background are obtained from the data (see Fig. 3.20). The signal band is defined as $5.19 < m(J/\psi K) < 5.34$ GeV/c^2, and the background band is defined as $4.98 < m(J/\psi K) < 5.13$ GeV/c^2 or $5.40 < m(J/\psi K) < 5.55$ GeV/c^2. The background probability density function for each variable is constructed using the sum of events in the two background bands. The signal probability density function is constructed by subtracting the background distribution multiplied by 0.5 from the distribution of events in the signal band. The obtained distributions for all variables are shown in Fig. 3.21-3.23. Fig. 3.24 shows the distribution of the combined tagging variable defined by the equation (3.32). $N(tot)$ is defined as the integral of the $m(J/\psi K)$ distribution over the signal band. $N(signal)$ is defined as the integral of the $m(J/\psi K)$ distribution over the signal band after the background subtraction. For the final selection of the $B^+ \to J/\psi K^+$ decays, the cut $\log_{10} y < -0.16$ is applied. With this cut the ratio $N(signal)/\sqrt{N(tot)}$ is very close to maximum, as seen from Fig. 3.25. The resulting distribution of the invariant mass of the $J/\psi K$ system is shown in Fig. 3.26.

3.4.2 Signal extraction

To extract the event yields of the $B^+ \to J/\psi K^+$ and $B^+ \to J/\psi \pi^+$ decays, we perform a multi-dimensional unbinned log-likelihood fit of the distribu-

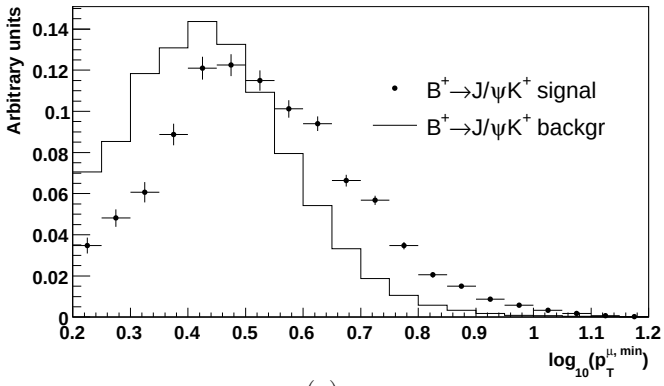

(a)

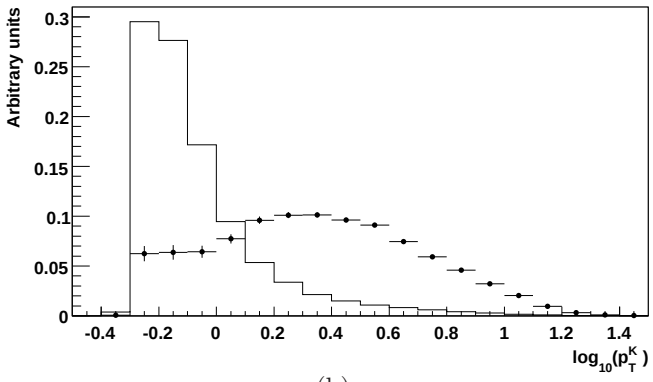

(b)

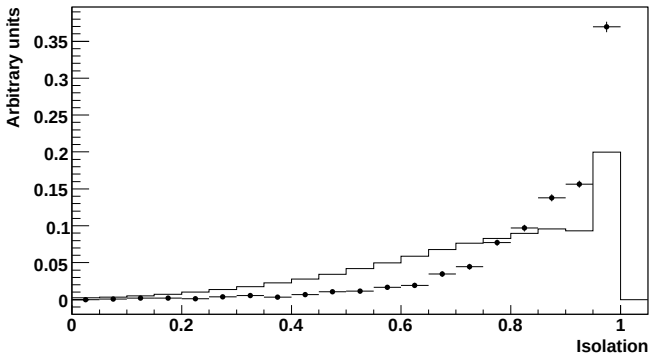

(c)

Figure 3.21: Normalized distributions of the discriminating variables: a) minimal transverse momentum of the two muons; b) kaon transverse momentum; c) isolation of the $J/\psi K$ system.

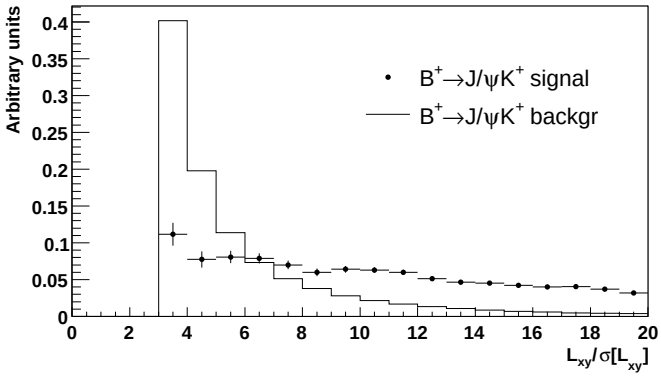

(a)

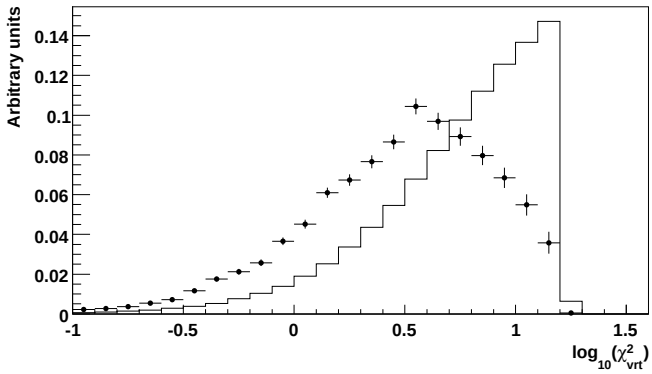

(b)

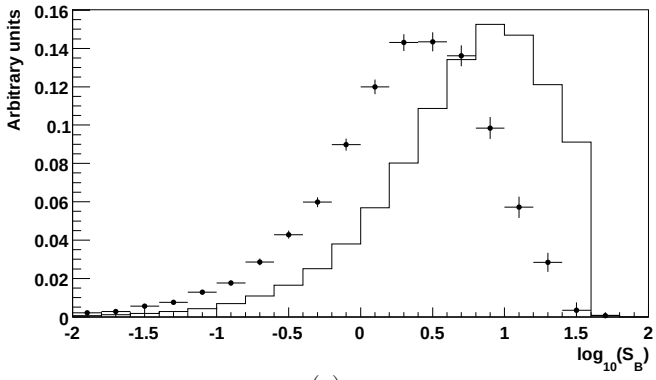

(c)

Figure 3.22: Normalized distributions of the discriminating variables: a) transverse projection of B^+ decay length divided by its error; b) χ^2 of the B^+ decay vertex; c) combined significance of B^+.

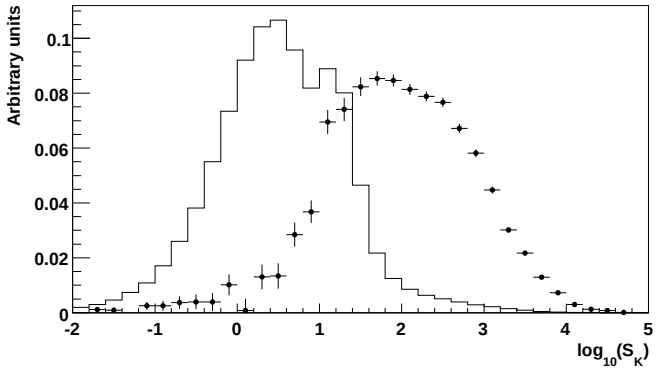

Figure 3.23: Normalized distributions of the discriminating variables: combined significance of kaon.

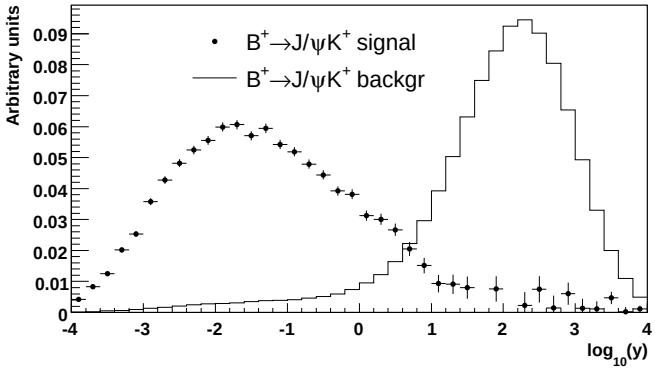

Figure 3.24: Distributions of $\log_{10}(y)$, where y is a combined tagging variable defined by (3.32).

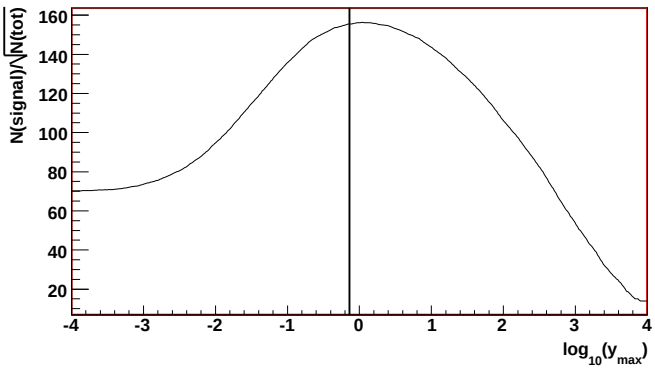

Figure 3.25: Significance of the signal computed as $N(signal)/\sqrt{N(tot)}$ as a function of the selection cut on $\log_{10}(y)$. The plot is obtained for a part of available event statistics. Vertical line shows the cut applied in this analysis.

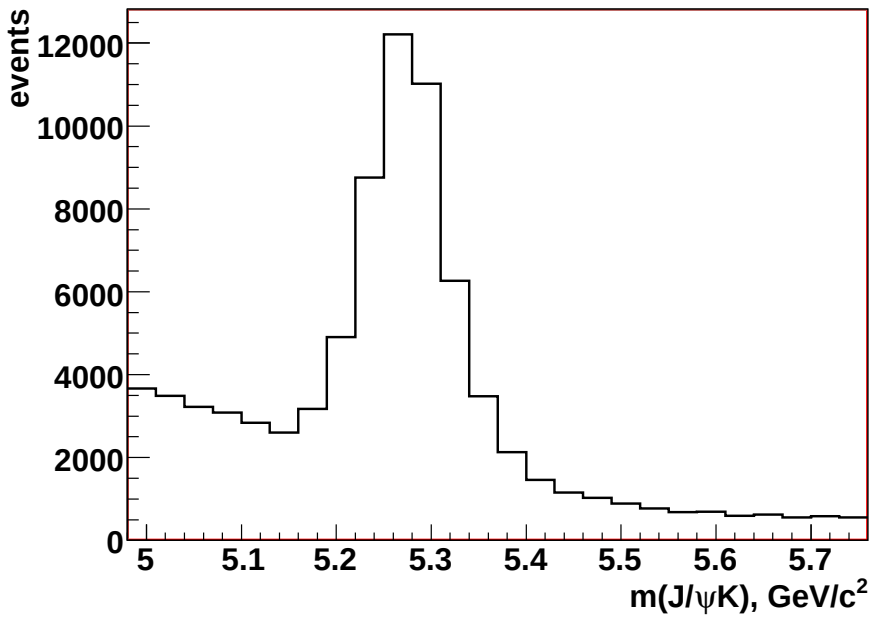

Figure 3.26: The distribution of the invariant mass of the $J/\psi K$ system after the final selection using the likelihood ratio method described in the text.

tion of $m(J/\psi K)$ to the sum of the following contributions:

- The $B^+ \to J/\psi K^+$ decay;
- The reflected mass peak from the $B^+ \to J/\psi \pi^+$ decay. This peak allows to measure direct CP asymmetry in $b \to dc\bar{c}$ using the $B^+ \to J/\psi \pi^+$ decay;
- The $B^+ \to J/\psi K^+ X$ decays, where $K^+ X$ stands for the decay products of e.g. K^* or $K_1(1270)$ of which only K^+ is reconstructed;
- Combinatorial background.

The fitting range is chosen to be $4.98 < m(J/\psi K) \equiv m < 5.76$ GeV/c^2 to ensure a stable description of the background under the peak. The corre-

sponding likelihood function is:

$$\mathscr{L} = \prod_{i=1}^{N} \alpha \left[\beta_1 \,\mathrm{Gauss}_{J/\psi K}(m_B, \sigma_B, m) + \beta_2 \,\mathrm{Gauss}_{J/\psi\pi}(m_{B,R}, \sigma_{B,R}, m)\right.$$
$$\left. + \beta_3 \,\mathrm{Threshold}_{J/\psi KX}(m)\right] + [1 - \alpha(\beta_1 + \beta_2 + \beta_3)] \,\mathrm{Exp}_{BKG}(m). \tag{3.33}$$

The index i runs from 1 to the number of B candidates N. The expected shape in m for the $J/\psi K^+$ contribution is a single Gaussian:

$$\mathrm{Gauss}_{J/\psi K}(m_B, \sigma_B, m) = \frac{1}{\sigma_B\sqrt{2\pi}} \exp\left(-\frac{1}{2}\left(\frac{m - m_B}{\sigma_B}\right)^2\right),$$

where m_B and σ_B are the position and the width of the $J/\psi K^+$ mass peak. The shape in m for the $J/\psi\pi^+$ contribution is also a single Gaussian:

$$\mathrm{Gauss}_{J/\psi\pi}(m_{BR}, \sigma_{BR}, m) = \frac{1}{\sigma_{BR}\sqrt{2\pi}} \exp\left(-\frac{1}{2}\left(\frac{m - m_{BR}}{\sigma_{BR}}\right)^2\right), \tag{3.34}$$

where the position of the reflected peak, m_{BR}, is defined assuming that the hadronic track is a kaon with momentum p and energy $E_K = \sqrt{p^2 + m_K^2}$:

$$m_{BR}^2 = (E_{J/\psi} + E_K)^2 - (p_{J/\psi} + p)^2. \tag{3.35}$$

m_{BR}^2 is shifted relatively to m_B^2 towards higher values due to the following. The $B^+ \to J/\psi\pi^+$ mass peak is centered at m_B:

$$m_B^2 = m_{J/\psi\pi}^2 = (E_{J/\psi} + E_\pi)^2 - (p_{J/\psi} + p)^2, \tag{3.36}$$

where $E_\pi = \sqrt{p^2 + m_\pi^2}$. However, if the pion is wrongly assigned a kaon mass, the invariant mass distribution becomes centered at

$$m_{BR}^2 = (E_{J/\psi} + E_K)^2 - (p_{J/\psi} + p)^2, \tag{3.37}$$

which is shifted relative to m_B^2 by

$$m_{BR}^2 - m_B^2 = 2\,E_{J/\psi}(E_K - E_\pi) + m_K^2 - m_\pi^2 > 0. \tag{3.38}$$

Note, that the position of the reflected peak depends on the kinematics of a particular event defined by the energy of the di-muon, $E_{J/\psi}$, and of the kaon candidate, E_K.

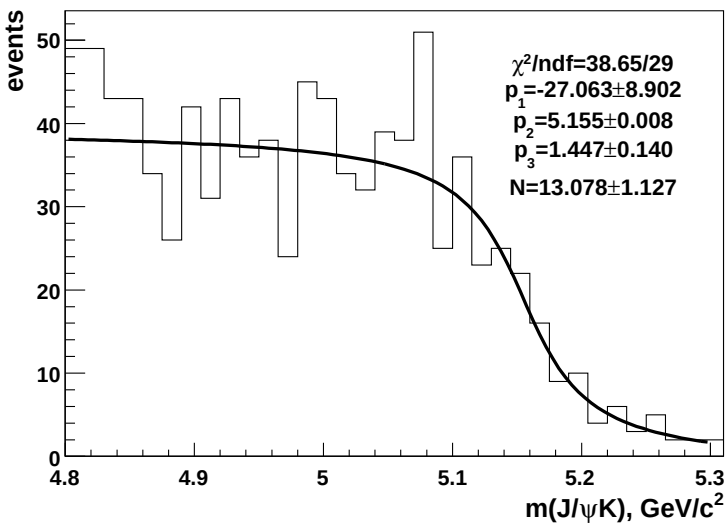

Figure 3.27: The $m(J/\psi K)$ distribution obtained using Monte Carlo simulation of $B^+ \to J/\psi K^*(K^+X)$ and $B^+ \to J/\psi K_1(1270)(K^+X)$ events. The fit is a threshold function described in the text.

The shape in m for the $B^+ \to J/\psi K^+X$ decays is determined using Monte Carlo simulation, which includes dominant modes $B^+ \to J/\psi K^*(K^+X)$ and $B^+ \to J/\psi K_1(1270)(K^+X)$ [13]. The $p\overline{p}$ collisions were generated in Pythia and passed to EvtGen for decay. The listing of the EvtGen decay file can be found in Appendix 3.4.7. The $m(J/\psi K)$ distribution in the $B^+ \to J/\psi K^+X$ decays is shifted relative to the B mass peak to the lower masses due to the unreconstructed system X (see Fig. 3.27). The part of the $J/\psi K$ peak in the range $4.80 < m < 5.30$ GeV/c^2 is parameterized as a threshold function of an arbitrary normalization N:

$$\text{Threshold}_{J/\psi KX}(m) = N\left(\arctan(p_1\,(m - p_2)) + p_3\right). \tag{3.39}$$

We assume the peak to vanish at $m = 5.30$ GeV/c^2. The parameters of the threshold function are determined from the fit in Fig. 3.27, and are fixed to their central values during the unbinned fit of the $m(J/\psi K)$.

The shape for the combinatorial background is an exponential with a slope S_{BKG}:

$$\text{Exp}_{BKG}(m) = C_{BKG} \exp\left(-\frac{m}{S_{BKG}}\right), \tag{3.40}$$

where C_{BKG} is a constant normalizing Exp_{BKG} to 1.

The fractions of different processes depend on the kinematic properties of the event defined by the energy of the di-muon system, $E_{J/\psi}$, and of the kaon candidate, E_K. The kinematic difference between $B^+ \to J/\psi K^+$ and $B^+ \to J/\psi \pi^+$ decay is small, so both fractions are assumed to have the same dependence on E_K. From Monte Carlo study we also find that the distributions of the kaon momentum, p_K, and correspondingly kaon energy, $E_K = \sqrt{m_K^2 + p_K^2}$, in the $B^+ \to J/\psi K^+ X$ and $B^+ \to J/\psi K^+$ decays are well within statistical errors (see Fig. 3.28). So, the fractions of the $J/\psi K$, $J/\psi \pi$, and $J/\psi K X$ signals are assumed to have the same dependence on E_K, which is parameterized by:

$$\alpha = \begin{cases} 1 + a_1 \frac{E_K - 3}{3} + a_2 \left(\frac{E_K - 3}{3}\right)^2 & \text{if } E_K < 3 \text{ GeV}, \\ 1 + a_3 \frac{E_K - 3}{7} & \text{if } 3 < E_K < 10 \text{ GeV}, \\ 1 + a_3 & \text{if } E_K > 10 \text{ GeV}, \end{cases} \tag{3.41}$$

with parameters a_i to be determined from the fit. The parameterization (3.41) is chosen "by eye", observing how the $m(J/\psi K)$ spectrum looks at different E_K. E_K is measured in GeV, and parameters a_i are considered dimensionless. The parameterization (3.41) is scaled by different factors β_1, β_2, and β_3 for the $J/\psi K$, $J/\psi \pi$, and $J/\psi K X$ contributions respectively, see (3.33). The factors are to be determined from the fit.

At high energies both the mass peak resolution and the fraction of the combinatorial background increase. The change in the resolution of the B mass peak at high E_K is parameterized by:

$$\sigma_B = \begin{cases} \left|\sigma_{B\,0} \left(1 + b_1 \frac{E_K}{10} + b_2 \left(\frac{E_K}{10}\right)^2\right)\right| & \text{if } E_K < 10 \text{ GeV}, \\ \left|\sigma_{B\,0} \left(1 + b_1 + b_2\right)\right| & \text{if } E_K > 10 \text{ GeV}, \end{cases} \tag{3.42}$$

with parameters $\sigma_{B\,0}$ and b_i to be determined from the fit. The parameterization (3.42) is chosen "by eye", E_K is measured in GeV, and parameters b_i are considered dimensionless. For small shifts of the reflected $J/\psi \pi$ peak from its nominal position, the resolution is assumed to scale linearly with

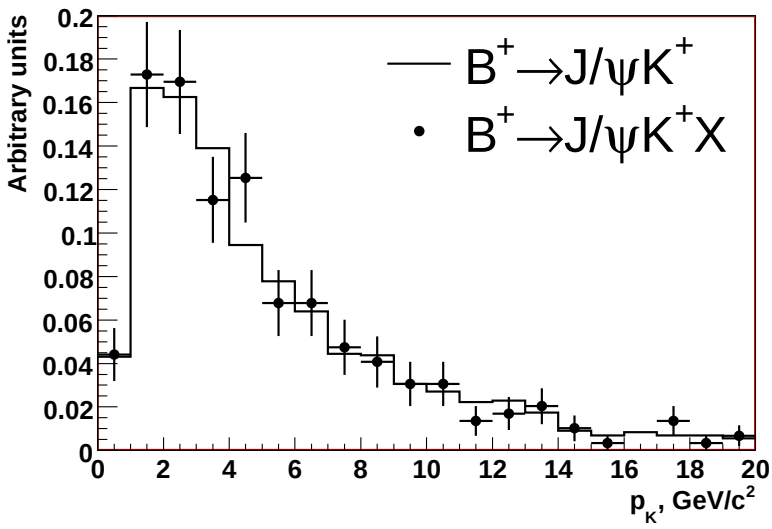

Figure 3.28: Distributions of $B^+ \to J/\psi K^+$ and $B^+ \to J/\psi K^+ X$ have similar dependence on p_K.

the mass of the reflection:

$$\sigma_{BR} = \sigma_B \frac{m_{BR}}{m_B}. \tag{3.43}$$

The change in the background slope at higher E_K is parameterized by:

$$S_{BKG} = \begin{cases} S_{BKG\,0}\left(1 + c_1 \frac{E_K}{10} + c_2 \left(\frac{E_K}{10}\right)^2\right) & \text{if } E_K < 10 \text{ GeV}, \\ S_{BKG\,0}\left(1 + c_1 + c_2\right) & \text{if } E_K > 10 \text{ GeV}, \end{cases} \tag{3.44}$$

with parameters $S_{BKG\,0}$ and c_i to be determined from the fit. The parameterization (3.44) is chosen "by eye", E_K is measured in GeV, and parameters c_i are considered dimensionless. As event count at high energies drops, in (3.41), (3.42), and (3.44) we parameterize α, σ_B, σ_{BR}, and S_{BKG} as constants for $E_K > 10$ GeV.

The result of the fit is shown in Fig. 3.29. The corresponding optimal values of the fit parameters, for energy of the kaon candidate measured in GeV, are listed in Table 3.10. The number of events in each channel is summarized in Table 3.11. Note, that as both $J/\psi K$ and $J/\psi \pi$ signals fall into the mass fit window, we should expect

$$\frac{N(B^+ \to J/\psi \pi^+)}{N(B^+ \to J/\psi K^+)} \approx \frac{\mathrm{Br}(B^+ \to J/\psi \pi^+)}{\mathrm{Br}(B^+ \to J/\psi K^+)}. \tag{3.45}$$

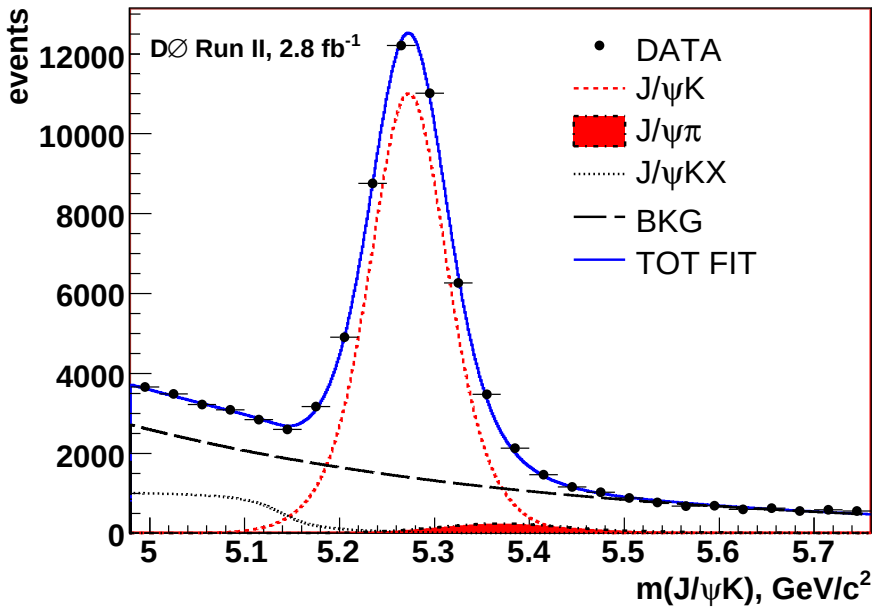

Figure 3.29: Result from the unbinned fit of invariant mass distribution of the $J/\psi K$ system.

where $\mathrm{Br}(B^+ \to J/\psi K^+)$ $[\mathrm{Br}(B^+ \to J/\psi \pi^+)]$ are the branching fractions of the corresponding decays as reported by PDG [13]. Indeed, from Table 3.11 we obtain $N(B^+ \to J/\psi\pi^+)/N(B^+ \to J/\psi K^+) = [3.92 \pm 0.30(\mathrm{stat})] \times 10^{-2}$, which is confirmed by PDG: $\mathrm{Br}(B^+ \to J/\psi\pi^+)/\mathrm{Br}(B^+ \to J/\psi K^+) = (4.86 \pm 0.62) \times 10^{-2}$. However, this is not the case with the $J/\psi KX$ decay, which falls only partially into the mass fit window. Besides, other $B \to J/\psi X$ decays which may contribute to the $J/\psi KX$ final state in the mass fit window create an uncertainty on the $J/\psi KX$ contribution. We account for the uncertainty of the $J/\psi KX$ contribution in the systematic uncertainty of the measurement.

3.4.3 Solving the detector model

To measure the asymmetries (1.71) and (1.81), the yields $N(B^\pm \to J/\psi K^\pm)$ and $N(B^\pm \to J/\psi\pi^\pm)$ are extracted from the normalization of the $B^\pm \to J/\psi K^\pm$ and reflected $B^\pm \to J/\psi\pi^\pm$ peaks of Fig. 3.29. To disentangle pos-

parameter		value
	$J/\psi K$ peak parameters:	
$m_{B\,0}$	GeV/c^2	5.2728 ± 0.0003
$\sigma_{B\,0}$	GeV/c^2	0.0245 ± 0.0005
b_1	–	2.0908 ± 0.1522
b_2	–	-0.3830 ± 0.1178
	signal fraction parameters:	
β_1	–	0.5136 ± 0.0025
β_2	–	0.0205 ± 0.0016
β_3	–	0.0693 ± 0.0027
a_1	–	-0.3799 ± 0.0898
a_2	–	-1.0975 ± 0.1436
a_3	–	-0.0142 ± 0.0187
	background parameters:	
$S_{BKG\,0}$	GeV/c^2	0.5223 ± 0.0266
c_1	–	-0.9571 ± 0.0921
c_2	–	0.9600 ± 0.0902

Table 3.10: Parameters of the unbinned fit shown in Fig. 3.29.

Channel	#events
$J/\psi K$	$40,222 \pm 242$
$J/\psi \pi$	$1,578 \pm 119$
$J/\psi KX$	$5,429 \pm 217$
Combinatorial Bkg	$33,192 \pm 425$
Total	80,422

Table 3.11: Result from the unbinned fit shown in Fig. 3.29: number of events in each channel.

sible detector effects, the procedure described in Section 3.2 is used. As the whole tracking is performed inside the solenoid, the initial sample is divided into eight subsamples corresponding to eight combinations of the solenoid polarity, kaon pseudorapidity, and kaon charge. The invariant mass distribution of the $J/\psi K$ system in every subsample is fitted using (3.33). The number of events in the $J/\psi K$, $J/\psi\pi$, and $J/\psi KX$ channels, and in the combinatorial background, extracted from the fits in eight $\beta\gamma q$ subsamples, are shown in Table 3.12. During the fits in the subsamples, all the parameters of the mass model (3.33), apart from the fraction of the $J/\psi K$ decays, β_1, the $J/\psi\pi$ decays, β_2, and the $J/\psi KX$ decays, β_3, are fixed to the values determined from the fit in the whole sample (see Table 3.10).

To extract the asymmetries in the signal channels, $J/\psi K$ and $J/\psi\pi$, the master equation (3.9) is solved with common ϵ^+. The resulting asymmetries are shown in Table 3.13. The measured charge asymmetry in the $J/\psi K$ channel is $A(J/\psi K) = -0.0070 \pm 0.0060(\text{stat})$, and that in the $J/\psi\pi$ channel is $A(J/\psi\pi) = -0.0887 \pm 0.0807(\text{stat})$.

Note, that the number of $J/\psi\pi$ events fluctuates considerably among the $\beta\gamma q$ subsamples (see Table 3.12). Therefore, the asymmetry measured in this channel is subject to high systematic uncertainty due to fitting procedure. The number of $J/\psi KX$ events also undergoes fluctuations, although at a lower level. The statistical fluctuations between the $\beta\gamma q$ subsamples in any particular channel may influence the asymmetries determined in this and other channels. This effect is accounted for in the systematic uncertainty from the mass model parameterization.

3.4.4 Kaon asymmetry in the $J/\psi K$ sample

The kaon asymmetry in the $J/\psi K$ sample is found by convolving the momentum dependence of the kaon asymmetry measured in the D^* sample (see Table 3.8) with the probability distribution function of the kaon momentum

$\beta\gamma q$	$J/\psi K$	$J/\psi\pi$	$J/\psi KX$	Combinatorial Bkg
$+++$	$5,104 \pm 87$	337 ± 44	692 ± 77	$4,079 \pm 151$
$+-+$	$5,131 \pm 87$	222 ± 42	689 ± 78	$4,170 \pm 151$
$++-$	$4,999 \pm 85$	212 ± 40	767 ± 76	$3,978 \pm 149$
$+--$	$5,098 \pm 86$	144 ± 38	523 ± 77	$4,395 \pm 150$
$-++$	$4,973 \pm 86$	158 ± 41	578 ± 78	$4,397 \pm 151$
$--+$	$5,039 \pm 86$	127 ± 39	663 ± 78	$4,281 \pm 150$
$-+-$	$4,965 \pm 85$	242 ± 41	794 ± 76	$3,880 \pm 148$
$---$	$4,906 \pm 84$	138 ± 39	724 ± 75	$4,006 \pm 147$
Total	$40,222 \pm 242$	$1,578 \pm 119$	$5,429 \pm 217$	$33,192 \pm 425$

Table 3.12: Number of events in the $J/\psi K$, $J/\psi\pi$, and $J/\psi KX$ channels, and in the combinatorial background, in different $\beta\gamma q$ subsamples.

	$J/\psi K$	$J/\psi\pi$	$J/\psi KX$	Combinatorial Bkg
N	$40,217 \pm 243$	$1,577 \pm 118$	$5,433 \pm 217$	$33,189 \pm 424$
ϵ^+	0.5060 ± 0.0030		0.4912 ± 0.0206	0.5010 ± 0.0064
A	-0.0070 ± 0.0060	-0.0887 ± 0.0807	0.0294 ± 0.0411	-0.0205 ± 0.0128
A_{fb}	0.0013 ± 0.0060	0.0453 ± 0.0890	0.0756 ± 0.0409	-0.0170 ± 0.0128
A_{det}	-0.0033 ± 0.0060	0.2061 ± 0.0826	0.0425 ± 0.0411	-0.0158 ± 0.0128
$A_{q\beta\gamma}{}^*$	-0.0050 ± 0.0060	-0.0207 ± 0.0873	0.0186 ± 0.0412	-0.0024 ± 0.0128
$A_{q\beta}$	0.0001 ± 0.0060	-0.1896 ± 0.0823	-0.0719 ± 0.0410	0.0274 ± 0.0128
$A_{\beta\gamma}$	-0.0030 ± 0.0060	0.0499 ± 0.0801	0.0540 ± 0.0411	-0.0145 ± 0.0128

Table 3.13: Physics asymmetry A and detector asymmetries for different channels after solving the system (3.9). The number of events in the $J/\psi K$ and $J/\psi\pi$ channels are fitted to (3.9) simultaneously with common ϵ^+.
* corresponds to the range-out asymmetry, negligible in the solenoid.

in the $J/\psi K$ sample:

$$A_K(J/\psi K) = \sum_i A_{K,i} \frac{N_i(J/\psi K)}{N(J/\psi K)}. \tag{3.46}$$

Here the sum runs over p_K bins, $A_{K,i}$ is the kaon asymmetry measured in the D^* sample in the i-th p_K bin of the Table 3.8, $N_i(J/\psi K)$ is the number of $J/\psi K$ events in this bin, and $N(J/\psi K)$ is the total number of $J/\psi K$ events, reported in Table 3.11. The numbers of $J/\psi K$ events in p_K bins, $N_i(J/\psi K)$, are determined from the unbinned log-likelihood fit in each p_K bin using the likelihood function (3.33) (see Fig. 3.30). We measure:

$$A_K(J/\psi K) = -0.0147 \pm 0.0012(\text{stat}). \tag{3.47}$$

The statistical uncertainty on $A_K(J/\psi K)$ is calculated by propagating the statistical uncertainties on $A_{K,i}$ (see Table 3.8), $N(J/\psi K)$ (see Table 3.11), and $N_i(J/\psi K)$ (see Fig. 3.30) into the convolution. The systematic uncertainty on $A_K(J/\psi K)$ includes the systematic uncertainty of 0.0008, calculated in Section 3.3.6. Additionally, the choice of the kaon momentum bins introduces a systematic bias. The convolution is repeated with four bins of equal statistics instead of eight. The deviation from the nominal value, $\Delta A_K(J/\psi K) = +0.0014$, is assigned as a symmetric systematic uncertainty from the choice of binning. The total systematic uncertainty, 0.0016, is obtained by summing the above contributions in quadrature. Finally:

$$A_K(J/\psi K) = -0.0147 \pm 0.0012(\text{stat.}) \pm 0.0016(\text{syst.}). \tag{3.48}$$

3.4.5 Systematic uncertainties

The systematic uncertainties on $A^{dir}_{J/\psi K^+}$ and $A^{dir}_{J/\psi \pi^+}$ originate from the systematic uncertainties on the measured charge asymmetries, $A(J/\psi K)$ $[A(J/\psi \pi)]$. In addition, the systematic uncertainty on $A^{dir}_{J/\psi K^+}$ has a contribution from the systematic uncertainty on the kaon charge asymmetry, $A_K(J/\psi K)$ (see previous section). All contributions are summarized in Table 3.14.

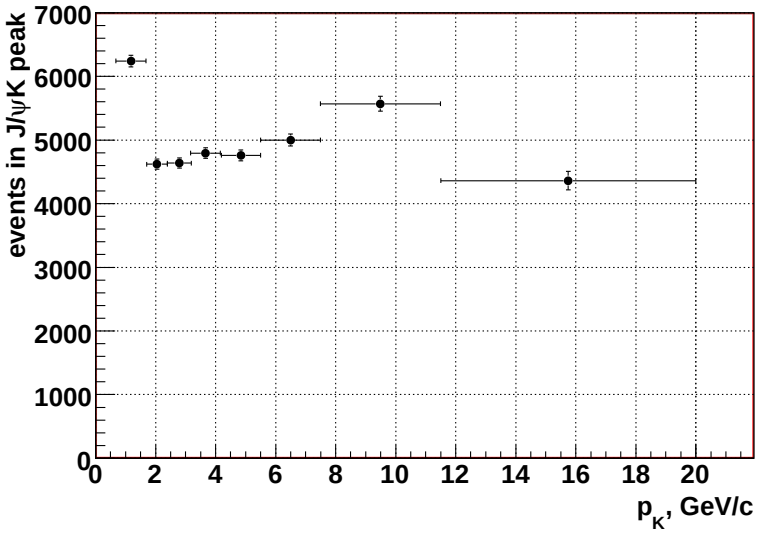

Figure 3.30: Momentum distribution in the $B \to J/\psi K$ sample, defined as the number of events in the $J/\psi K$ peak versus the kaon momentum bin, using the same bins in which the kaon asymmetry is measured (see Section 3.3).

Source	$\Delta A^{dir}_{J/\psi K^+}$	$\Delta A^{dir}_{J/\psi \pi^+}$
$\pm 1\sigma$ variation of the parameters		
fixed during the fit in $\beta\gamma q$ subsamples	0.0002	0.0004
Choice of the fitting range	0.0004	0.0129
Likelihood parameterization		
of the $J/\psi\pi$ and $J/\psi KX$ decays	0.0025	0.0252
Asymmetry of the kaon reconstruction	0.0016	–
Asymmetry of the pion reconstruction	–	0.0002
Total	0.0030	0.0283

Table 3.14: The systematic uncertainties on $A^{dir}_{J/\psi K^+}$ ($A^{dir}_{J/\psi \pi^+}$).

	Model variation	$A(J/\psi K)$	$A(J/\psi\pi)$	$A(J/\psi KX)$	$A(\text{Bkg})$
1	$J/\psi KX$ dropped	-0.0082	-0.1139	–	-0.0103
2	$A(J/\psi\pi) \to A(\text{Bkg})$	-0.0070	-0.0249	0.0421	-0.0240
3	$A(J/\psi KX) \to A(\text{Bkg})$	-0.0085	-0.1039	-0.0095	-0.0097
4	$A(J/\psi\pi), A(J/\psi KX)$ $\to A(\text{Bkg})$	-0.0095	-0.0123	-0.0121	-0.0121

Table 3.15: $A(J/\psi K)$: the systematic effect from the mass parameterization. The nominal value of $A(J/\psi K)$ is -0.0070. The maximal variation is -0.0025.

	Model variation	$A(J/\psi K)$	$A(J/\psi\pi)$	$A(J/\psi KX)$	$A(\text{Bkg})$
1	$J/\psi KX$ dropped	-0.0082	-0.1139	–	-0.0103
2	$A(J/\psi K) \to A(\text{Bkg})$	-0.0111	-0.0725	0.0081	-0.0109
3	$A(J/\psi KX) \to A(\text{Bkg})$	-0.0085	-0.1039	-0.0095	-0.0097
4	$A(J/\psi K), A(J/\psi KX)$ $\to A(\text{Bkg})$	-0.0094	-0.0807	-0.0090	-0.0093

Table 3.16: $A(J/\psi\pi)$: the systematic effect from the mass parameterization. The nominal value of $A(J/\psi\pi)$ is -0.0887. The maximal variation is -0.0252.

There are two sources of the systematic uncertainty on $A(J/\psi K)$ [$A(J/\psi\pi)$]: the one coming from the unbinned fit procedure, and the one from the parameterization of the invariant mass distributions of the $J/\psi\pi$ [$J/\psi K$] and $J/\psi KX$ decays. The uncertainty from the unbinned fit procedure is estimated as follows. Some parameters of the fits in $\beta\gamma q$ subsamples are fixed to the values determined from the fit in the whole sample, listed in Table 3.10. To determine corresponding systematic uncertainties on $A^{dir}_{J/\psi K^+}$ and $A^{dir}_{J/\psi\pi^+}$, we vary these parameters by $\pm 1\sigma$ in all possible combinations, repeat the fits in $\beta\gamma q$ subsamples using (3.33), and extract asymmetries using (3.9). We assign maximum variations of $A^{dir}_{J/\psi K^+}$ and $A^{dir}_{J/\psi\pi^+}$, 0.0002 and 0.0004, as respective uncertainties from the unbinned fit procedure. The fitting range is varied by ± 0.03 GeV/c^2 from both sides to determine the corresponding uncertainties: 0.0004 for $A^{dir}_{J/\psi K^+}$, and 0.0129 for $A^{dir}_{J/\psi\pi^+}$.

The charge asymmetries under study, $A(J/\psi K)$ and $A(J/\psi\pi)$, are systematically influenced by the mass parameterization of all decays taken into account in the fit. E.g., the invariant mass distribution of the $J/\psi KX$ decay is parameterized using Monte Carlo simulation, which possibly does not include all the processes contributing to the $J/\psi KX$ final state. To estimate a corresponding uncertainty, we drop the contribution of the $J/\psi KX$ signal and repeat the fit. The corresponding variation in the signal asymmetries, $A(J/\psi K)$ and $A(J/\psi\pi)$, can be read off from the first row in Tables 3.15 and 3.16. Also, the signal asymmetries, $A(J/\psi K)$ and $A(J/\psi\pi)$, can be systematically shifted by the fluctuations in eight $\beta\gamma q$ subsamples. To estimate this shift, we vary the mass model (3.33) as follows. From the fit in the whole sample, we determine the ratio of the fraction of $J/\psi\pi$ decays to the fraction of the combinatorial background. We repeat the fits in $\beta\gamma q$ subsamples keeping this ratio fixed to the value determined from the fit in the whole sample. This effectively includes the $J/\psi\pi$ signal in the background description. All the asymmetries are shown in Table 3.15, second row. Note that $A(J/\psi\pi) \approx A(\text{Bkg})$, as expected. The corresponding $A(J/\psi K)$ does

not change from its nominal value. Next, we fix the ratio of the fraction of $J/\psi KX$ decays to the fraction of combinatorial background. The resulting asymmetries are shown in Table 3.15, third row. Finally, we fix both the ratios of the $J/\psi\pi$ and $J/\psi KX$ fractions to the fraction of combinatorial background. The result can be seen in Table 3.15, fourth row. The maximal variation of $A(J/\psi K)$ from its nominal value, $\Delta A(J/\psi K) = -0.0025$, is assigned as a symmetric systematic uncertainty on $A(J/\psi K)$ from the mass model parameterization of the $J/\psi\pi$ and $J/\psi KX$ decays. A similar procedure is used to estimate the systematic shift of the $A(J/\psi\pi)$ due to the parameterization of the $J/\psi K$ and $J/\psi KX$ decays (see Table 3.16). The maximal variation of $A(J/\psi\pi)$ is found to be $\Delta A(J/\psi\pi) = -0.0252$, which is assigned as a symmetric systematic uncertainty from the mass model parameterization of the $J/\psi K$ and $J/\psi KX$ decays.

To review the estimation of the systematic uncertainty on the kaon asymmetry in the $J/\psi K$ sample, $A_K(J/\psi K)$, see Section 3.4.4. For $A(J/\psi\pi)$, we also take into account the charge asymmetry of the pion reconstruction, $A_\pi \sim 0.0002$, estimated in Section 3.3.5, which we assign as a systematic uncertainty from this effect.

The total systematic uncertainty for both $A(J/\psi K)$ and $A(J/\psi\pi)$ is obtained by summing the contributions in quadrature. This is largely dominated by the uncertainty from the mass parameterization.

3.4.6 Consistency check

We perform the following consistency check. We calculate $A^{dir}_{J/\psi K^+}$ separately in two subsamples of events with kaon momentum $p_K < 4.2$ GeV/c and $p_K > 4.2$ GeV/c, in which the kaon asymmetry is correspondingly high and low (see Fig. 3.17) and the statistics is approximately the same. The result is shown in Table 3.17. The difference between two asymmetries is $\Delta A^{dir}_{J/\psi K^+} = 0.0152 \pm 0.0130$, which is consistent with a statistical fluctuation.

	$A(J/\psi K)$	A_K	$A^{dir}_{J/\psi K^+}$
$p_K < 4.2$ GeV/c	-0.0044 ± 0.0079	-0.0187 ± 0.0016	0.0143 ± 0.0081
$p_K > 4.2$ GeV/c	-0.0112 ± 0.0101	-0.0103 ± 0.0014	-0.0009 ± 0.0102

Table 3.17: $A^{dir}_{J/\psi K^+}$ separately for $p_K < 4.2$ GeV/c and $p_K > 4.2$ GeV/c.

3.4.7 Results and Conclusions

To summarize, the charge asymmetry between $B^- \to J/\psi K^-$ and $B^+ \to J/\psi K^+$ is measured to be $A(J/\psi K) = -0.0070 \pm 0.0060$(stat.). The kaon asymmetry in the $J/\psi K$ sample is measured to be $A_K(J/\psi K) = -0.0147 \pm 0.0012$(stat.). Finally, direct CP asymmetry in the $b \to sc\bar{c}$ transition, as measured in the $B^+ \to J/\psi K^+$ decay, is:

$$\begin{aligned} A^{dir}_{J/\psi K^+} &= A(J/\psi K) - A_K(J/\psi K) \\ &= +0.0077 \pm 0.0061(\text{stat.}) \pm 0.0030(\text{syst.}), \end{aligned} \tag{3.49}$$

with the uncertainty approaching the level of the Standard Model prediction (+0.003). Our result is consistent with the PDG-2007 world average, $A_{CP}(B^+ \to J/\psi(1S)K^+) = +0.015 \pm 0.017$ [13], but has a better precision by a factor of two, thus providing the most stringent constraints for new models predicting large values of $A^{dir}_{J/\psi K^+}$. Our result disfavours large direct CP asymmetry in the $b \to sc\bar{c}$ transition possible from the flavor-changing neutral coupling $b \to sZ'$.

CP violating asymmetry in the $b \to dc\bar{c}$ transition, as measured in the $B^+ \to J/\psi\pi^+$ decay, is

$$A^{dir}_{J/\psi\pi^+} = -0.089 \pm 0.081(\text{stat.}) \pm 0.028(\text{syst.}). \tag{3.50}$$

The systematic uncertainty of both measurements is largely dominated by the uncertainty from the mass model parameterization.

Conclusions

Using the sample of the $B^+ \to J/\psi(1S)K^+$ decays, collected in RunIIa and RunIIb of Fermilab Tevatron collider, we measure direct CP violation asymmetry in the $b \to sc\bar{c}$ transition, using the decay $B^+ \to J/\psi K^+$:

$$\begin{aligned} A_{CP}(B^+ \to J/\psi(1S)K^+) &\equiv A^{dir}_{J/\psi K^+} \\ &= +0.0077 \pm 0.0061(\text{stat.}) \pm 0.0030(\text{syst.}), \end{aligned}$$

and in the $b \to dc\bar{c}$ transition, using the decay $B^+ \to J/\psi\pi^+$:

$$\begin{aligned} A_{CP}(B^+ \to J/\psi(1S)\pi^+) &\equiv A^{dir}_{J/\psi\pi^+} \\ &= -0.089 \pm 0.081(\text{stat.}) \pm 0.028(\text{syst.}). \end{aligned}$$

The measurement of $A^{dir}_{J/\psi K^+}$ potentially constraints the contribution from the New Physics processes which may surface in the tree or penguin diagrams, governing the $b \to sc\bar{c}$ transition. The results of the measurement reported in this dissertation were published in the Physical Review Letters [97], and reviewed in the context of New Physics searches in [98].

Despite having backgrounds much higher than those at B factories, the world-best statistical precision is achieved in the $B^+ \to J/\psi K^+$ channel due to the high yield of the signal events in the hadronic collisions. Also, the availability of the calibration channel for the precise measurement of the kaon reconstruction asymmetry removes a severe source of the systematic uncertainty suffered by the similar measurements at B factories.

For the purpose of the present analysis, a new method of measuring the charge asymmetries in the environment of the DØ detector is developed. The method strongly relies on the reversal of the polarities of the DØ magnets during the data taking to disentangle the detector-induced asymmetries. The method, however, does not need to be specific to DØ, and can be used in other detectors which exploit the similar polarity flip. The use of Monte Carlo simulation in the present analysis is quite reduced, which makes the corresponding systematic uncertainty largely insignificant.

Due to the constant efforts to decrease the systematic uncertainty, the precision of our measurement is statistically dominated. So, the simplest way of improving the measurement is by using a larger event sample. Currently, DØ has 4 fb^{-1} of data on tape, and another 4 fb^{-1} are expected by the end of Run II of Tevatron. Assuming that the number of events scales with integrated luminosity, with 8 fb^{-1} the statistical uncertainty on $A^{dir}_{J/\psi K^+}$ can be brought down to 0.003, which directly probes the level of the Standard Model penguin pollution, see (1.80). Besides, with larger event samples, the fluctuations among $\beta\gamma q$ subsamples reduce. This in turn tames the dominant systematic uncertainty of the measurement arising from the parameterization of the $J/\psi K$ mass peak.

Further reduction of statistical and systematic uncertainties of the measurement of the direct CP violation in the $B^+ \to J/\psi K^+$ and $B^+ \to J/\psi \pi^+$ decays has probably to wait until the LHC experiments, LHCb in particular, will reach their full physics capabilities. The era of the LHC will bring many additional possibilities and challenges for the studies of CP violation, so the coming years look very promising both from experimental and theoretical side of the subject.

Appendix

Decay file

Listing of the EvtGen file used to generate the $B^+ \to J/\psi K^+ X$ events:

```
#
# B+ -> J/Psi K*+ OR B+ -> J/Psi K+ OR B+ -> J/Psi K_1+
# J/Psi -> MuMu
# K*+ -> K pi or some K gamma
# K_1+ -> many channels
#
noMixing
Alias myJ/psi J/psi
Alias myK*+ K*+
Alias myK_1+ K_1+
Decay B+
1.410    myJ/psi           myK*+
         SVV_HELAMP PKHplus PKphHplus PKHzero
                    PKphHzero PKHminus PKphHminus;
1.800    myJ/psi myK_1+      PHSP;
Enddecay
Decay myK*+
0.6660      K0  pi+          VSS;
0.3330      K+  pi0          VSS;
0.0010      K+  gamma        VSP_PWAVE;
```

```
Enddecay
Decay myK_1+
0.2800   rho+  K0            VVS_PWAVE 1.0 0.0 0.0 0.0 0.0 0.0;
0.1400   rho0  K+            VVS_PWAVE 1.0 0.0 0.0 0.0 0.0 0.0;
0.1067   K*0   pi+           VVS_PWAVE 1.0 0.0 0.0 0.0 0.0 0.0;
0.0533   myK*+   pi0         VVS_PWAVE 1.0 0.0 0.0 0.0 0.0 0.0;
0.1100   omega  K+           VVS_PWAVE 1.0 0.0 0.0 0.0 0.0 0.0;
0.1444   K+    pi+ pi-       PHSP;
0.1244   K0    pi+ pi0       PHSP;
0.0412   K+    pi0 pi0       PHSP;
Enddecay
Decay myJ/psi
1.000000    mu+ mu-          PHOTOS  VLL;
Enddecay
End
```

Bibliography

[1] E. Wigner, Nobel Prize Lecture (1964), reprinted in [2].

[2] P. Wigner, Symmetries and Reflections. Scientific Essays, Indiana University Press, Bloomington and London (1967).

[3] an extensive lists of references can be found in [5] and [20].

[4] one of the original publications is N. Burgoyne, Nuovo Cim., **8**, 67 (1958).

[5] A. Pais, Inward Bound, Oxford University Press (1986), Chapter 21, section (b).

[6] D. Perkins, Introduction to High Energy Physics, Adisson-Wesley, 1987.

[7] C. Wu *et al.*, Phys. Rev. D **105**, 1423 (1957).

[8] L. Leipuner *et al.*, Phys. Rev. **132**, 2285 (1963).

[9] J. Cronin, Nishina Memorial Lecture (1997).

[10] J. Christensen *et al.*, Phys. Rev. Lett. **13**, 138 (1964).

[11] I. Bigi and A. Sanda, CP Violation, Cambridge University Press (2000).

[12] M. Kobayashi and T. Maskawa, Prog. Theor. Phys. **49**, 652 (1973).

[13] W.-M. Yao *et al.* [Particle Data Group], J. Phys. G **33**, 1 (2006) and 2007 partial update for edition 2008 (URL: `http://pdg.lbl.gov`).

[14] L. Wolfenstein, Phys. Rev. Lett. **51**, 1945 (1983).

[15] J. Charles *et al.* [CKMfitter Group], Eur. Phys. J. C **41**, 1-131 (2005) [hep-ph/0406184], results and plots as of summer 2008 available at: `http://ckmfitter.in2p3.fr/plots_Summer08/`.

[16] C. Jarlskog, Z. Phys. C **29**, 491 (1985).

[17] Y. Koide, Phys. Lett. B **607**, 123 (2005) [arXiv:hep-ph/0411280].

[18] K. Anikeev *et al.*, SLAC-REPRINT-2001-056, FERMILAB-PUB-01-197 (2001).

[19] D. Green, Lectures in Particle Physics, Vol. 55 of World Scientific Lecture Notes in Physics, World Scientific (1994).

[20] W. Gibson and B. Pollard, Symmetry principles in elementary particle physics, Cambridge University Press (1976).

[21] E. Barberio *et al.* [Heavy Flavor Averaging Group] [arXiv:0808.1297 [hep-ex]].

[22] I. Dunietz, R. Fleischer and U. Nierste, Phys. Rev. D **63**, 114015 (2001) [arXiv:hep-ph/0012219].

[23] see the review by S. Raby, [arXiv:hep-ph/0608183]; see also [25].

[24] see the review by T. P. Cheng and L. F. Li, COO-3066-143 (1980), published in Guangzhou Conf. 1980:1469; see also [25].

[25] S. P. Martin [arXiv:hep-ph/9709356] (1997).

[26] A. Sakharov, Zh. Eksp. Teor. Phys. Pis'ma Red. 5, 32 (1967).

[27] W. Bernreuther, CP Violation and Baryogenesis [hep-ph/0205279].

[28] S. Baek, P. Hamel, D. London, A. Datta and D. A. Suprun, Phys. Rev. D **71**, 057502 (2005) [arXiv:hep-ph/0412086].

[29] C. S. Kim, S. Oh and Y. W. Yoon, Phys. Lett. B **665**, 231 (2008) [arXiv:0707.2967 [hep-ph]].

[30] H. J. Lipkin, Phys. Lett. B **445**, 403 (1999) [arXiv:hep-ph/9810351].

[31] V. Barger, C. W. Chiang, P. Langacker and H. S. Lee, Phys. Lett. B **598**, 218 (2004) [arXiv:hep-ph/0406126].

[32] R. Fleischer, arXiv:hep-ph/0701217.

[33] S. Baek and D. London, Phys. Lett. B **653**, 249 (2007) [arXiv:hep-ph/0701181].

[34] W. S. Hou, M. Nagashima and A. Soddu, [arXiv:hep-ph/0605080].

[35] see e.g. M. Cvetic, P. Langacker and G. Shiu, Phys. Rev. D **66**, 066004 (2002) [arXiv:hep-ph/0205252], further references can be found in [31].

[36] B. Aubert *et al.* [BaBar Collaboration], Phys. Rev. Lett. **99**, 171803 (2007) [arXiv:hep-ex/0703021].

[37] K. F. Chen *et al.* [Belle Collaboration], Phys. Rev. Lett. **98**, 031802 (2007) [arXiv:hep-ex/0608039].

[38] H. Sahoo *et al.* [Belle Collaboration], Phys. Rev. D **77**, 091103 (2008) [arXiv:0708.2604 [hep-ex]].

[39] G. Bonvicini *et al.* [CLEO Collaboration], Phys. Rev. Lett. **84**, 5940 (2000) [arXiv:hep-ex/0003004].

[40] B. Aubert *et al.* [BaBar Collaboration], Phys. Rev. Lett. **94**, 141801 (2005) [arXiv:hep-ex/0412062].

[41] K. Abe *et al.* [BELLE Collaboration], Phys. Rev. D **67**, 032003 (2003) [arXiv:hep-ex/0211047].

[42] I. Dunietz, Phys. Lett. B **316**, 561 (1993).

[43] S. Fratina *et al.*, Phys. Rev. Lett. **98**, 221802 (2007) [arXiv:hep-ex/0702031].

[44] B. Aubert *et al.* [BaBar Collaboration], Phys. Rev. Lett. **99**, 071801 (2007) [arXiv:0705.1190 [hep-ex]].

[45] B. Aubert *et al.* [BaBar Collaboration], Phys. Rev. D **74** (2006) 011101 [arXiv:hep-ex/0603012].

[46] S. E. Lee *et al.* [Belle Collaboration], Phys. Rev. D **77** (2008) 071101 [arXiv:0708.0304[hep-ex]].

[47] B. Aubert *et al.* [BaBar Collaboration], Phys. Rev. D **76**, 111102 (2007) [arXiv:0708.1549[hep-ex]].

[48] H. Miyake *et al.* [Belle Collaboration], Phys. Lett. B **618**, 34 (2005) [arXiv:hep-ex/0501037].

[49] B. Aubert *et al.* [BaBar Collaboration], Phys. Rev. Lett. **92**, 241802 (2004) [arXiv:hep-ex/0401035].

[50] G. Blaylock, A. Seiden and Y. Nir, Phys. Lett. B **355**, 555 (1995) [arXiv:hep-ph/9504306].

[51] J. D. Cockcroft and E. T. S. Walton, Proc. R. Soc. London A137:229 (1932), available online at `http://journals.royalsociety.org/content/2m21113156463273/`.

[52] any textbook in accelerator physics, e.g. D. A. Edwards and M. J. Syphers, An Introduction to the Physics of High Energy Accelerators, John Wiley and Sons, Inc. (1993).

[53] The Run II Luminosity Upgrade at the Fermilab Tevatron Collider, Project Plan and Recource-Loaded Schedule, June 15 (2003), available online at `www-bd.fnal.gov/doereview03/docs/Overview7.1.pdf`.

[54] V. Lebedev, Run II Status and Goals: Can We Achieve 8 fb^{-1}, FNAL (2006), available online at

http://www-bdnew.fnal.gov/pbar/organizationalchart/lebedev/RunIIb/Presnt/RunIISep2006Presentation.doc.

[55] V. M. Abazov *et al.* [DØ Collaboration], Nucl. Instrum. Meth. A **565**, 463 (2006) [arXiv:physics/0507191].

[56] R. Yarema *et al.*, A Beginners Guide to the SVXII, FERMILAB-TM-1892 (1994).

[57] Degussa AG, Düsseldorf, Germany, http://www.rohacell.com.

[58] http://www-d0.fnal.gov/computing/algorithms/howto/howtoreco.html.

[59] T. Diel *et al.*, Tracking Algorithm Recommendation Commettee (TARC) Report II (2003), abailable online at http://d0server1.fnal.gov/www/Computing/Web/Meeting/Reviews/TARC/TARC2Recom.pdf.

[60] http://www-d0.fnal.gov/computing/algorithms/status/p14.html.

[61] G. Hesketh, Central Track Extrapolation Through the DØ Detector, DØ note 4079 (2003).

[62] G. Borissov, Ordereing a Chaos, or Technial Details of AA Tracking, talk given at All DØ Meeting, 28 February 2003.

[63] http://en.wikipedia.org/wiki/Kalman_filter

[64] http://www.cs.unc.edu/∼welch/media/pdf/maybeck_ch1.pdf

[65] http://en.wikipedia.org/wiki/Hough_transform.

[66] A. Khanov, HTF: histogramming method for finding tracks. The algorithm description, DØ note 3778 (2000).

[67] H. Greenlee, The DØ Interactinng Propagator, DØ note 4293 (2003).

[68] J. Abdallah *et al.* [DELPHI Collaboration], Eur. Phys. J. C **32**, 185 (2004) [arXiv:hep-ex/0311003].

[69] O. Peters, Muon Segment Reconstruction – Linked List Algorithm, DØ note 3901 (2001).

[70] F. Déliot, The Fit Algorithm in muo_trackreco (2000), available online at `http://www-d0.fnal.gov/~deliot/fitalg.ps`.

[71] P. Calfayan *et al.*, Muon Identification Certification for p17 data, DØ note 5157 (2007).

[72] J. Temple *et al.*, Upgrade of Level 1 Muon Trigger Logic for the v13 Trigger List, DØ note 4566 (2004).

[73] K. Hanagaki, DØ Layer 0 – innermost layer of Silicon Microstrip Tracker, FERMILAB-CONF-06-519-E (2006).

[74] M. Joghnson, Noise Performance of the DØ Layer 0 Silicon Detector, FERMILAB-CONF-06-401-E (2006).

[75] T. Sjöstrand *et al.*, Comp. Phys. Commun. **135**, 238 (2001); further documentation at `http://www.thep.lu.se/~torbjorn/Pythia.html`.

[76] D. J. Lange, Nucl. Instrum. Meth. **462**, 152 (2001); further documentation at `http://www.slac.stanford.edu/~lange/EvtGen`.

[77] `http://www-clued0.fnal.gov/d0_mess`.

[78] `http://www-d0.fbal.gov/computing/MonteCarlo/simulation/d0gstar.html`.

[79] GEANT Detector Description and Simulation Tool, CERN Program Library Long Writeup W5013 (1993); further documentation at `http://wwwasd.web.cern.ch/wwwasd/geant/`.

[80] `http://www-d0.fbal.gov/computing/MonteCarlo/simulation/d0sim.html`.

[81] `http://www-d0.fnal.gov/computing/algorithms/status/p1703.html`.

[82] `http://www-d0.fnal.gov/computing/algorithms/reco/prod_release/p2003/p2003d0reco.html`.

[83] http://www-d0.fnal.gov/Run2Physics/ckm/d0_private/btriggers/.

[84] http://www-d0.fnal.gov/Run2Physics/ckm/d0_private/btriggers/btrig_strategy.ps.

[85] http://www-d0.fnal.gov/Run2Physics/ckm/d0_private/btriggers/no_ip_bias/unbiased.html.

[86] http://www-d0.fnal.gov/Run2Physics/ckm/d0_private/bgv/aa/bana.htm.

[87] S. Catani *et al.*, Phys. Lett. B **269**, 432 (1991).

[88] http://wwwasd.web.cern.ch/wwwasd/paw/.

[89] http://root.cern.ch.

[90] G. Borissov, New Inclusive Muon Skim, talk given at DØ B physics group meeting, 21 April 2005.

[91] E. Halkiadakis, Asymmetries in $W^{\pm}$ and Z^0/γ^* Production at the Tevatron, talk given at ICHEP04 (2004).

[92] U. Nierste [arXiv:hep-ph/0406300].

[93] A. Lenz and U. Nierste, [arXiv:hep-ph/0612167].

[94] F. James, MINUIT − Function Minimization and Error Analysis, CERN Program Library Long Writeup D506 (1998).

[95] G. Borissov, personal communication.

[96] A. Carter *et al.*, Phys. Rev. **168**, 1457 (1968).

[97] V. M. Abazov *et al.* [DØ Collaboration], Phys. Rev. Lett. **100**, 211802 (2008) [arXiv:0802.3299 [hep-ex]].

[98] G. W. S. Hou, [arXiv:0808.1932 [hep-ex]].